DEVELOPMENT OF AN UNCREWED SEDIMENT SAMPLING SYSTEM

by

Jun Han Bae

A Dissertation

Submitted to the Faculty of Purdue University

In Partial Fulfillment of the Requirements for the degree of

Doctor of Philosophy

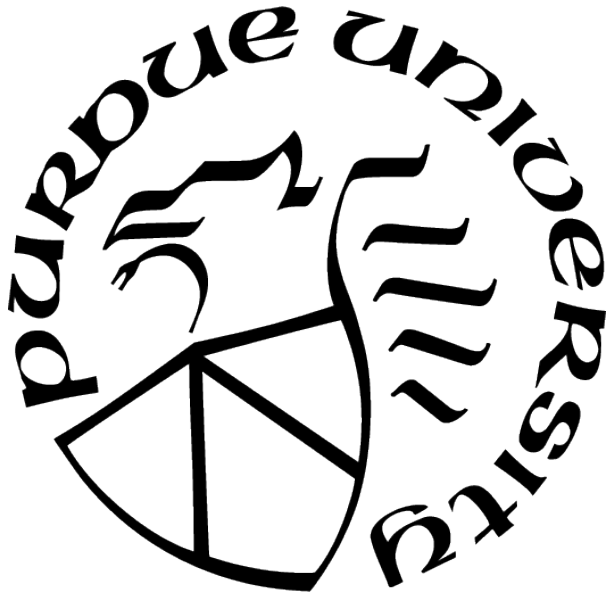

Department of Computer and Information Technology

West Lafayette, Indiana

December 2021

THE PURDUE UNIVERSITY GRADUATE SCHOOL
STATEMENT OF COMMITTEE APPROVAL

Dr. Byung-Cheol Min, Co-Chair

Department of Computer and Information Technology

Dr. Richard M. Voyles, Co-Chair

School of Engineering Technology

Dr. J. Eric Dietz

Department of Computer and Information Technology

Dr. Xiumin Diao

School of Engineering Technology

Dr. Sara K. McMillan

Department of Agricultural and Biological Engineering

Approved by:

Dr. Kathryne A. Newton

This dissertation is dedicated to my love-Hyelyn, my children (Eilyn-Soheon, Jayden-Byunghoon, and Adelyn-Nayeon), and my parents for their endless support and love.

ACKNOWLEDGMENTS

This journey started in 2012 fall. I still remember the day of arrival, August 8th, 2012. It was hot and humid summer. The Chicago O'Hare International airport was disappointing for me, compared to the Incheon International airport. My parents were already in Chicago on that day, so I met them at the airport. My mother was complaining about my duty-free cigarette cartons. Ten cigarette cartons were the most important thing when I started my journey in the USA as a graduate student. I joined the College of Technology (now Purdue Polytechnic) as a part of the fellowship program in Korea. I was in the STX Shipbuilding & Offshore company before taking a flight to the USA, and I was looking for new positions and planning to apply for the graduate schools in Korea. Luckily, I joined the fellowship program. That fellowship program was to send people already in the heavy industry to a high-ranked engineering university and make them upgraded professionals by earning a Master's degree. Twelve people were in the fellowship program, and my closest colleague was Jaeyoung Park. He helped me a lot during the stay, and we lived together almost every day until he left Purdue. By that time, I met Gilchan Park and Dr. Byung-Cheol Min. Gilchan was my roommate for a year and mental pillar until now. The first year, I only focused on playing sports, making friends, and traveling. The fellowship was only one year, and half of the fellowship members went back to Korea. I decided to stay longer to pursue my Master's degree. By that time, I was using the same lab space as Dr. Min. He influenced me a lot, and Dr. Min, Gilchan, and I had fun together. When Dr. Min graduated, I told him that 'I will be your graduate student when you become an assistant professor'. It was a half-joke at that time, but the word became true. Dr. Min came back to Purdue in 2015 as a faculty. I was a second-year Ph.D. student.

The Year 2014 was one of the craziest years of my life. The relationship between my wife and I was unsure around that time. I need to do something to make her as mine. I betted my life, and finally, I could marry my wife. I would still make the same decision when I can go back to that time, but it was a really tough day for me. Anyway, I brought my wife to Purdue in 2015, and Dr. Min also came back. Dr. Min and I started a SMART Lab and started my research. I did not do anything during 2014, so I consider 2015 is the first year of my Ph.D.

I constructed my research topic and worked hard to develop a robotic sediment sampling system. I made the first prototype of the underwater sediment sampler and published my first conference paper in 2016. Jee Hwan Park helped me a lot in developing the sampler and writing a paper. In 2016, my first daughter, Eilyn, was born. After she born, my life changed a lot. It was hard to believe that I had become a father and didn't know what to do. I was so happy to have my first child, but my research started the dark ages. I tried to develop the second version of the sampler, but it didn't go well. I decided to make a test-bed instead of the actual sampler to analyze the sediment and sediment sampling more. Wonse Jo and Jee Hwan helped me a lot to develop the test-bed and massive experiment. Luckily, we could complete the journal paper, but it took more than 2 years to publish it. We finally published it to the IEEE Journal of Oceanic Engineering in 2020. I really had a hard time between 2016 and 2020, but my son, Jayden, was born in 2018, and my second daughter, Adelyn, in 2020. They were the hope of my life.

In 2019, I met Dr. Bumjoo Lee, and he was a visiting scholar of the SMART Lab. He designed the first draft of the current underwater sediment sampler. He taught me how to design the mechatronics system and how to integrate sensors with hardware. Based on his dedication, we could accelerate the sampler development again. Pou Hei Chan (Gavin) joined our team, and he and I devoted ourselves to developing the sampler for almost a year. Gavin was a freshman at that time, but his skills and knowledge were not like a normal college freshman. Yongho Kim joined our team in 2020 fall to establish the software architecture of the unmanned sediment sampling system. Yongho has been my old friend since 2013, and he is the embedded system master. In March 2021, we finally started our field experiment. It was a really touch field experiment, but Gavin and Yongho dedicated themselves to evaluating the system. We even upgraded this system during field experiments. We collected many photos, videos, and meaningful data from fourteen field experiments. The final step is the demonstration of the unmanned sediment sampling system in Arequipa, Peru. The development of this system was part of the NEXUS project between Purdue University and UNSA (National University of Saint Augustine). We have already shipped the entire system to Peru and planning to visit Peru as a final step of the project.

This was a long, long journey. I spent all my 30's in West Lafayette, and the size of my family changed from 2 to 5. I cannot remember all names during this journey, but I really appreciate your support. First of all, great thanks to my advisor, Dr. Byung-Cheol Min and my co-chair, Dr. Richard Voyles. Special thanks to my committees - Dr. J. Eric Dietz, Dr. Sara McMillan, and Dr. Xiumin Diao; my special colleagues - Pou Hei Chan, Dr. Shaocheng Luo, Dr. Manoj Penmetcha, Dr. Sangjun Lee, Wonse Jo, and Jee Hwan Park. Thanks to former advisors of my Master's committee - Dr. Mark French, Dr. Eric Matson, and Professor Nancy Denton; Mentor from Korea - Dr. Bumjoo Lee. Special love to my precious friends, Dr. Gilchan Park, Dr. Yongho Kim, and his wife, Dr. Seongha Park. Lastly, endless love to my family, Hyelyn, Eilyn, Jayden, Adelyn, my mother, and my father. Also, to my grandmother and grandfather, who will see all of us in heaven.

TABLE OF CONTENTS

LIST OF TABLES

LIST OF FIGURES

LIST OF SYMBOLS

Chapter 3

M_1	Motor 1 of the sediment sampling platform
M_2	Motor 2 of the sediment sampling platform
v	Linear velocity of the sediment sampling platform
ω_r	Angular velocity of the sediment sampling platform
f_r	Direction changing frequency
F_p	Penetration force of the sediment sampling platform
C_1	Current of Motor 1
C_2	Current of Motor 2
C_{max}	Maximum current allowed
$f_1(\mathbb{X})$	Reciprocal function of the density of the sampled sediment
$f_2(\mathbb{X})$	Reciprocal function of the power of the sediment sampler
w_1, w_2	Finite weighting factors
m_s	Mass of sampled sediment
V_d	Desired volume of the core sampler
r	Radius of the core sampler
L_d	Desired depth
P_1	Sampling pattern 1 (Linear)
P_2	Sampling pattern 2 (Helix)
P_3	Sampling pattern 3 (Zig-zag)

Chapter 4

n_p	Port (left) side thruster velocity
n_s	Starboard (right) side thruster velocity
A_p	Port side anchor position
A_s	Starboard side anchor position
$L_{A,p}$	Port side anchor cable length
$L_{A,s}$	Starboard side anchor cable length
m_A	Mass of the anchor

h_w	Depth of the water
W_{USS}	Total weight of the USS
$F_{b,USS}$	Buoyancy force of the USS
M_{USS}	Total mass of the USS
m_s	Mass of the main body of the USS
m_l	Mass of the weight attached to each leg of the USS
ρ_w	Density of the water
V_{USS}	Fluid (water) volume displaced by the USS
L_S	Physical cable length
h_s	Height of the USS
d_p	Penetration depth
H	Penetration depth
h	Actual sample size
h/H	Sampling ratio
F_p	Penetration force
F_{e}	External driven force
W_b	Buoyant weight of the sampler
Q_t	Bearing capacity at the tip of the core sampler
F_t	Side friction of the core sampler
F_R	Resistance force
θ_{tl}	Toppling limit
n_c	Common mode
n_d	Differential mode
T_A	Tension of the anchor cable
$m_A g$	Weight of the anchor
θ_A	Angle between the anchor cable and the water surface
$F_{drag,wind}$	Drag force acting on the USV based on the wind
ρ_{wind}	Density of the wind
v_{rel}	Speed of the USV relative to the wind

C_d	Drag coefficient
A_{USV}	Cross sectional area of the USV
z_{cs}	Position of the lead screw
w_{cs}	Linear velocity of the lead screw
r_m	Radius of the lead screw
λ	Lead angle
θ_{lead}	Lead screw rotation
ω_{cs}	Angular velocity of the core sampler
$\Delta\theta_{cs}$	Change in angular rotation of the core sampler
Δt	Time difference
ϕ_{USS}	Roll angle of the USS
θ_{USS}	Pitch angle of the USS
ρ_{water}	Density of the water
p_1	Pressure from the bottom pressure sensor
p_2	Pressure from the top pressure sensor
h_1	Height of the bottom pressure sensor
h_2	Height of the top pressure sensor
$V_{L-bellow}$	Volume of the large rubber bellow
$V_{L-bellow,\mathrm{i}}$	Initial volume of the large rubber bellow
$V_{L-bellow,f}$	Final volume of the large rubber bellow
$V_{air,atm}$	Air volume inside of the USS at atmosphere pressure
$m_{air,atm}$	Air mass inside of the USS at atmosphere pressure
$\rho_{air,atm}$	Air density inside of the USS at atmosphere pressure
$\Delta V_{pressure}$	Volume difference because of the pressure change
ΔV_{total}	Total volume change
$\Delta V_{L-bellow}$	Volume difference of the large rubber bellow

ABBREVIATIONS

ALIVE	Autonomous Light Intervention Vehicle
AUV	Autonomous Underwater Vehicles
CG	Center of gravity
CB	Center of buoyancy
CPS	Cyber-Physical System
GPS	Global Positioning System
IMU	Inertial Measurement Unit
MCU	Motor controller unit
PRF	Purdue Research Foundation
PSD	particle-size distribution
ROV	Remotely Operated Vehicle
SAUVIM	Semi-Autonomous Underwater Vehicle
UGV	Unmanned Ground Vehicles
USS	Underwater Sediment Sampler
USV	Unmanned Surface Vehicle
UUV	Unmanned Underwater Vehicles

ABSTRACT

Sediment has a significant impact on social, economic, and environmental systems. With the need for an effective sediment management and monitoring system growing more important, a method for precisely and reproducibly obtaining sediment samples that represent the actual environment is essential for water resource management and researchers across aquatic domains (such as lakes, rivers, reservoirs, mine drainage ponds, and wastewater lagoons). Sediment sampling is usually carried out less frequently than water sampling because of the cost and labor involved. However, more frequent sediment sampling and an increase in the range of the sampling area are necessary to more effectively monitor the ecosystem and water quality.

To fill this gap, robotic approaches for sediment sampling have been introduced. However, they are not tailored to a sediment sampling method and do not focus on the quality of the sediment sample. Moreover, there are many challenges involved in developing such a sediment sampling system for the surface water of rivers, streams, lakes, ponds reservoirs, and lagoons. Thus, this study can be conducted to investigate to design and develop an uncrewed sediment sampling system for surface-water environments based on marine robot platforms that are capable of collecting intact sediment samples from a range of sediment types. As part of this study, an unmanned surface vehicle (USV) was used to deploy the underwater sediment sampler (USS) at the sampling locations. The USS adopted a core sampling method to collect the sediment samples. The specific requirements were integrated, taking into consideration the challenges posed by surface water and underwater environments, to design and develop an unmanned sediment sampling system.

The USV has two missions - *deploying* and *positioning*. Users can deploy the USV with the USS to the desired sampling area. Once the USV arrives, it has to maintain its position while launching the USS and during the sampling process. The USS also has two missions — *launching* and *sampling*. The USS must be a negative-buoyancy platform so it can reach the bottom and maintain its stability during sampling. To sample the sediment, the USS has to generate a sampling pattern. We defined and formulated challenges based on the missions of each platform.

The USV consists of three sub-systems; propulsion, launching, and monitoring system to accomplish missions. The propulsion system and launching system are necessary to accomplish deploying and positioning missions. The propulsion system is consists of two thrusters to navigate the USV. The launching system is to launch anchors for positioning and the USS for sampling. The monitoring system is to monitor and control other systems on-board via online video. The USS can generate sampling patterns based on three motions; linear, rotational, and hammering motion. We integrated servos, sensors, and mechanical components to generate three motions. The main system of the USS is completely waterproof, even for linear and rotational motion with enclosures, O-rings, and rubber bellows. Since the USS operates underwater, the water pressure causes the pressure difference between inside and outside the enclosure. We designed a pressure-equalizing system to compensate for the volume change because of sampling motions and pressure differences.

Extensive field experiments were conducted to evaluate the proposed system. Users can monitor and control the system from the base station based on all data and images from each platform. The evaluation of the system is based on the data from sensors installed on each platform. Deploying and positioning missions of the USV can be shown based on the trajectory data. Launching and sampling missions of the USS can be validated based on depth, orientation, and reaction force data.

Contributions of the proposed unmanned sediment sampling system are, 1) It is the first unmanned system with a novel design to collect the less disturbed sediment samples even from the inaccessible area and remove the potential risks of human-based sampling tasks, 2) We proposed and integrated a new sediment sampling pattern based on the sediment sampling pattern analysis to increase the quality of sediment samples by minimizing disturbances, and 3) The proposed unmanned sediment sampling system is the first step toward the autonomous environmental monitoring system for more effective environmental monitoring. This proposed system has many potential elements that can be a total solution for robotic environmental monitoring in addition to other features such as water sampling system, and various types of sensing system.

1. INTRODUCTION

Sediment is also an important component in the natural geochemical cycle and moves from land to oceans by river systems [1]. Sediment consists of solid particles (mineral and organic) that can be transported by water and eventually deposited on the bed or bottom of a body of water [1]. The importance of effective sediment management in water bodies around the globe is increasing because of its significant impact on social, economic, and ecological systems. Significant challenges exist when sampling in contaminated water bodies or locations that are difficult to access which make manual sediment collection via boat, wading, or diver-assisted collection impossible. Effective sediment management can be achieved through advancements in sediment monitoring systems. The baseline of a sediment monitoring system is sediment sampling. Sediment sampling is also necessary in a variety of other areas, including water quality monitoring, agriculture, mineralogy, marine geology, industries, and other engineering applications.

1.1 Motivation and Goals

Generally, sediment samples are collected from the bottom boundary layer (bed sediment) through manual sampling methods which involve potential problems such as the sediment sample disturbance problem, significant human labor, considerable expense, and potential safety risks (Fig. 1.1(a), [2]). During the sediment sampling task, minimizing the sediment disturbance during sampling, transportation, and storage is critical. Human operators follow the field manual to reduce the risk of disturbance and contamination [3]–[5]. However, there might be a chance that hard to maintain the integrity of the sediment samples because the performance of the sediment sampling can be vary depending on the human operator. This fact may require trained personnel with experience for every sediment sampling event. In some cases, we have to consider sediment sampling from inaccessible areas. For example, rivers with high flow rate, it is hazardous for human operators to access to the required sampling point. This kind of environment makes it difficult to collect samples manually and requires additional equipment such as an electrical cable reel, a boat (or ship), and additional human resources (Fig. 1.1(b))[6][7]. Moreover, in severely polluted environments,

sediment sampling presents additional challenges and cannot be implemented without the proper equipment such as personal protective equipment (PPE) [8]. These factors lead to a significant cost for sediment sampling which reduces data availability. Also, current sediment sampling approaches requires intensive human labor and human operators have to endure potential hazardous threats.

Recent advances in robotic technologies have been introduced to fill the gaps between existing methods and challenges, and to propose solutions that can be both economical and effective in sediment sampling. Previous robots with sediment sampling capability were primarily intended for use in oceanic environments [9]–[13]. They were large and heavy because of the typical conditions found in the open ocean and required a support vessel to carry them to the sampling location. A two-stage remotely operated underwater vehicle (ROV) for sediment sampling was introduced to increase the sampling capability [11]. For practical use in surface water bodies like rivers, streams, lakes, and ponds, reducing the scale was necessary. ROVs have been developed to work with sediment sampling equipment to sample sediment from the surface water environment [14]–[16]. However, these robotic systems were developed, with the primary focus on the navigation, path planning, and orientation control of underwater robotics. Also, less consideration was given to the impact of the sampling technique on the integrity of the sample collected thus, it is not appropriate to sample high-quality sediment samples with these approaches. This fact is the biggest limitation of the current existing systems.

Understanding the needs of researchers, characteristics of the sediment itself, and physical constraints of the body of water is imperative for developing a robust robotic sediment sampling system that recovers high-quality samples. A clear understanding of how the specific sediment type interacts with the sampling equipment becomes more critical when sampling with robotic systems as compared to manual sampling with human oversight. Traditional methods of manual sampling, particularly those in shallow water with the wading method, allow the worker to change approaches rapidly based on the sediment compaction, presence of rocks or plant roots, or simply different soil textures. However, with robotic samplers, these conditions need to be assessed and the penetration force adjusted to sample to the desired depth. This requires an analysis of the resistance force, which controls the

(a) Human-based sediment sampling (b) Sediment sampling from the boat

Figure 1.1. Examples of human-based sediment sampling: (a) Core sampling by operator [17] and (b) Manual sediment sampling from boat [18].

stability of the sampling platform. In addition, disturbances such as deformation of the sediment layers or contamination by the water during the sampling process, that affect the physical, geochemical, and biological conditions of the sample should be considered. For example, deformation of the sediment sample structure [19] or polluted by the water from different layers. Thus, minimizing disturbances to samples is both critical and challenging.

To meet these challenges, an uncrewed sediment sampling system has been developed based on the unmanned surface vehicle (USV) and underwater sediment sampler (USS). The main objective of the USV is to carry the USS to the desired sampling area and then maintain its position within the maneuvering range while launching the USS to the bottom of the body of water and sampling the sediment. The core sampling method was adopted for the USS to extend the use of the sampled sediment by minimizing the disturbance while sampling. The overall goal of this research is to design and develop an uncrewed sediment sampling system for sediment sampling from surface water bodies based on a USV and USS, as shown in Fig. 1.2(b), and 1.2(a). The overall goal included three sub-goals. First, we develop an effective sediment sampling procedure that is capable of deploying unmanned systems (USV and USS) into the unknown environments such as unknown depth, unknown properties of the sediment, or uneven terrain based on challenges. Second, we integrate highly flexible sediment sampling patterns and self-adaptability mechanisms to investigate thoroughly collecting sediment samples' reliability and quality. Although full testing of

sediment sample quality should be undertaken by a soils expert and is not a component of this dissertation, the effectiveness of the flexible mechanisms is tested as reported in Chapter 3 and Section 5.1. Lastly, we conduct extensive field experiments to evaluate and validate the performance of the USV and USS by collecting sediment samples from a real environment and verifying the proper and flexible operation of the system as a whole.

1.2 System Overview: Uncrewed Sediment Sampling System

Developing an uncrewed sediment sampling system based on the USV and USS was challenging because of unknown environmental factors such as the wind, current, water pressure, unknown sediment, and uneven terrain. Overall procedure of the uncrewed sediment sampling system can be summarized into five steps. First, we deploy the USV with the USS to the desired sampling point. Second, the USV have to maintain its position while launching the USS, sampling the sediment, and retrieving the USS. Third, we launch the USS to the bottom of the water. Fourth, the USS have to penetrate the sediment to collect the sample of it. Fifth, we retrieve the USS back to the USV and return the USV to the base station. We can define missions of each platform based on the procedure of the uncrewed sediment sampling system and each platform has two missions. Missions of the USV are *Deploying* and *Positioning*. Missions of the USS are *Launching* and *Sampling*. This section outlines the design criteria for the uncrewed sediment sampling system based on the challenges to be considered during missions.

1. **Deploying - USV**

   The first mission of the USV is to carry the USS to the desired sampling area using its navigation capability based on the propulsion system. The size and load capacity of the USV must be large enough to load the USS, including other components of the USV, because the USV is the main carrier to achieve all missions.

2. **Positioning - USV**

   The main objective of the positioning is to minimize the maneuvering of the USV. Maintaining the position of the USV by minimizing the maneuvering in the sampling location is critical during the sediment sampling process. Otherwise, disturbances

(a)

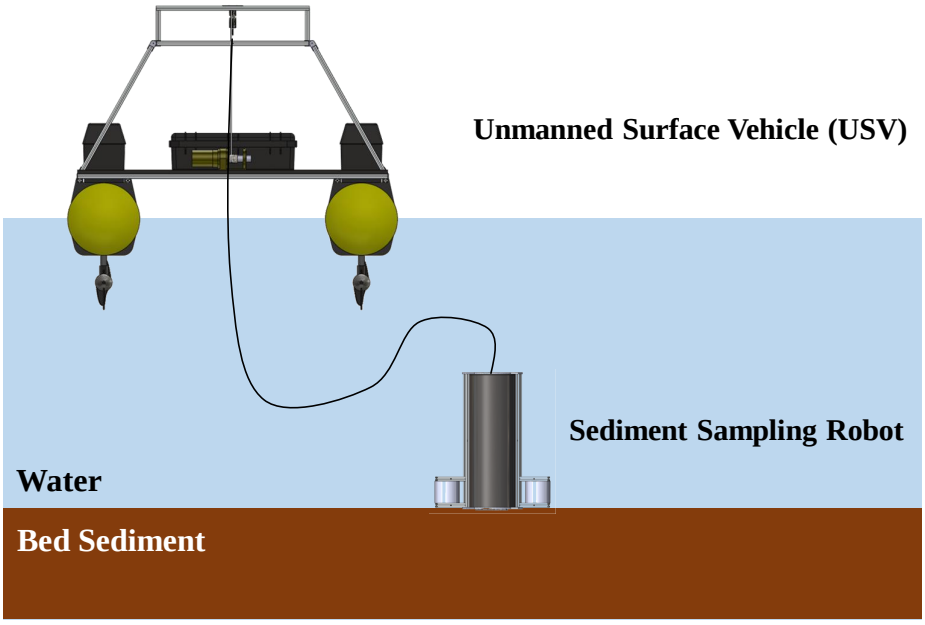

(b)

Figure 1.2. Proposed uncrewed sediment sampling system based on the Unmanned Surface Vehicle (USV) and Underwater Sediment Sampler (USS), (a) at the field, and (b) cross-section view when the USS is launched.

such as wind or current can drag the USV away from the sampling location, and we cannot launch the USS to sample the sediment.

3. **Launching - USS**

   The USS must be a submersible platform that can submerge down to the bottom of the water by its weight. The components of the USS must be waterproofed since the workspace is underwater. The volume inside of the USS changes because of the linear motion during sampling and the water pressure as the USS submerges. The USS must equalize the pressure inside and outside the USS to compensate for the volume change. The stability issue arises when the USS is submerging and landing due to the water current, unknown sediment, and uneven terrain.

4. **Sampling - USS**

   The main goal of deploying the USS is to overcome the environmental challenges and sample sediment at the required quality and quantity. Because the target sediment was the sediment at the bottom of a body of water, many challenges arise when designing the USS. For example, how much penetration force is required to penetrate to the desired depth which determine the amount of sediment? Is the size of the sediment sample important to evaluate the system? Also, the penetration force creates a reaction force, which can be the major factor causing the instability of the USS. Thus, it was necessary to devise systems to measure and control the penetration force and orientation of the USS.

1.3 Contributions

We expect the contributions of this research to be as follows.

1. **Uncrewed Sediment Sampling System with Novel Design**

   Currently developed unmanned systems for underwater sediment sampling are typically based on a single robot platform, such as a remotely operated vehicle (ROV). ROV-based sediment sampling systems have limitations because of the buoyancy condition, which is 'neutral buoyancy.' ROVs need an additional system that cre-

ates the down-force to facilitate negative buoyancy, such as thrusters or a ballast system. These systems installed a stationary coring tube and penetrated the sediment by generating the down-force using thrusters. However, this sampling method may cause significant disturbances to the sediment sample because of the unstable orientation and penetration. The proposed idea is to utilize the multi-robot team consisting of the USV and USS, which can reduce the limitations of existing approaches. The USV is the main control station, transports and launches the USS. The USS is the sole platform for underwater sediment sampling. This configuration can eliminate the limitations of the buoyancy force by making the USS a negative-buoyancy platform. Furthermore, the USS can be more sophisticated to sample less disturbed sediment samples. In addition, a proposed uncrewed sediment sampling system aims for a low-cost design: 1) we utilized commercially available components and integrated them into the system, 2) we adopted rapid proto-typing methods such as 3D printing technology to fabricate components for the system, and 3) we installed low-cost sensors which have enough performance to evaluate the system.

2. **Integration of Sediment Sampling Pattern**

   This system aims to collect sediment samples by minimizing the disturbance and securing the sediment by preventing the risk of contamination. We conducted extensive indoor sediment sampling pattern tests to find the effect of each motion, which determines the sampling pattern; this involved analyzing the amount of the sediment collected, reaction force, and work carried out. We considered the results of the preliminary study of the sampling pattern. During the preliminary study, we tested three sampling patterns with three types of sediment to find the optimal sampling pattern based on the objective of sediment sampling. The USS can currently generate the sampling pattern based on three different motions: linear motion, rotational (direction changing), and hammering motion. Furthermore, we could generate several sampling patterns depending on the input variables of each motion. The main objective of the sampling pattern analysis was to find the effectiveness of each motion that generates the sampling pattern by analyzing the

reaction force as well as input and output energy. We compared the reaction force of the sampling patterns to explain how different motions affect the reaction force. Moreover, the reaction force was a critical factor in determining whether the USS could maintain its stability or not. The input energy was based on the input variables for generating motion, and we considered the reaction force to calculate the output energy. We derived the system's energy efficiency during sampling based on the input and output energy.

3. **First Step Toward an Autonomous Environmental Monitoring System** Development of the uncrewed sediment sampling system can be the cornerstone of the autonomous environmental monitoring system. This system consisted of multi-robot team (USV and USS) which can cover both water surface and underwater environment. The advantages of the multi-robot team can be actively used not only for sediment sampling but also for other sampling and sensing features. The multi-robot team with the USV and USS can have many potential elements that can be a total solution for autonomous environmental monitoring in addition to other features such as water sampling system, and various types of sensing system. Specifically, by adding the water sampling system to the USS, we can collect water samples even from the different depth since the USS is submerging vertically through the water. We can integrate various sensors such as pH [20], turbidity [21]–[24], total organic carbon (TOC) [25], [26], conductivity [27], [28], residual chlorine [29], or oxygen-reduction potential [30] senor to the USV and USS for collect various types of data both from surface water and underwater. Also, we can install sensors for bathymetry mapping [31]–[33] such as sonar [34], [35] or acoustic doppler [36], [37]. Based on the terrain data, we can build more precise data of the sampling area.

1.4 Dissertation Outline

This dissertation consists of six chapters, including this introductory chapter, and is organized as follows:

Chapter 2 presents a review of the literature on the use of underwater robotics for an USV and unmanned underwater vehicle (UUV), sediment sampling method and equipment, and robotic approaches for sediment sampling. Chapter 3 introduce the results of a preliminary study to provide a better understanding of the sediment and sediment sampling. Chapter 4 introduces the design of the uncrewed sediment sampling system based on the system requirement. The mechanical and electrical design of the USV and USS are presented, along with the software architecture of the proposed system. Also, sampling pattern analysis introduced based on the analytical approach. Chapter 5 presents the results of the sampling pattern test in the lab environment and the setup and results of a field experiment used to evaluate the proposed system. Chapter 6 covers three discussion topics, which are Design of the uncrewed sediment sampling system, Field experiment, and Autonomous sediment sampling system. Finally, the conclusions of this research and future research directions are presented in chapter 7.

2. BACKGROUND

This section introduces some basic information about the use of underwater robotics for unmanned marine vehicles as a preliminary study to design and develop an uncrewed sediment sampling system for a water environment. To understand sediment and sediment sampling, different types of sediment sampling devices and methods were studied. Robotics technology for sediment sampling is also introduced to design a more effective uncrewed sediment sampling system.

2.1 Underwater Robotics for Unmanned Marine Vehicles

2.1.1 Unmanned Underwater Vehicle (UUV)

Underwater robotic vehicles are referred to as Unmanned Underwater Vehicles (UUVs); Remotely Operated Vehicles (ROVs), and Autonomous Underwater Vehicles (AUVs) [38]. ROVs have been developed to explore underwater environments such as oceans. Primarily, human-occupied submersibles have been used for scientific exploration. As underwater technology progressed, ROVs started taking over many tasks that had been assigned to manned submersibles. The first ROV was developed in 1953 (called POODLE), and in the early 1980s, the scientific research on ROVs began in earnest [39]. Many ROVs have conducted seafloor exploration and obtained superior data. The Jason 2 (Fig. 2.1(a)) manufactured by the Woods Hole Oceanographic Institution (WHOI) is a good example of an ROV for scientific use [40]. It is mainly used for deep sea exploration (about 6,500 m) and is equipped with sonars, video and image capturing systems, lights, and various types of sampling systems. Applications of ROVs have expanded with the growth of the offshore oil and gas industry. ROVs have been deployed to perform frequent inspections and support various tasks such as drilling operations, valve actuation, and the maintenance of components [40][41]. The term ROV indicates an underwater platform tethered to an operator in a ship or submarine [41]. The purpose of the tether is to provide power and control commands to the vehicle and receive data from it. However, the limitations of this method increase with the depth

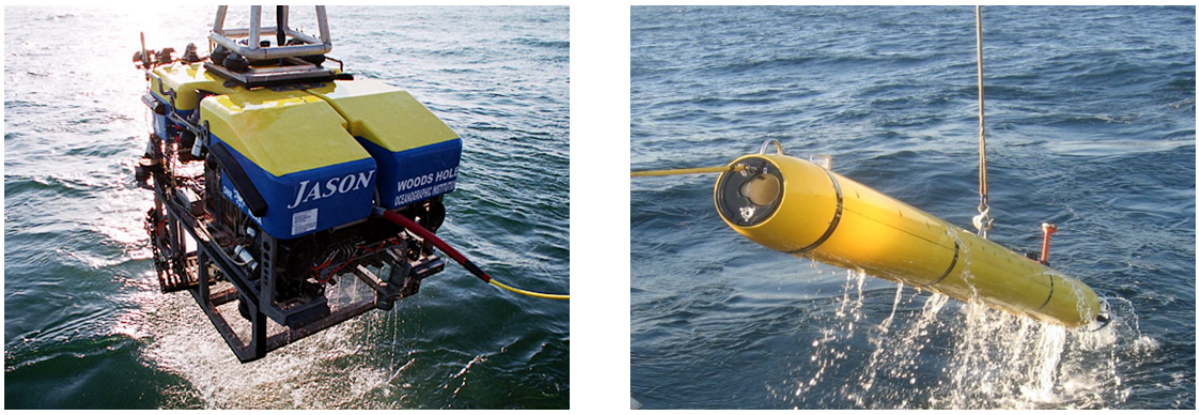

(a) Jason2 (WHOI)

(b) Bluefin-12D

Figure 2.1. Different types of unmanned underwater vehicles: ROV (left) [43] and AUV (right) [44].

of the ROV because of the long tether required and the high manufacturing and operating costs [39][42].

AUVs are untethered underwater vehicles that carry their own power system and can overcome the limitations of ROVs in some areas [40]. Fig. 2.1(b) depicts an example of an AUV from Bluefin Corporations. Currently, scientific surveys, oceanographic sampling, and under-ice surveys are the major uses of AUVs [40]. The use of AUVs can also include military applications such as mine detection and some surveillance tasks [40]. Because AUVs only rely on the acoustic communication, they are incapable of continuous human control [40]. Limited communications require that AUVs operate fully autonomously; however, they still cannot replace ROVs, which are capable of sampling, and complex and challenging manipulation tasks.

In summary, ROVs and AUVs have been developed in many areas such as industry, scientific research, the military, and engineering research [42]. There are hundreds of ROVs and AUVs in operation and many manufacturers offer turnkey systems for specific tasks. In the future, the design and development of autonomous manipulations will remain a challenge, which will be met by Semi-Autonomous Underwater Vehicles for Intervention Missions (SAUVIMs) and Autonomous Light Intervention Vehicles (ALIVEs) [40][45][46].

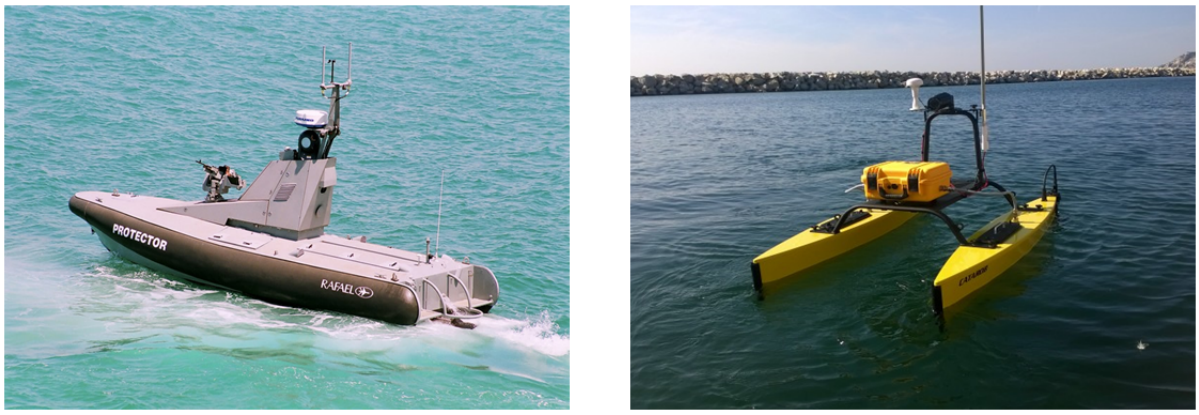

(a) Rigid hull

(b) Twin hull

Figure 2.2. Different types of unmanned surface vehicles (a) Protector USV (NAVY) [51], (b) Catarob-ATS-03 [52].

2.1.2 Unmanned Surface Vehicle (USV)

Initially, USVs were developed for the military [47]. Currently, the applications of USVs have expanded to scientific and engineering research. With advanced GPS (Global Positioning System) systems, as well as higher bandwidth and long-range wireless communication technologies, the capabilities of USVs have grown rapidly [31]. The main military applications include harbor security and minesweeping. USVs for the military are usually based on traditional boats such as a rigid hull inflatable (Fig. 2.2(a)) with control, navigation, and communication systems [31][48]. For commercial and scientific uses, USVs became more compact, and various types of hull designs have been developed such as a twin hull platform (Fig. 2.2(b)). Rapid mapping in a riverine environment to generate bathymetric maps is the one of the useful applications in the scientific area [49]. In this case, USVs should have autonomous navigation and maneuvering capabilities. However, one of the limitations of a small USV is its coverage area. To overcome this limitation, multiple USVs are operated together as a team [50]. For the further study of USVs, renewable energy technologies have been introduced such as wind, wave, and solar powered USVs.

(a) Grab sampler

(b) coring tube

Figure 2.3. Sediment sampling devices (a) Grab sampler [54], (b) coring tube [55].

2.2 Traditional Sediment Sampling Equipment and Methods

Fluvial sediment is sediment that is transported by, suspended in, or deposited in the bed of a river by water [53]. Fluvial sediment is transported by water as suspended sediment or as bed load sediment. If the density of the sediment particles is greater than that of the water, fluvial sediment is deposited in the bed of the river. To observe suspended sediments, a sampler that can collect a water-sediment mixture from the water surface is needed. For bed load sediment collection, in general, a grab or dredge sampler is used. In the case of the bed sediment, coring tubes are commonly used for sample collection.

Traditional sediment sampling has been done manually by users. However, sampling tasks include more than just collecting the sediment. There are many different types of sampling equipment and methods for proper sampling. Sediment samples can be collected using different types of equipment and various methods depending on the desired depth, type of sample, and volume of sample needed. Most sediment sampling equipment is designed to collect a specified amount of sediment from a required depth with minimal disruption of the integrity and no contamination of the sample [56]. It is important to select the right device because maintaining the integrity of the sediment sample is the most primary concern. If the

structure of the sediment is disrupted, its physical, chemical, and biological characteristics will influence the availability of contaminants and toxicity of the sediment.

The purpose of collecting sediment samples is to analyze the physical, chemical, biological, and toxicological conditions of water resources. Defining the purpose of the sampling is essential and must be done before the sediment sampling planning. The typical purposes of sediment sampling include bioassays and biosurvey sampling, contaminant source identification, and monitoring pollutant discharge, sediment oxygen demand, trace elements and organic contaminants, and sediment dynamics [57], [58].

It is important to select the most appropriate sampling instrument and method based on the sampling objective, type of sediment, and sampling location (i.e., water depth) [57], [59], [60]. There are three types of sediment sampling equipment: grab samplers, coring tubes, and dredge samplers. A grab sampler is shown in Fig. 2.3(a), Typically these are used for sediment on the surface to find the horizontal distribution of its characteristics. This sampler consists of a set of jaws, which are shut when it reaches the bottom to collect the sediment. The advantages of a grab sampler are that it is relatively easy to handle and operate, and it can collect a large sample. coring tubes (corer) can be used mainly in three ways, to collect sediment samples for geological characterizations, to investigate the actual input of contaminants to aquatic systems, and to characterize the depth of on-site contamination (Fig. 2.3(b)). Typically, corers are used when maintaining the integrity of the sediment is critical. It is less disruptive than grab or dredge samplers. Limiting the oxygen exchange is important to maintain the oxygen-free environment. The disadvantages of corers are the relatively small volume compared to the given depth and the plugging or corroding issue when the friction of the sediment is not sufficient for it to stay in the tube coring tubes can be selected based on the water depth and core size [61]. The typical core sampling methods include gravity coring, box coring, hammer coring, and vibro-coring, which make use of a free fall (weight), a piston, or hydraulic energy [62], [63].

2.3 Robotic Technologies in Sediment Sampling Task

In extraterrestrial research to sample Martian and Lunar soil via automated systems, focus has been placed on soil mechanics to overcome the friction between the drill mechanism and soil [64]–[70]. Those studies demonstrated that an understanding of the sampling environment and material properties is essential to the design and development of an automated sampling system.

In the case of underwater sediment sampling, however, few studies have been published [71], which highlights the need for a thorough understanding of the underwater environment [72], [73] and sediment sampling [74], [75] to sample sediment effectively with automated systems, particularly in more challenging environments.

Sediment monitoring in an aquatic environment is critical to preventing contamination during the analysis of the chemical properties, physical properties, and historical conditions of the sediment. In order to reduce the processing time and risks of manual sampling, unmanned platforms such as ROVs and Unmanned Ground Vehicles (UGVs) have been implemented to complement the sample system.

For example, an underwater vehicle with an attachable coring tube was developed ([14]). The main goal was to collect sediment with an existing corer (e.g., the Craib corer) by generating a negative buoyancy force with the ROV. The ROV had two buoyancy regulators to generate a downward force, which supported corer penetration. However, this system still required an anchor to hold the ROV on the bottom, as well as human operators to operate the system from a ship on the surface. An operator-portable ROV with sample coring cylinders has also been introduced [15], [16]. The ROV was relatively lightweight (34 kg, air) compared to previous platforms and had a length of 2.3 m. Its thrusters allowed maneuvering in the water but it could only penetrate the sediment to a depth of 0.16 m because of its limitations. The vertical force created by the ROV caused a reaction force from the sediment that could affect the stability of the ROV and the sampled sediment amount. Vertically-attached thrusters generated thrust forces to overcome the reaction force created by the sampling process. Horizontally-installed thrusters controlled the orientation of the ROV to allow it to take sample at the specific location as determined by the human opera-

(a) Remotely operated underwater vehicle (ROV) for Sediment Sampling

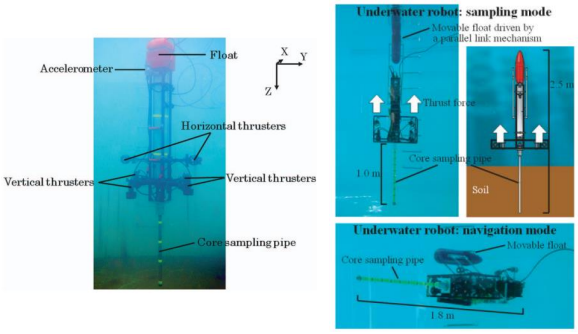

(b) Human portable ROV

(c) Unmanned ground vehicle (UGV) for sediment sampling

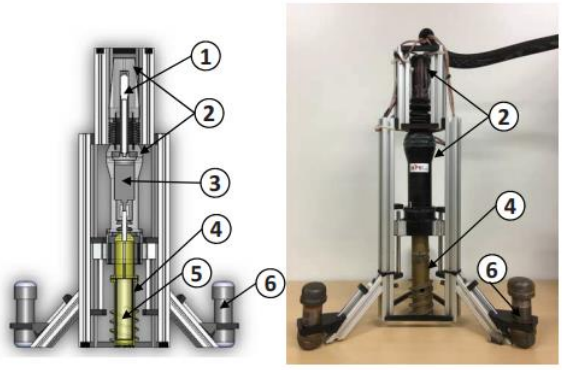

(d) Underwater sediment sampler

Figure 2.4. Unmanned systems for sediment sampling: (a) Underwater robot for sediment sampling [14], (b) Human portable underwater robot for sediment core sampling [15], [16], (c) UGV for sediment sampling [76], and (d) Sediment sampling robot [77].

tor. However, because of the limitations of the electric thrusters, the sediment penetration depth in field experiments was limited to approximately 0.16 m [15]. An alternative method involved cooperation between human operators and other types of unmanned platforms [76]. Based on the image from a high-resolution camera attached to an Unmanned Aerial Vehicle

(UAV), an operator decides which specific mudflat to sample. Then, the UGV travels to the desired location and samples the sediment using a cylindrical container with a diameter of 6 *cm* and length of 45 *cm*. The core performs vertical and rotational movements to sample the sediment. A compliant 6-DOF robotic arm attached to the UGV is used to exchange up to nine cylindrical container samples from various locations. However, this method is limited to a sub-aerial inter-tidal environment because of the limitation of the UGV which is not designed for an underwater environment.

Most robotic sediment sampling systems are more focused on underwater platform design and control ([14]–[16]). However, an analysis of the interaction between the sediment sampling robot and the sediment is critical to sample the sediment efficiently via a robotic sediment sampling system. For example, the force acting on a robotic sampler during the sampling process depends on the sediment and should be quantified to ensure effective sampling [71]. It is also crucial to maintain the stability of the underwater sediment sampler during the sampling process by countering the linear and rotational motion of the core [77]. A feedback controller was implemented to control the stability by measuring the residual between the reference and actual orientations. A closed-loop control system showed better performance, including a shorter sampling time, better stability, and better sediment weight [77].

The main goal for the uncrewed sediment sampling system is to develop the most effective sediment sampling system by maintaining the quantity and quality of the sediment. The experimental data can be integrated to enhance the design of the robotic sediment sampling system. Collecting data and suggesting new methods can be done not only for robot developers but also for environmental scientists who are attempting to improve sediment monitoring systems. Understanding the sampling environment and characteristics of the sediments should be the starting point to develop a robotic sediment sampling system.

3. SEDIMENT SAMPLING METHODS: A PRELIMINARY STUDY

This chapter contains the material from the previously published paper. The material has been added with the consent of the all the authors on the paper.

- J. H. Bae, W. Jo, J. H. Park, R. M. Voyles, S. K. McMillan, and B.-C. Min, "Evaluation of sampling methods for robotic sediment sampling systems," *IEEE Journal of Oceanic Engineering*, vol. 46, no. 2, pp. 542–554, 2021.

3.1 Preliminary Study

Experimental study on sediment sampling task has been conducted to evaluate sediment sampling methods for an autonomous sediment sampling system. We developed a sediment sampling test-bed to measure and analyze parameters during the sampling process. The general configuration of the proposed sediment sampling test-bed, including its two motors, load cell, sampling core, and sediment container is shown in Fig. 3.1.

3.1.1 Sediment Sampling Platform Specifications

The sampling patterns of the sediment sampling platform are based on a combination of motions by Motor 1 (M_1) generating a linear motion and Motor 2 (M_2) generating a rotary motion. The M_1 encoder measures the linear velocity of the sediment sampling platform while the M_2 encoder measures the angular velocity of the sampling core. A commercial plastic (PVC) core liner for sediment sampling with an outer diameter of 50.8 mm (inner diameter of 47.8 mm, Wall thickness = 1.5 mm) and a length of 304.8 mm[1] was used as the sampling core liner. A check valve was installed on the core liner to prevent the sampled sediment from flushing out of the core liner upon retrieval. A sediment container is located on the bottom of the sediment sampling platform. The signals monitored by the sediment sampling platform are shown in Table 3.1(a) and the specifications of the sediment sampling platform are shown in Table 3.1(b). The load cell measures the penetration force during the

[1] ↑https://www.ams-samplers.com/2-x-12-plastic-liner.html

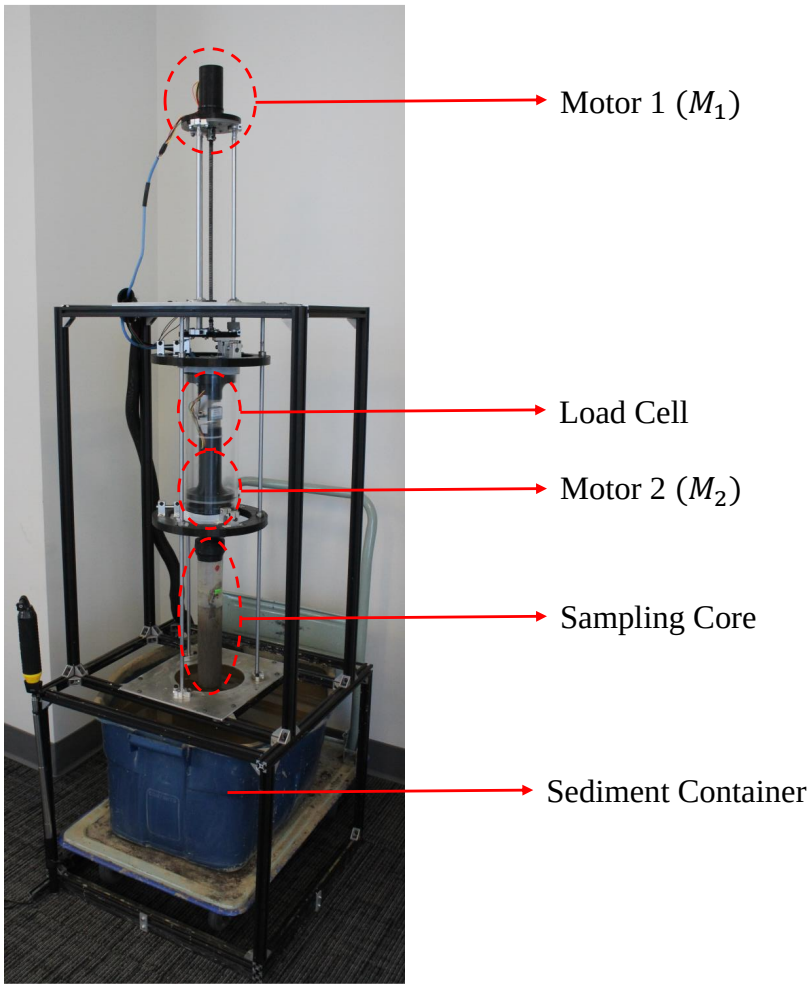

Figure 3.1. A sediment sampling platform composed of two 12V DC motors with encoder (M_1 & M_2), load cell, sampling core, and sediment container. Motor 1 (M_1) generates a linear motion and Motor 2 (M_2) generates rotary motion. The load cell measures the force during the sampling process. The motion of the sampling core is based on the combination of Motor 1 (M_1) and Motor 2 (M_2).

sampling process. Current sensors are installed to measure the input current of each motor. Specifically, this platform has a maximum (no-load) linear velocity of 38 mm/s and angular velocity of 12 rad/s. The maximum penetration force is 15 kg and the current limit is 3 A. Its vertical distance range is 0 to 300 mm.

Table 3.1. Signals monitored by the sediment sampling platform and specifications of the sediment sampling platform.

(a) Monitoring signals

Measuring sensor	Signal monitored
Motor 1 (M_1) encoder	Linear velocity (v)
Motor 2 (M_2) encoder	Angular velocity (ω_r)
Load cell	Penetration force (F_p)
Current sensor	M_1 & M_2 current (C_1, C_2)

(b) Specification

Specification[unit]	Range
Linear (M_1) velocity [mm/s]	0 - 38
Rotational (M_2) speed [rad/s]	0 - 12
Rotational (M_2) frequency [Hz]	0 - 50
Penetration force [kg]	0 - 15
Driving distance [mm]	0 - 300
Current sensor [A]	0 - 3

3.1.2 Sampling Pattern

We applied three different sample sediment coring patterns based on our empirical studies: linear, helical, and an oscillating zig-zag motion. The linear motion is the core samplers' default pattern. The helical motion is the drilling pattern made by manual ground-drilling augers. The zig-zag motion rotates the core liner left and right, recursively. A demonstration of these patterns can be found from our experiment video at https://goo.gl/rhctu9.

Although only three parameterized patterns are explored in this study (see Fig. 3.2), the sediment sampling platform can generate an arbitrary blend of the two motions induced by motors M_1 and M_2; M_2 is connected directly to the sampling core for rotary motion and M_1 drives the combined corer plus M_2 mechanism up-and-down for linear motion. The linear motion (Fig. 3.2(a)) generated by M_1 is vertical motion without rotation ($\omega_r = 0$). The helical motion (Fig. 3.2(b)) and zig-zag motion (Fig. 3.2(c)) are the combinations of M_1 and M_2. The helical motion is generated by combining linear motion while the sampling core is rotating. The zig-zag motion is composed of two different helical motions: both right-hand and left-hand motions combined with the linear motion to drive the coring tube into

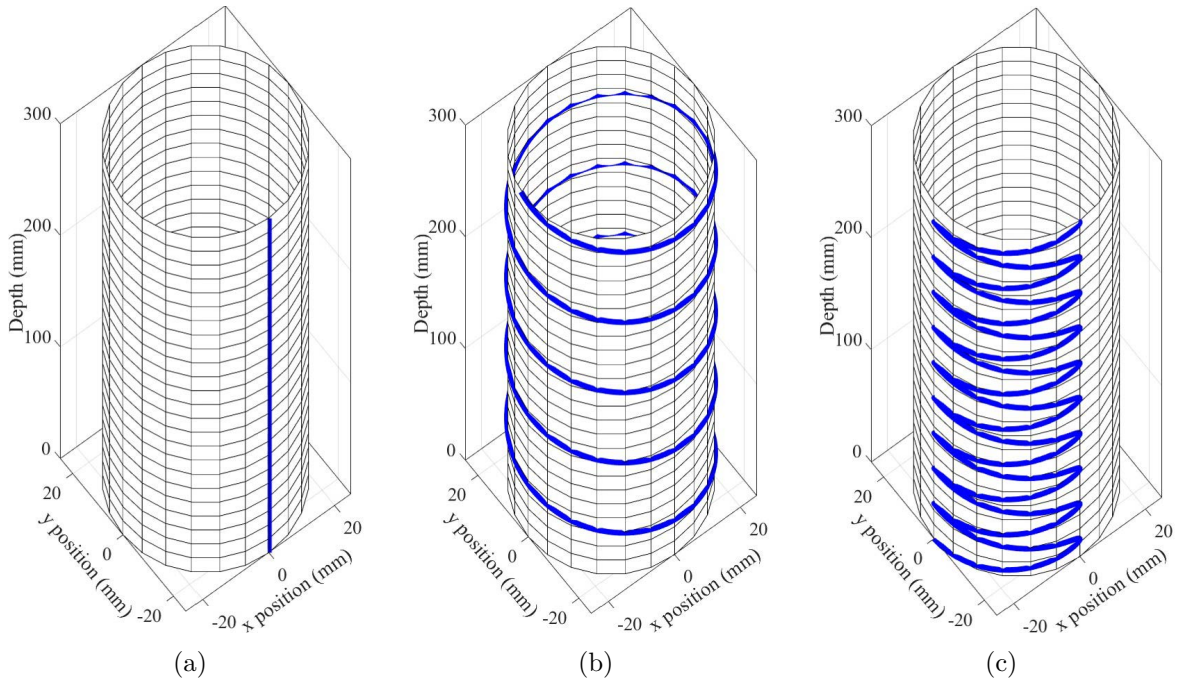

Figure 3.2. The sediment sampling patterns applied in this study: (a) Linear motion, (b) Helical motion, and (c) Zig-zag motion.

the sediment. The changing rate of the rotational motion direction depends on the angular velocity, ω_r, and the frequency of the motor input signal, f_r. Let $p(x, y, z)$ be the arbitrary point on the surface of the sampling core. The position of the point can be expressed as Eq. 3.1, 3.2, and 3.3, respectively, depending on a motion where r is the radius of the sampling core, ω_r is the angular velocity of the sampling core, and v is the feed rate, which is the linear velocity of the sampling core.

Pattern 1: Linear motion

$$\begin{cases} x = rsin(\omega_r t) = 0 \\ y = rcos(\omega_r t) = r \\ z = -vt \end{cases} \tag{3.1}$$

Pattern 2: Helical motion

$$\begin{cases} x = rsin(\omega_r t) \\ y = rcos(\omega_r t) \\ z = -vt \end{cases} \tag{3.2}$$

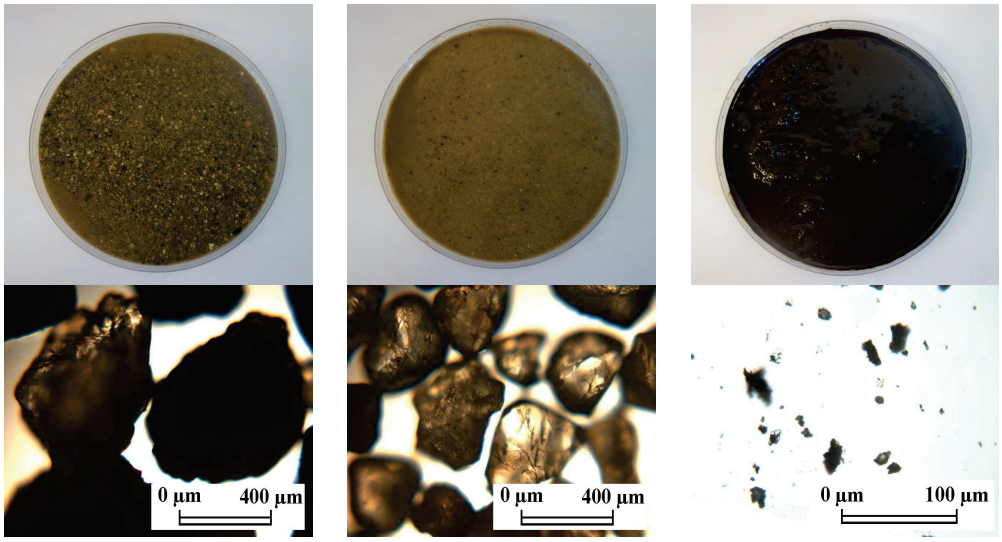

(a) (b) (c)

Figure 3.3. Types of sediments (a) Coarse sand (D50=409.85μm), (b) Medium sand (D50=408.58μm), and (c) Silt (D50=45.26μm).The top panel shows each sediment type at 100% saturation in a petri dish and the bottom panel is a microscopic view of particles observed polarizing microscope (*Leitz Laborlux 12 POL S*).

Pattern 3: Zig-zag motion

$$\begin{cases} x = r sin(10\omega_r \, |sin(0.1 f_r t))|/f_r) \\ y = r cos(10\omega_r \, |sin(0.1 f t))|/f_r) \\ z = -vt \end{cases} \tag{3.3}$$

3.1.3 Classification of Sediment

We used three types of sediment classified by the particle-size distribution (PSD) (Fig. 3.3) [78][79]. We defined sample sediments (i.e., coarse sand, medium sand, and silt) based on the USDA soil texture classes and subclasses used a laser particle counter (Mastersizer 3000, Malvern Panalytical, Malvern, UK) to provide precise particle distribution of the sediments (Fig. 3.4).

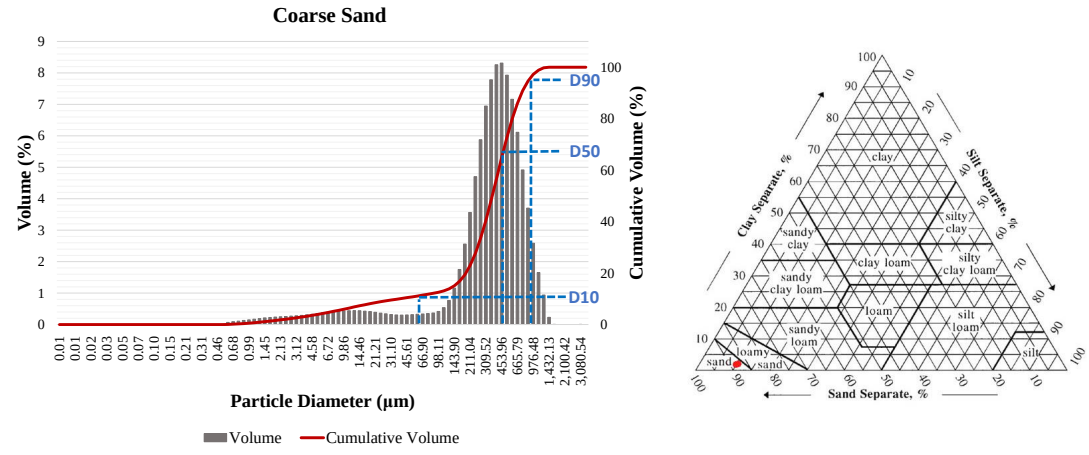

(a)

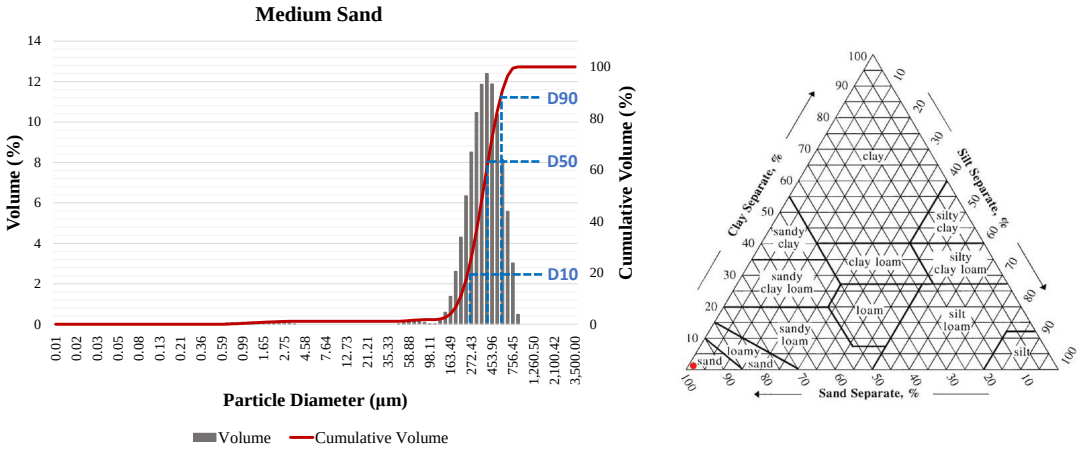

(b)

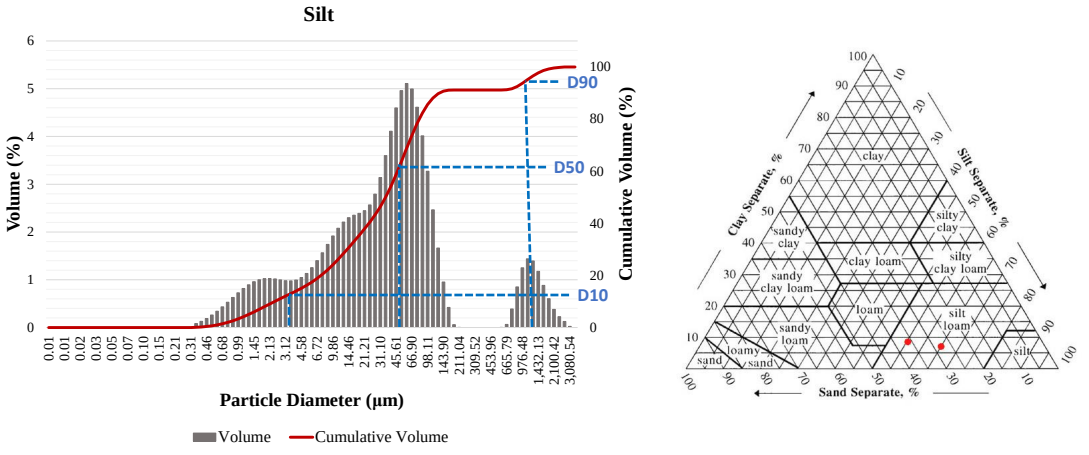

(c)

Figure 3.4. The particle distribution of each sediment (left): (a) Coarse sand, (b) Medium sand, and (c) Silt. Sediment classification ternary diagrams (right) depict the texture of each sediment based on the particle-size distribution (PSD) results and red dots indicate the type of the sediment.

3.1.4 Multiple Objective Optimization

We defined the optimal sediment sampling pattern as the one that collects the greatest amount of sediment with greater work efficiency. Therefore, we consider this as a multiple objective optimization problem in order to find the optimal sediment sampling pattern based on the type of sediment. A common approach to optimize the multi-objective problem is to minimize the sum of the individual objectives using the weighted-sum method [80][81]. A weighting factor indicates the importance of each objective. We also implement this as a discrete optimization problem because we are limited in the number of design iterations of the physical systems that we are able to create and test. While we recognize there are an infinite set of potential solutions, it is impossible to run the experiment iteratively by continuously increasing the input parameters. Hence, we can express the objective function as follows:

$$\begin{aligned} &\textit{Minimize}: \quad F(\mathbb{X}) = w_1 f_1(\mathbb{X}) + w_2 f_2(\mathbb{X}) \\ &\textit{Subject to}: \; x_{\mathrm{i}} \in \mathbb{X}, (\mathrm{i} = 1,2,3); \\ &\qquad\qquad w_{1,2} \geq 0 \text{ and } w_1 + w_2 = 1; \\ &\qquad\qquad C_{1,2} \leq C_{max} \end{aligned}$$

where $\mathbb{X}$ is a finite set,

$$\mathbb{X} = \begin{bmatrix} x_1 \\ x_2 \\ x_3 \end{bmatrix} = \begin{bmatrix} \nu_1 \\ \omega_r \\ f_r \end{bmatrix} \tag{3.4}$$

where $x_1 = \nu_1$ is the linear velocity (mm/s) of Motor 1 (M_1), $x_2 = \omega_r$ is the angular velocity (rad/s) of Motor 2 (M_2), and $x_3 = f_r$ is the direction changing frequency (Hz) of Motor 2 (M_2). w_1 and w_2 are finite weighting factors. C_1 and C_2 are the values of the electrical current consumed by M_1 and M_2, respectively. C_{max} is the value of the maximum current

allowed for each motor that prevents the motors and systems from overload damage. We can express $f_1(\mathbb{X})$ and $f_2(\mathbb{X})$ in the following functions:

$$f_1(\mathbb{X}) = \left(\frac{m_s(x_1, x_2, x_3)}{V_d} \right)^{-1} \tag{3.5}$$

$$f_2(\mathbb{X}) = \left(\frac{\int F_p(x_1, x_2, x_3) ds}{t} \right)^{-1} \tag{3.6}$$

where $f_1(\mathbb{X})$ is a reciprocal function of the density of the sampled sediment and $f_2(\mathbb{X})$ is a reciprocal function of the power of the sediment sampler. The goal of the experiment is to minimize $f_1(\mathbb{X})$ and $f_2(\mathbb{X})$. Minimizing $f_1(\mathbb{X})$ and $f_2(\mathbb{X})$ identifies the pattern with the largest sampled mass and the most efficient work performed by the sampler. The variable m_s is the mass of sampled sediment, $V_d = \pi r^2 L_d$ is the desired volume of the sampling core based on the core radius (r) and the desired depth (L_d). F_p is the penetration force of the sampling core based on the load cell data, and s is the total distance traveled by the sampling core from the M_2 encoder. Based on the sets of $f_1(\mathbb{X})$ and $f_2(\mathbb{X})$ values, we can apply multiple objective optimization to identify the optimal pattern for a given sediment type, sample mass, etc. The optimal pattern is somewhat dependent on the chosen weights (w_1 and w_2) that reflect the user's emphasis on sample mass versus efficiency.

3.2 Preliminary Study - Experiment and Data Analysis

3.2.1 Experiment

For the experimental study, we used three sampling patterns and three sediment types to find the optimal sampling pattern for each type of sediment. We conducted independent experiments that varied the linear and rotational velocities for linear and helical sampling patterns and the frequency of the back and forth motion (direction of the rotation) for the zig-zag sampling pattern. We set $C_{max} = 3\ A$ as a value of the maximum current allowed to each motor. In addition, we applied the same compaction protocol to each sediment in every iteration to conduct experiment under the same condition.

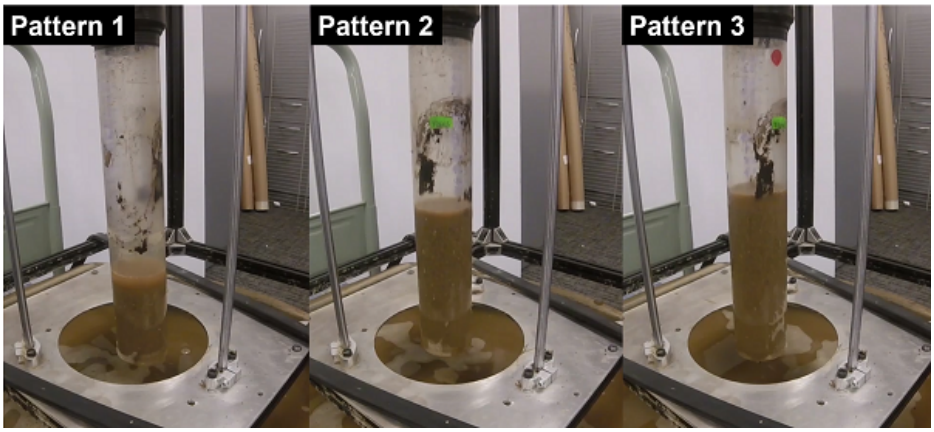

(a) Coarse sand

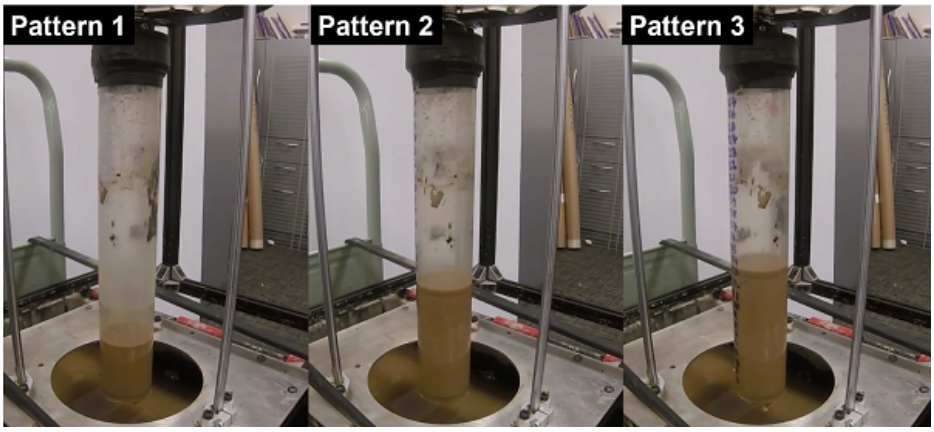

(b) Medium sand

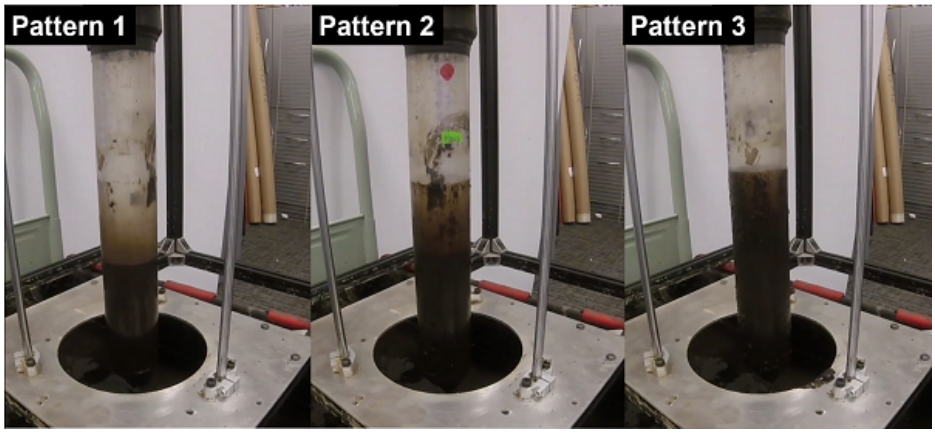

(c) Silt

Figure 3.5. Recovered sediment for each sediment sampling coring approach (i.e., pattern) and sediment type. Pattern 1 used a linear motion, Pattern 2 used a helical motion, and Pattern 3 used an oscillating zig-zag motion. Video recordings of the experiments are available at https://goo.gl/rhctu9.

Experiment Procedure

We utilized the two-step experiment: Step 1 – Apply two patterns P_1 (linear) and P_2 (helix); and Step 2 – Apply P_3 (zig-zag) based on the selected (statistically significant) patterns from the Step 1. We applied this procedure to all three sediment types. The recovered sediment from each experiment is shown in Fig. 3.5.

For Step 1, we applied 20 combination sets (4 patterns for P_1 and 16 patterns for P_2) of M_1 and M_2 inputs: $\nu_1 \in \{15, 22, 29, 38\}$ and $\omega_r \in \{0, 3, 6, 9, 12\}$. The sequence for each experimental combination was based on the Simple Random Sampling (SRS) [82] method to avoid bias. We ran three trials for each combination. For example, in the case of P_2 (helix motion), we could have 16 combinations, and for each combination, we repeated it three times. As a result, we had 48 sampling results of P_2 for each sediment. We collected four pieces of data: penetration depth, sampled sediment mass, penetration force, and motor current. We weighed sediment samples manually using a top load balance and other data were based on sensors.

For Step 2, we applied P_3 to validate the zig-zag motion. As shown in Eq. 3.3, the P_3 sampling core changes its rotating direction depending on the frequency of the motor input signal f_r, which is the direction change rate. Because we used the optimal angular velocity, ω_r, from our Step 1 results, we changed only the input frequency, $f_r \in \{0, 10, 30, 50\}$.

Statistical Approach

Based on Step 1 experimental results, $f_1(\mathbb{X})$ and $f_2(\mathbb{X})$ can be calculated as shown in Table 3.2. $f_1(\mathbb{X})$ and $f_2(\mathbb{X})$ are normalized values into the range [1, 10] (Table 3.2). First, we ran a two-way ANOVA to verify the significance of the results from two motors. Second, in order to select the patterns to use in the Step 2 experiment, we first found the patterns representing the minimum values in P_1 and P_2 (see bolded vales in Table 3.2). We then used a multiple comparison method [83] to find statistically significantly different patterns of these patterns, and we chose the results as the final patterns for the Step 2 experiment.

Step 2 experimental results based on the selected values from Step 1 experiment results are shown in Table 3.3: $f_1(\mathbb{X})$ and $f_2(\mathbb{X})$ values in Table 3.3 are normalized values into the

range [1, 10]. We also ran a two-way ANOVA to verify the significance of the selected patterns and the direction change rate. Based on Step 1 and Step 2 experimental results, we applied a weighted-sum multiple objective optimization to find the optimal pattern depending on the sediment type and weight configuration.

Experiment Result: Step 1

As we described in Section 3.3.4, $f_1(\mathbb{X})$ is a reciprocal function of the density of the sampled sediment based on the desired volume. $f_2(\mathbb{X})$ is a reciprocal function of the power of the sediment sampler, which indicates the sampling efficiency (the penetration force times the travel time to the desired depth). The lowest $f_1(\mathbb{X})$ indicates the largest amount of sediment sampled and the lowest $f_2(\mathbb{X})$ indicates the pattern with the highest work efficiency.

In the case of coarse sand, not all null hypotheses were rejected, based on results (Table 3.2(a)). The velocity of M_1 (ν_1(mm/s)) and the interaction between the velocities of M_1 and M_2 were significant (p-value < 0.05). The velocity of M_2 (ω_r(rad/s)) was not significant. To select the patterns of Step 2, the pattern with 38 mm/s of linear velocity and 12 rad/s of angular velocity (P_2: 38/12/0)[2] provided the minimum value of $f_1(\mathbb{X})$. The mass of sediment (257.67g) with this pattern was the largest amount recovered out of the 20 patterns. A value of 0 means no sample was collected, so we excluded these data from the optimization process.

In the case of medium sand, all null hypotheses were rejected based on the results (Table 3.2(b)). The velocities of M_1 and M_2, as well as the interaction between the velocities of M_1 and M_2, were significant (p-value < 0.05). The pattern with 29 mm/s of linear velocity and 12 rad/s of angular velocity (P_2: 29/12/0) provided the minimum $f_1(\mathbb{X})$ value. The mass of sediment (458.33g) from this pattern was the largest amount out of the 20 patterns.

In the case of silt, all null hypotheses were rejected based on the results (Table 3.2(c)). The velocities of M_1, M_2 and the interaction between the velocities of M_1, M_2 were significant (p-value < 0.05). The pattern with 15 mm/s of linear velocity and 12 rad/s of angular velocity (P_2: 15/12/0) provided the minimum value of $f_1(\mathbb{X})$. The mass of sediment (281g) with this pattern was the largest amount out of the 20 patterns.

[2]↑We use notation (P_x: $\nu_1/\omega_r/f_r$) where x is the pattern number, ν_1 is the linear velocity, ω_r is the angular velocity and f_r is the frequency.

Table 3.2. Experiment results of Step 1: P_1 and P_2 (a) Coarse sand, (b) Medium sand, and (c) Silt. The minimum values for each coring pattern and sediment type are highlighted in bold. The minimum $f_1(\mathbb{X})$ indicates the largest sampled mass and the minimum $f_2(\mathbb{X})$ is the best work efficiency.

(a) Coarse Sand

Objective	$f_1(\mathbb{X})$					$f_2(\mathbb{X})$				
Pattern	P_1	P_2				P_1	P_2			
ν_1(mm/s)ω_r(rad/s)	0	3	6	9	12	0	3	6	9	12
15	0.00	0.00	4.69	4.18	3.10	4.55	8.42	7.02	5.75	4.80
22	4.93	0.00	6.15	4.03	3.34	2.36	3.54	4.63	3.48	2.73
29	6.97	7.30	6.97	2.96	3.17	1.51	1.79	4.83	2.09	2.30
38	**4.67**	4.66	10.00	6.50	**2.63**	**1.11**	1.40	**1.35**	1.78	1.37

(b) Medium Sand

Objective	$f_1(\mathbb{X})$					$f_2(\mathbb{X})$				
Pattern	P_1	P_2				P_1	P_2			
ν_1(mm/s)ω_r(rad/s)	0	3	6	9	12	0	3	6	9	12
15	10.00	9.96	8.12	4.12	4.87	7.39	10.00	8.01	4.69	6.21
22	7.59	9.28	8.06	5.41	3.99	4.05	3.29	5.46	5.11	2.30
29	6.45	8.46	6.56	4.80	**1.41**	1.96	2.16	2.65	1.71	**1.00**
38	**6.30**	8.46	7.11	6.56	5.27	**1.12**	1.56	2.00	1.21	1.99

(c) Silt

Objective	$f_1(\mathbb{X})$					$f_2(\mathbb{X})$				
Pattern	P_1	P_2				P_1	P_2			
ν_1(mm/s)ω_r(rad/s)	0	3	6	9	12	0	3	6	9	12
15	7.51	10.00	3.07	2.82	**2.46**	5.61	4.90	7.08	8.21	9.39
22	4.66	3.80	3.07	2.58	2.95	2.22	3.85	4.70	4.62	3.11
29	**4.41**	4.41	3.55	3.43	2.82	**1.00**	2.70	2.48	3.49	2.25
38	5.20	5.62	4.04	4.04	3.92	1.08	**1.94**	2.25	2.53	2.54

Experiment Result: Step 2

The patterns were selected based on the multiple comparison method to test P_3 for each sediment. Multiple patterns are selected for coarse sand (7 patterns) and silt (14 patterns). In the case of medium sand, only one pattern was selected because results of the pattern with 29 mm/s of linear velocity and 12 rad/s of angular velocity (P_2: 29/12/0) were significantly different from the other patterns. Similar to Table 3.2, the lowest values for each pattern and sediment are in bold.

In the case of coarse sand (Table 3.3(a)), all null hypotheses were rejected. The velocities of M_1, M_2, and the interaction between the velocities of M_1 and M_2 were significant (p-value < 0.05). The pattern with 38 mm/s of linear velocity, 12 rad/s of angular velocity, and 30 Hz of the motor input frequency (P_3: 38/12/30) provided the minimum value of $f_1(\mathbb{X})$. The mass of sediment (486g) with this pattern was the largest amount out of the 28 patterns.

In the case of medium sand (Table 3.3(b)), all null hypotheses were rejected. The velocities of M_1 and M_2 were significant (p-value < 0.05). There was not much difference between the patterns in $f_1(\mathbb{X})$. The pattern with 29 mm/s of linear velocity, 12 rad/s of angular velocity, and 30Hz of the motor input frequency (P_3: 38/12/30) and P_3: 38/12/50 provided the minimum value of $f_1(\mathbb{X})$. The masses of sediment (493.67g and 491.33g) were respectively sampled in two patterns.

In the case of silt (Table 3.3(c)), all null hypotheses were rejected. The velocities of M_1, M_2 and the interaction between the velocities of M_1 and M_2 were significant (p-value < 0.05). The pattern with 15 mm/s of linear velocity, 6 rad/s of angular velocity, and 10Hz of the motor input frequency (P_3: 15/6/10) provided the minimum value of $f_1(\mathbb{X})$. The mass of sediment (306.33g) with this pattern was the largest amount out of the 56 patterns.

Summary of Experiment

To maximize the mass of the sampled sediment and the power efficiency of the sediment sampling platform, we minimized the values of $f_1(\mathbb{X})$ and $f_2(\mathbb{X})$, respectively. Three types of sediment were tested against three parameterized classes of core sampler motion under two different user objectives. While parameter variation was not exhaustive, we conclude from the data that it appears sufficient for the sediments explored and user objectives.

3.2.2 Data Analysis

Steps 1 and 2 measured four parameters: the mass of sampled sediment, penetration depth, penetration force, and motor currents. We analyzed the measured data to find the optimal values and characterize the sediments.

Table 3.3. Experiment result of Step 2: P_3 (a) Coarse sand, (b) Medium sand, and (c) Silt. The minimum values are highlighted in bold. The minimum $f_1(\mathbb{X})$ indicates the largest sampled mass and the minimum $f_2(\mathbb{X})$ is the best work efficiency.

(a) Coarse sand

Objective	$f_1(\mathbb{X})$				$f_2(\mathbb{X})$			
Pattern	P_2	P_3			P_2	P_3		
$\nu_1/\omega_r f_r$(Hz)	0	10	30	50	0	10	30	50
15/9	4.18	2.10	2.08	2.97	5.75	3.45	3.15	5.26
15/12	3.10	2.46	2.46	2.67	4.80	4.29	4.44	10.00
22/9	4.03	2.17	2.38	3.01	3.48	2.12	1.98	1.85
22/12	3.34	2.35	2.17	2.69	2.73	2.37	1.95	2.22
29/9	2.96	2.17	1.98	2.46	2.09	1.57	1.72	1.85
29/12	3.17	1.91	1.91	2.55	2.30	1.39	1.55	1.50
38/12	**2.63**	2.07	**1.87**	2.84	**1.37**	**1.00**	1.05	1.38

(b) Medium Sand

Objective	$f_1(\mathbb{X})$				$f_2(\mathbb{X})$			
Pattern	P_2	P_3			P_2	P_3		
$\nu_1/\omega_r f_r$(Hz)	0	10	30	50	0	10	30	50
29/12	**1.41**	1.07	**1.00**	**1.00**	**1.00**	**3.30**	3.39	3.73

(c) Silt

Objective	$f_1(\mathbb{X})$				$f_2(\mathbb{X})$			
Pattern	P_2	P_3			P_2	P_3		
$\nu_1/\omega_r f_r$(Hz)	0	10	30	50	0	10	30	50
15/6	3.07	**1.00**	2.58	2.46	7.08	7.97	7.68	5.53
15/9	2.82	3.31	3.31	4.41	8.21	6.24	7.03	5.67
15/12	**2.46**	5.01	5.38	6.35	9.39	6.07	6.98	10.00
22/3	3.80	4.41	5.38	5.01	3.85	2.87	2.73	2.34
22/6	3.07	2.58	3.68	3.19	4.70	5.07	3.90	3.08
22/9	2.58	5.50	6.59	7.32	4.62	4.74	5.60	5.13
22/12	2.95	5.14	5.86	5.14	3.11	3.98	4.46	3.83
29/3	4.41	3.31	2.58	2.70	2.70	2.04	1.85	1.75
29/6	3.55	4.04	4.28	5.38	2.48	2.78	2.52	2.13
29/9	3.43	2.58	4.65	4.53	3.49	2.64	2.98	2.58
29/12	2.82	1.73	2.70	3.19	2.25	3.57	3.94	2.99
38/6	4.04	4.53	6.23	5.26	**2.25**	1.93	1.81	**1.38**
38/9	4.04	3.92	4.89	5.01	2.53	1.79	1.95	1.70
38/12	3.92	5.14	6.11	5.38	2.54	2.06	1.89	1.72

Mass of Sampled Sediment

The mean and standard deviation of the mass of sampled sediment based on each pattern (Fig. 3.6) shows the variation of the mass sampled by the pattern. The blue bar indicates the average of the sampled mass with P_1, the red bar corresponds to P_2, and the green bar to P_3. In the case of coarse sand (Fig. 3.6(a)), the amount of sampled mass in P_2 increased by 61% as compared to that in P_1. The amount of sampled mass in P_3 increased by 355% and 178% as compared to that in P_1 and P_2, respectively.

In the case of medium sand (Fig. 3.6(b)), the amount of sampled mass in P_2 increased by 15% as compared to that in P_1. The amount of sampled mass in P_3 increased by 117% and 88% as compared to that in P_1 and P_2, respectively. In the case of silt (Fig. 3.6(c)), the amount sampled mass in P_2 increased by 8% as compared to that in P_1. The amount of sampled mass in P_3 increased by 5% as compared to that in P_1 but decreased by 2% as compared to that in P_2. Based on Fig. 3.6(a), Fig. 3.6(b), and Fig. 3.6(c), the sampled masses of coarse sand and medium sand increase as the pattern changes from P_1 to P_3 sequentially. In other words, a larger amount of coarse sand and medium sand was collected by P_3. In the case of silt, there was no significant difference between the patterns.

Multiple Objective Optimization

We posed the problem as a multiple objective optimization problem and defined the objective function using the weighted sum method from Section 3.3.4. The weighted sum method addressed the set of objectives as one single objective by multiplying each objective by a user-defined weight [84]. The feasible objective space was based on the $f_1(\mathbb{X})$ and $f_2(\mathbb{X})$ data sets for each sediment while solutions lie on a line called the *Pareto-optimal front* [85]. As shown in Fig. 3.7, the shaded area is the feasible objective space and the bold red line is the Pareto-optimal front.

Results of the multiple objective optimization via the weighted sum method are shown in Table 3.4 and Fig. 3.8. In the case of coarse sand (Table 3.4(a)), an optimal pattern is skewed despite the weight configuration. Pattern P_3: 38/12/30 is the optimal pattern when the user has equal concern for mass recovery and power expended (w_1=0.5, w_2=0.5), mass-

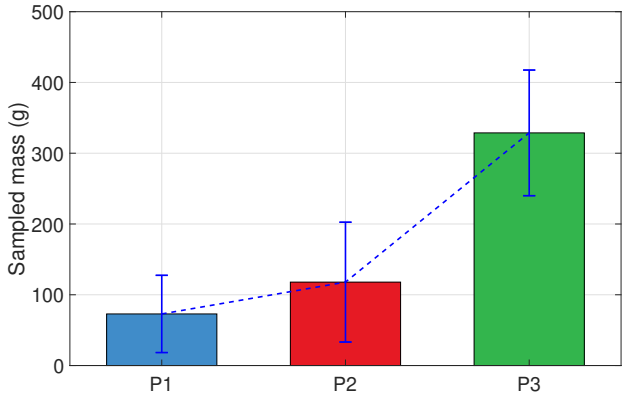

(a) Coarse Sand

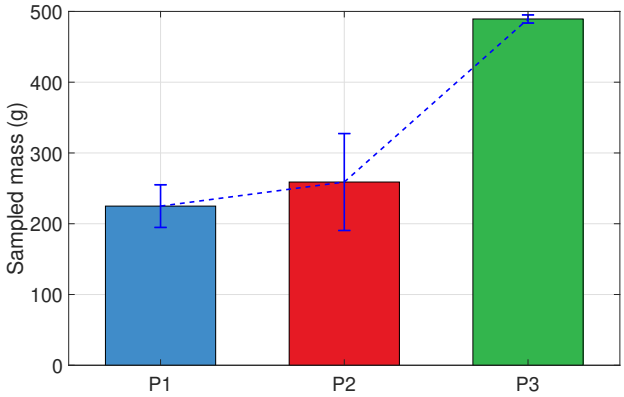

(b) Medium Sand

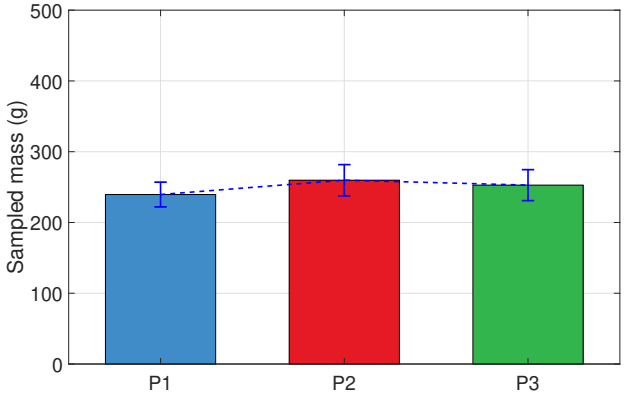

(c) Silt

Figure 3.6. Mean and standard deviation of each mass sampled by three patterns. The sampled masses of coarse sand and medium sand vary considerably with the pattern. No significant differences were observed as a function of coring patterns for silty sediment.

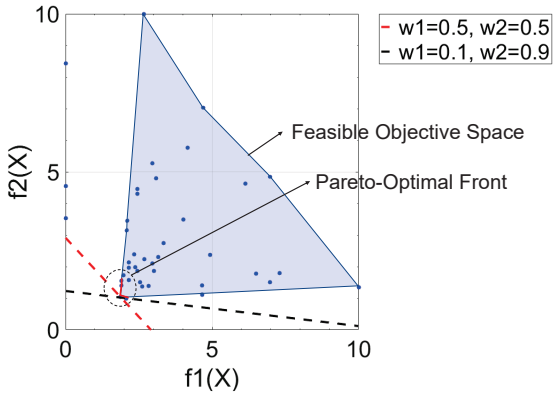

(a) Coarse sand

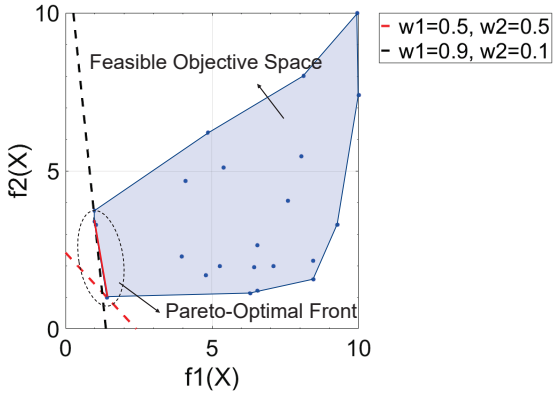

(b) Medium sand

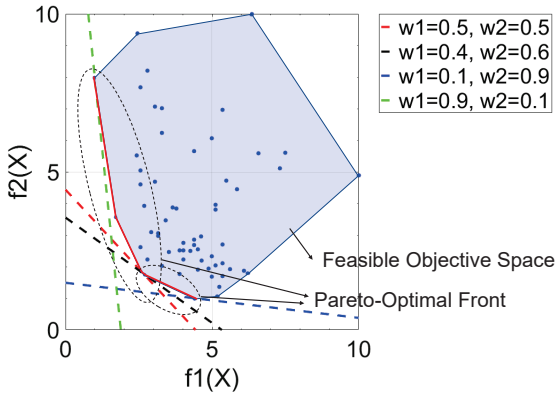

(c) Silt

Figure 3.7. Pareto-optimal front (red line) in the feasible objective space (shaded area) and the weighted objective functions (dotted line) of (a) Coarse sand, (b) Medium sand, (c) Silt. The coarse and medium sand have two optimal patterns, respectively. The silt has four optimal patterns.

Table 3.4. Results of the weighted sum method (a) Coarse sand, (b) Medium sand, (c) Silt.

(a) Coarse sand

Weight		Objective Function			Pattern			
w_1	w_2	$f_1(\mathbb{X})$	$f_2(\mathbb{X})$	$F(\mathbb{X})$	P	M_1	M_2	f_r
0.1	0.9	2.07	1.00	1.107	P_3	38	12	10
0.2	0.8	1.87	1.05	1.211	P_3	38	12	30
0.3	0.7	1.87	1.05	1.293	P_3	38	12	30
0.4	0.6	1.87	1.05	1.375	P_3	38	12	30
0.5	0.5	1.87	1.05	1.457	P_3	38	12	30
0.6	0.4	1.87	1.05	1.539	P_3	38	12	30
0.7	0.3	1.87	1.05	1.621	P_3	38	12	30
0.8	0.2	1.87	1.05	1.703	P_3	38	12	30
0.9	0.1	1.87	1.05	1.785	P_3	38	12	30

(b) Medium Sand

Weight		Objective Function			Pattern			
w_1	w_2	$f_1(\mathbb{X})$	$f_2(\mathbb{X})$	$F(\mathbb{X})$	P	M_1	M_2	f_r
0.1	0.9	1.41	1.00	1.041	P_2	29	12	0
0.2	0.8	1.41	1.00	1.082	P_2	29	12	0
0.3	0.7	1.41	1.00	1.123	P_2	29	12	0
0.4	0.6	1.41	1.00	1.164	P_2	29	12	0
0.5	0.5	1.41	1.00	1.205	P_2	29	12	0
0.6	0.4	1.41	1.00	1.246	P_2	29	12	0
0.7	0.3	1.41	1.00	1.287	P_2	29	12	0
0.8	0.2	1.41	1.00	1.328	P_2	29	12	0
0.9	0.1	1.00	3.39	1.239	P_3	29	12	30

(c) Silt

Weight		Objective Function			Pattern			
w_1	w_2	$f_1(\mathbb{X})$	$f_2(\mathbb{X})$	$F(\mathbb{X})$	P	M_1	M_2	f_r
0.1	0.9	4.41	1.00	1.341	P_1	29	0	0
0.2	0.8	4.41	1.00	1.682	P_1	29	0	0
0.3	0.7	4.41	1.00	2.023	P_1	29	0	0
0.4	0.6	2.70	1.75	2.132	P_3	29	3	50
0.5	0.5	2.58	1.85	2.217	P_3	29	3	30
0.6	0.4	2.58	1.85	2.290	P_3	29	3	30
0.7	0.3	1.73	3.57	2.282	P_3	29	12	10
0.8	0.2	1.73	3.57	2.098	P_3	29	12	10
0.9	0.1	1.00	7.97	1.697	P_3	15	6	10

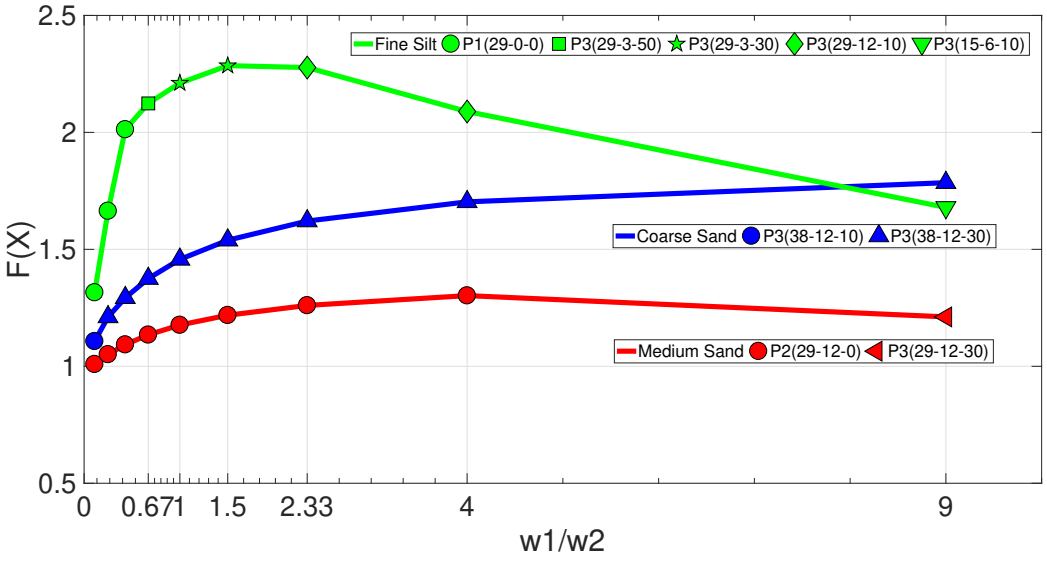

Figure 3.8. Diagram of the multiple objective optimization results where X-axis is the weight ratio between w_1 and w_2, and Y-axis is the sum of the $f_1(\mathbb{X})$ and $f_2(\mathbb{X})$ multiplied by each weight; $F(\mathbb{X}) = w_1 f_1(\mathbb{X}) + w_2 f_2(\mathbb{X})$. In the case of coarse sand (blue line) and medium sand (red line), an optimal pattern is skewed despite the weight configuration. In the case of silt (green line), the optimal pattern varies depending on the weight.

oriented sampling (when w_1=0.6 or higher / w_2=0.4 or less), or power-oriented sampling up to w_1=0.2, w_2=0.8. When the user is targeting a power-oriented sampling with w_2=0.9, pattern P_3: 38/12/10 is optimal.

In the case of medium sand (Table 3.4(b)), an optimal pattern is also skewed regardless of the weights placed on either mass or power. Pattern P_3: 29/12/30 is the optimal pattern when the user is targeting mass-oriented sampling with w_1=0.9. Pattern P_2: 29/12/0 is the optimal pattern when the user is targeting mass-oriented sampling up to w_1=0.8, w_2=0.2, balanced sampling (w_1=0.5, w_2=0.5), or power-oriented sampling (when w_1=0.4 or less / w_2=0.6 or higher).

In the case of silt (Table 3.4(c)), the optimal pattern varies depending on the weight. Pattern P_3: 15/6/10 is the optimal pattern when the user is targeting mass-oriented sampling with w_1=0.9. When the user is targeting mass-oriented sampling with w_1=0.8 and w_1=0.7, pattern P_3: 29/12/10 is the optimal pattern. When the user is targeting balanced

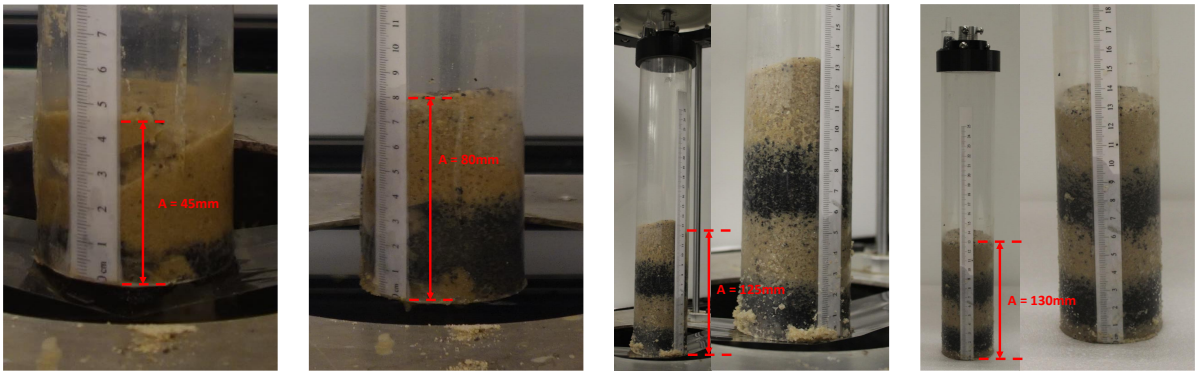

(a) (b) (c) (d)

Figure 3.9. Results of the sediment sampling disturbance experiments to validate the optimal sampling patterns for the quality of the sediment samples. We measured sediment disturbance via visual observation of the deformation of the layers of sediments and the total depth of sediment recovered (A: Core's length, and B = Penetration depth of 200mm); (a) P_1: Linear (A/B = 0.225), (b) P_2: Helix (A/B = 0.4), (c) P_3: Zig-zag (A/B = 0.625), and (d) Manual sampling by hammer coring (A/B = 0.65).

sampling (w_1=0.5, w_2=0.5) or mass-oriented sampling with w_1=0.6, pattern P_3: 29/3/30 is the optimal pattern. When the user is targeting power-oriented sampling with w_2=0.6, pattern P_3: 29/3/50 is the optimal pattern. When the user is targeting power-oriented sampling (when w_1=0.3 or less / w_2=0.7 or higher), pattern P_1: 29/0/0 is optimal.

Analysis on Sediment Disturbance

Minimizing the sediment disturbance in core sampling is a challenging problem. Unavoidable disturbances occur during the whole process of sampling: drilling, recovery, transportation, handling, and early stages of analysis [86]. Disturbances during the sampling process can cause disruption to the physical, geochemical, and biological condition of the sediment sample [86] [87] due to the various factors such as friction between the core liner and sediment, contamination by air exposure, and human error. Also, we realized that post-lab processes are necessary to measure parameters that can determine the disturbance of the sediment such as oxygen microprofiles, benthic oxygen flux rates, sediment solid phase analyses (chlorophyll a, organic carbon, and porosity), pore pressure, and secondary hydrate

formation [86] [87]. We tested our sampling platform to characterize the relative amount of disturbance using the three patterns for driving the core liner into the sediment. In addition, we conducted manual sampling (i.e., hammer coring) to compare its result with the platform-based sampling. We measured disturbance as the total depth of sediment recovered and via visual observation of sampled sediment.

For visual observation and analysis of sampled sediments, we used a coarse-grained sand layered with distinct red and tan colors (7 layers total and each layer was 30mm thick). Three optimal patterns (linear (P_1: 38/0/0), helix (P_3: 38/12/0), and zig-zag (P_3: 38/12/10)) that we found in Section 3.2.2 have applied. As shown in the figures, the *recovery ratio (A/B)*[3] was greatest with P_3: Zig-zag (A/B = 0.625, Fig. 3.9(c)), followed by P_2: Helix (A/B = 0.4, Fig. 3.9(b)) and P_1: Linear (A/B = 0.225, Fig. 3.9(a)), which was expected based on the previous experiment results in Section 3.2.1 and 2. Moreover, from the layered structure (the layer of tan and red sediment) of the sample taken with the three patterns based on the automated system and the manually sampled sample could not be concluded that there was a difference only by visual observation. For more precise analysis on the sediment disturbance, additional post-lab processing is required. We leave this for future work.

Summary of Data Analysis

Analysis of experimental results shows that the optimal pattern changed depending on the sediment pattern, sediment type, and user's objectives. In the case of coarse sand, pattern P_3 (zig-zag) performed best, regardless of objective preference, with greater linear (ν_1) and angular (ω_r) velocities improving both mass collection and power efficiency. The frequency of oscillation (f_r) did not strongly impact mass collection or power efficiency.

With medium sand, pattern P_2 (helical) is best unless mass collection is strongly preferred ($w_1 > 0.9$) over efficiency. In that case, P_3 is better. Using P_2, the faster angular velocity (ω_r) demonstrated better performance. However, the fastest linear velocity did not assure the best result. Using P_3 (mass collection preference), higher frequencies tended to improve mass collection, but not by much.

[3]↑Ratio A/B where "A" is the distance from the top of the sediment core to the bottom (core's length) and "B" is the penetration depth that we set as 200mm.

In the case of silt, pattern P_3 is best unless power efficiency is moderately preferred. In that case, pattern P_1 (linear) is better. The interaction between $f_1(\mathbb{X})$ and $f_2(\mathbb{X})$ was not strong, however.

3.2.3 Summary

To understand sediment sampling, we developed and tested a robotic sampling platform in the laboratory to test functionality under a range of sediment types and operating conditions. Specifically, we focused on three patterns by which a cylindrical coring device was driven into the sediment (linear, helical, and zig-zag) for three sediment types (coarse sand, medium sand, and silt). The results show that the optimal sampling pattern varies depending on the type of sediment and can be optimized based on the sampling objective. We examined two sampling objectives: maximizing the mass of minimally disturbed sediment and minimizing the power per mass of sample. This preliminary study provides valuable data to aid in the selection of optimal sediment coring methods for various applications and builds a solid foundation for future field testing under a range of environmental conditions.

4. UNCREWED SEDIMENT SAMPLING SYSTEM

This chapter contains the material from the previously published papers. The material has been added with the consent of the all the authors on the papers.

- J. H. Bae, J. H. Park, S. Lee, and B.-C. Min, "Tri-SedimentBot: An underwater sediment sampling robot," *2016 IEEE International Conference on Automation Science and Engineering (CASE)*, August, 2016.

- J. H. Bae, S. Luo, S. S. Kannan, Y. Singh, B. Lee, R. M. Voyles, M. Postigo-Malaga, E. G. Zenteno, L. P. Aguilar, and B.-C. Min, "Development of an Unmanned Surface Vehicle for Remote Sediment Sampling with a Van Veen Grab Sampler," *2019 MTS/IEEE OCEANS*, Seattle, WA, USA, 27-31 October, 2019.

The main objective of this research is to design an unmanned system that can collect sediment samples from the desired sampling area. In this section, we aim to describe the overall idea of an uncrewed sediment sampling system, system requirements, and system design of unmanned platforms (USV and USS) that compose this system.

4.1 Overall Idea

The uncrewed sediment sampling system has two main functions: 1) navigate toward the desired sampling location relative to the body of water, and 2) sample the sediment while maintaining position relative to the body of water. To achieve these functions, we propose a unique multi-robot team consisting of an unmanned surface vehicle (USV) that carries an underwater sediment sampler (USS). Each system has two missions in their respective workspaces, as shown in Fig. 4.1. The mission hierarchy prioritizes USV missions over USS missions in the following order: *Deploying* $\rightarrow$ *Positioning* $\rightarrow$ *Launching* $\rightarrow$ *Sampling*.

Given the workspace, each unmanned system must complete its missions to attain the goal of an uncrewed sediment sampling system. The USV performs its missions on the water surface, and the first mission is to deploy to the desired sampling point (*Deploying* state). Once the USV arrives at the sampling point, it must maintain its position within the maneuvering range by anchoring (*Positioning* state).

Following the completion of the USV positioning, the system must transfer to the *Launching* state, and the USS performs its missions in the underwater environment as illustrated in Fig. 4.2. The launching state can be divided into two sub-missions, namely submerging and landing. The USS is a tethered system where the winch on the USV must launch the USS. Once the USS touches the bottom of the water, it must satisfy the stability limit based on the orientation of the USS to move to the *Sampling* state. During this state, the coring tube of the USS needs to penetrate the sediment bed to collect the sediment sample. Once all states are completed, the system reverses the mission procedure and return the USV to the base station with the sediment sample as depicted in Fig. 4.2.

To complete all missions, a communication system is required to be established between the unmanned systems (USV and USS) and the base station for monitoring and controlling purposes. Environmental disturbances such as wind, current, uneven terrain, and obstacles

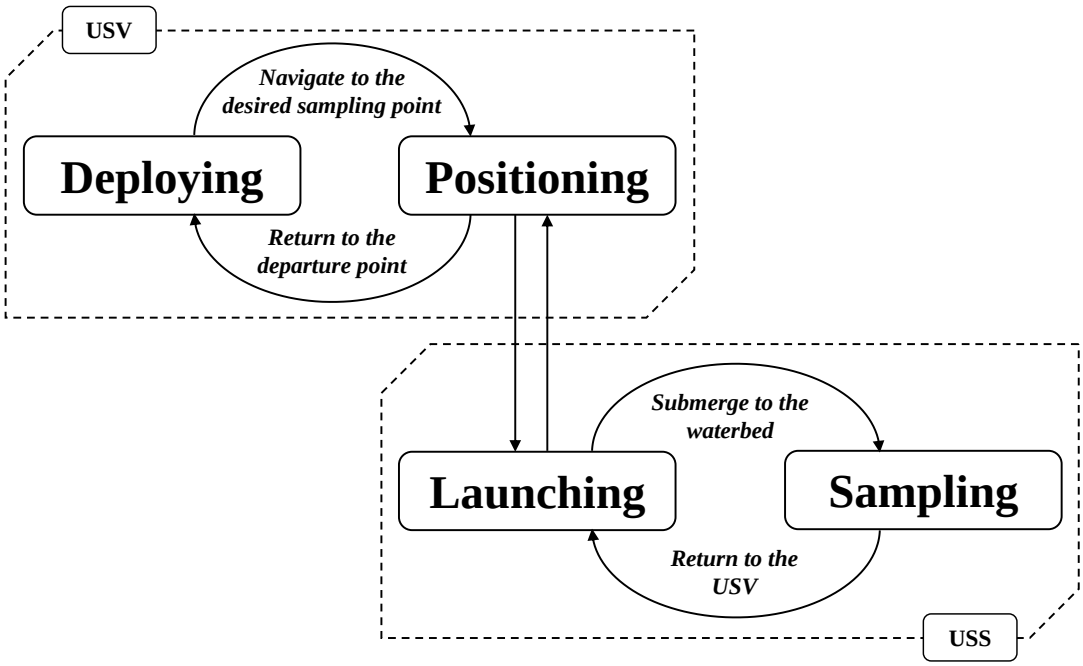

Figure 4.1. State diagram of uncrewed sediment sampling system showing missions of each unmanned system. The mission hierarchy prioritizes USV missions over USS missions.

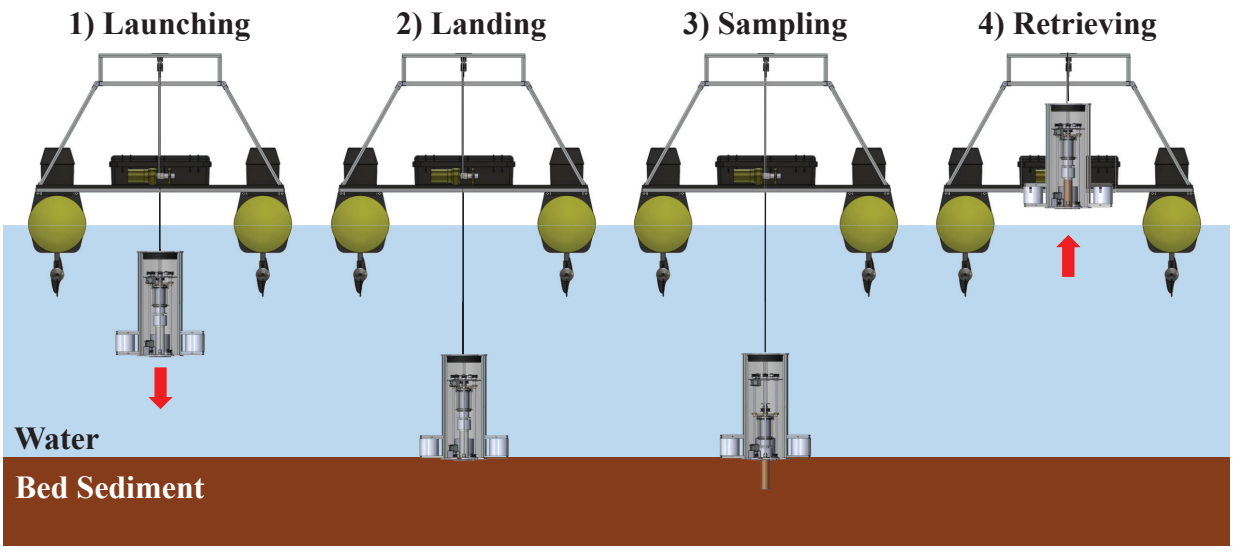

Figure 4.2. A procedure of sediment sampling: 1) Submerge the USS to the bottom of the water, 2) Once the USS lands at the bottom, 3) The coring tube of the USS starts sampling the sediment, 4) when sampling is done, the USV starts to retrieve the USS with the sediment sample.

must also be considered during the development of this system to establish an effective unmanned system.

4.2 System Design of the USV

We adopt a catamaran structure based on twin hulls that can reduce roll and pitch motions to maintain the stability of the USV. The overall dimensions and specifications of the USV are shown in Fig. 4.3(a) and Table 4.1.

The USV for the uncrewed sediment sampling system is designed based on three system requirements: *Deploying*, *Positioning*, and *Launching*. Based on the system requirements for the USV, we can divide it into four sub-systems: propulsion system, positioning system, launching system, and monitoring system as shown in Fig. 4.3(b). The propulsion system uses two thrusters to deploy the USV to the desired sampling point. The positioning system is based on a double anchoring method to maintain the position of the USV within the maneuvering range, while the launching system employs the winch to launch the USS to the

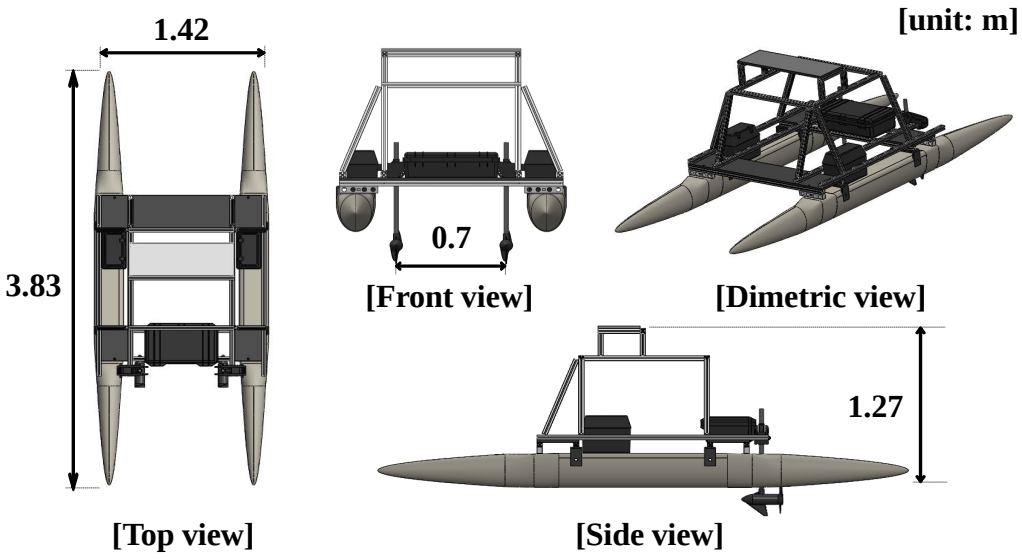

(a)

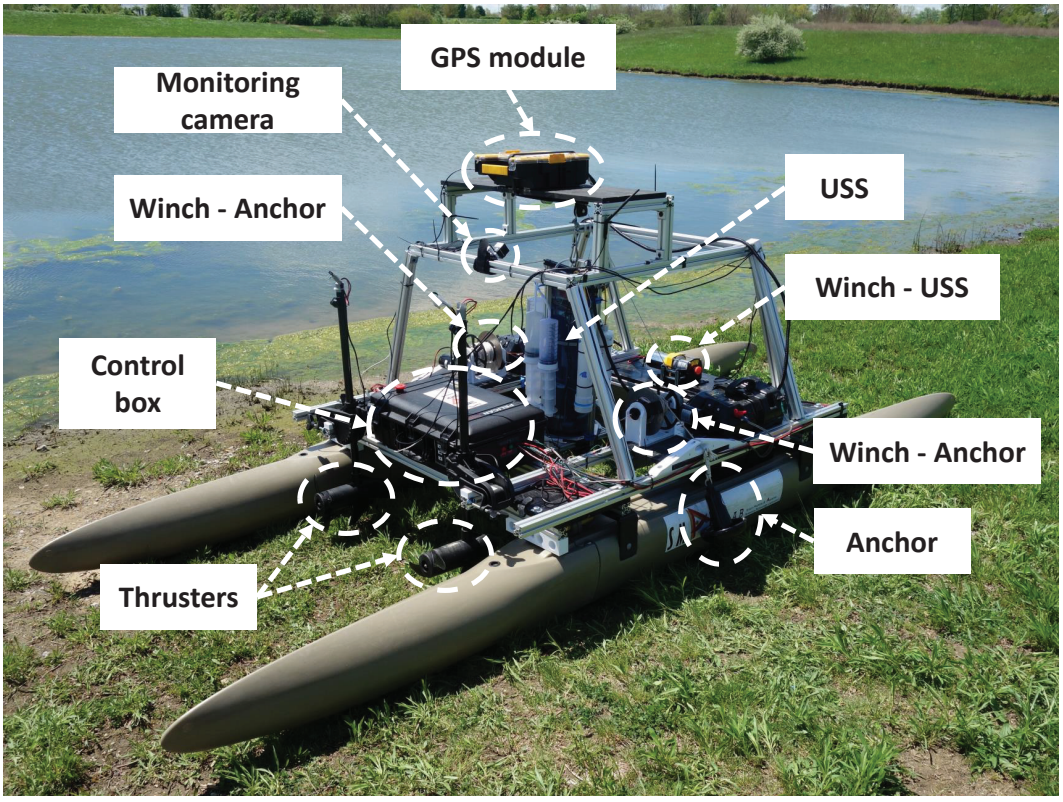

(b)

Figure 4.3. (a) Overall dimensions for the USV, and (b) Full set up of the USV.

Table 4.1. Hardware specification of the USV.

Parameter	Value (m)
Length (overall)	3.83
Width (overall)	1.42
Height (overall)	1.27
Diameter of hulls	0.324
Draft	0.19
Distance between propellers	1.12

bottom of the water. The monitoring system is for controlling the positioning and launching systems based on the online streaming of the view of winches for those systems on the USV.

4.2.1 Deploying

The main mission of the USV in the *Deploying* state is to carry the USS to the desired sampling area. The USV must deploy from the base station to the desired sampling area. To deploy the USV to the sampling area, a propulsion system is required. The propulsion system consists of two thrusters from each side of the USV, port (left) and starboard (right) side. Based on this configuration, we can define the velocity of each thruster as n_p (port (left) side thruster velocity) and n_s (starboard (right) side thruster velocity). Thrusters are 12V freshwater trolling motors that are controlled by the motor controller unit (MCU) to implement maneuverability for the USV. Thus, the USV possesses a differential steering mechanism based on two inputs to control the velocity and heading. We represent the thruster velocities as a common mode (n_c) and differential mode (n_d) can be defined [88], [89] as $n_c = \frac{n_p+n_s}{2}$, $n_d = \frac{n_p-n_s}{2}$. Ideally, the differential thrust is zero when the USV maneuvers straight by operating two propellers at the same speed. To change the heading of the USV, two propellers (port and starboard side) are required to generate momentum by the differential thrusts. However, the velocity also shifts while changing the heading of the USV. Thus, coupling moment between the velocity and yaw rate of the USV occurs.

4.2.2 Positioning

Maintaining of the position of the USV is necessary when the system transfers from the *Positioning* state to the *Launching* state. We adopt a double anchoring method to minimize the maneuvering of the USV. The cable length of each anchor ($L_{A,p}$ and $L_{A,s}$) must be longer than the depth of the water (h_w). We consider the wind as a significant factor during the *Positioning* state. The USV will be dragged by the wind to the arbitrary point at the boundary of the maneuvering range depending on the direction of the wind. The USV can minimize the maneuvering unless there is a significant change of wind direction. When the USV settles at the arbitrary point, the tension on the cable of the anchor is observed to hold the position of the USV, which can be defined as $T_A = m_A g \sin^{-1}\theta_A$, where $m_A g$ is the weight of the anchor and θ_A is the angle between the cable and the water surface. We assume that the horizontal force of the tension ($T_A \cos\theta_A$) is greater than the drag force acting on the USV based on the wind ($F_{drag,wind}$), which allows us to maintain the position of the USV within the boundary of the maneuvering range, where $T_A \cos\theta_A = m_A g \tan^{-1}\theta_A$, $F_{drag,wind} = \frac{1}{2}\rho_{wind} v_{rel}^2 C_d A_{USV}$, ρ_{wind} is the density of the wind, v_{rel} is the speed of the USV relative to the wind, C_d is the drag coefficient, and A_{USV} is the cross-sectional area of the USV.

The main purpose of the positioning system is to minimize the maneuvering range of the USV. The positioning system consists of two customized winches, anchors (5 kg), and the MCU. The anchoring winch has a clutch consisting of electromagnets to integrate a free-fall function by engaging and disengaging the spool of the winch as shown in Fig. 4.4. The steel plate is fixed to the spool, and the electromagnets disengage from the steel plate to ensure that the anchor free-falls by its weight. Electromagnets engage the steel plate to rewind and retrieve the anchor by coupling the spool with the motor. The axial force ($F_{em,axial}$) of the electromagnets is approximately 185 N. Based on the coefficient of friction ($\mu_{em} = approximately 0.5$) between the metal part of the electromagnets and the steel plate, the shear force ($F_{em,shear}$) to break the axial force can be calculated as $F_{em,shear} = \mu_{em} F_{em,axial} = 0.5(185) = 92.5\ N$. Since two electromagnets are installed, the total shear force is $185N$. The

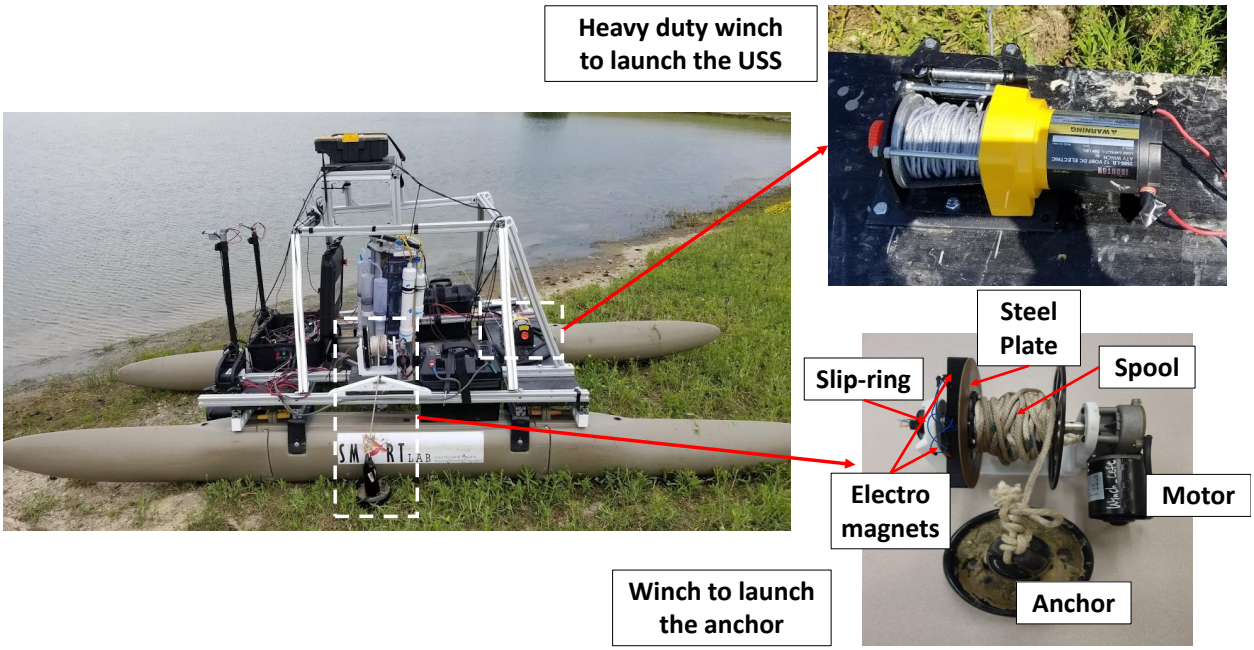

Figure 4.4. Figure on the top right shows the heavy-duty winch to launch the USS. A bottom right figure shows the customize winch for anchoring. The spool of this winch consists of still plate, electromagnets, and slip-ring. When the electromagnet is detached, the spool can rotate freely. When the electromagnet is engaged with the steel plate, we can rotate the spool with the motor.

maximum load of the anchor winch can be approximated to 18.9 kg, and the cable feeding rate of the anchoring winch is approximately 6.3 m/min.

4.2.3 Launching

The launching system of the USV intends to launch the USS to the bottom of the water. We use a heavy-duty winch since the load of the USS (40 kg or more) is much heavier compared to the anchors (approximately 5 kg), as shown in Fig. 4.4. The user can achieve the remote operation of the USS launching through real-time monitoring from the base station.

4.3 System Design of the USS

The two missions of the USS are *Launching* and *Sampling*. Based on missions of the USS, we can define the system requirements for designing the underwater platform as: *Launching*, *Sampling*, and *Pressure Equalizing*.

The USS is a tethered system based on the launching system on the USV. To deploy the USS to the bottom of the water, it must be designed as a submersible and stable platform. However, the waterproofing of the USS is a challenging process, and equalizing the pressure between the inside of the USS and the water is critical. The pressure equalization system, shown in Fig. 4.5(a), is complex and described later in this dissertation. To complete the sampling mission, a penetrating function based on the core sampling method is necessary. Moreover, implementing sampling patterns to support penetration is also critical as shown in Fig. 4.5(b). After penetration, functions to capture the sediment and to prevent sample loss must be considered prior to collection of the sediment sample.

4.3.1 Launching

In the *Launching* state of the USS, the USS submerges using negative buoyancy force to the bottom of the water since the total weight (W_{USS}) of the USS is greater than the buoyancy force ($F_{b,USS}$) acting on the USS. The first condition to launch the USS can be defined as $W_{USS} > F_{b,USS}$, where $W_{USS} = M_{USS}g = (m_s + 4m_l)g$ is the total weight of the USS, M_{USS} is the total mass of the USS, m_s is the mass of the main body of the USS, and m_l is the mass that attached to each landing gear. The buoyancy force ($F_{b,USS} = -\rho_w g V_{USS}$) is based on the density of the water (ρ_w) and the fluid volume that displaced by the USS (V_{USS}) as shown in Fig. 4.6.

The weight of the core (including the encloser) of the USS is almost equalized with the buoyancy force of the USS. According to this result, external mass is necessary to increase the downward force (negative buoyancy) of the USS. We installed a total of 20 kg (or more) of external mass and distributed to each landing gear of the USS. Based on the submersible design, the USS is able to submerge itself by its weight. However, the USS is a tethered system, which helps in the prevention of collision with the bed sediment. We launch and

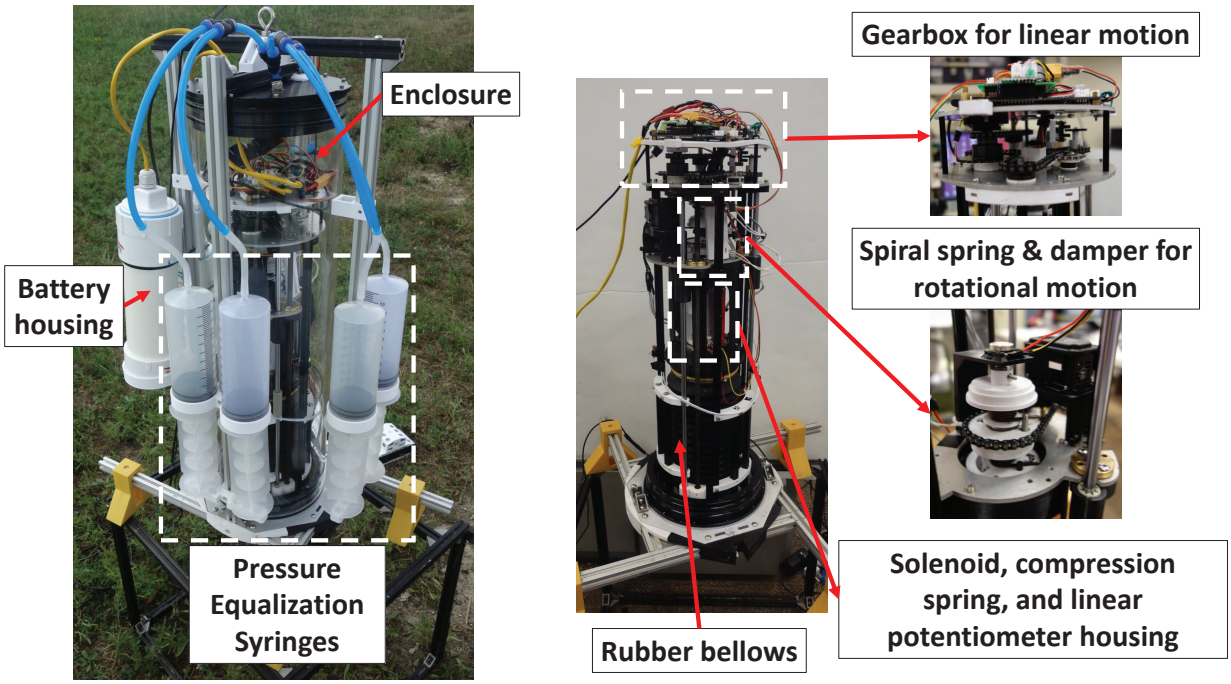

(a) (b)

Figure 4.5. (a) Assembled main system of the USS showing the enclosure, battery housing, and pressure equalization system (syringes), and (b) Detailed components of the USS in charge of generating different motions (linear motion, rotational motion, and hammering motion) and sensing the penetration process using the linear potentiometer.

retrieve the USS with the launching system of the USV. Since the USS is tethered, it has two connections with the USV: physical cable and serial communication cable. The length of the physical cable (L_S) must be longer than the height difference between the depth of the water and the height of the USS ($h_w - h_s$). The second condition of the *Launching* state can be defined as $L_S > h_w - h_s$ as shown in Fig. 4.6.

A stable design of the USS is essential to land on the sediment bed successfully, and to maintain the position and orientation of the USS during the sampling process. The external weight attached to the USS is not only for submerging but also to increase the stability of the USS. The mass is not distributed throughout the USS to concentrate the mass at the bottom of the USS. This design lowers the center of gravity (CG) as low as possible to increase the distance between the center of buoyancy (CB). Moreover, by lowering

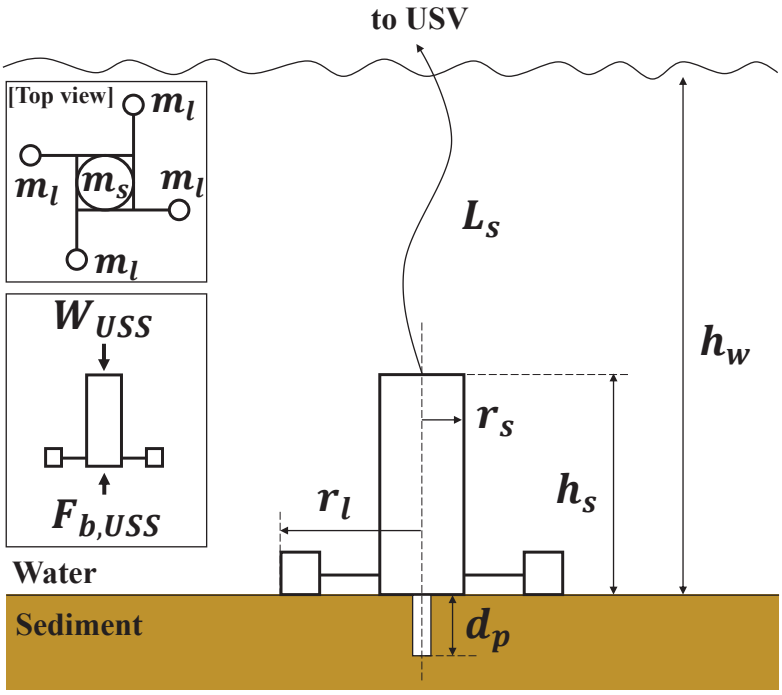

Figure 4.6. Conditions of the USS during the *Launching* state where m_s is the mass of the main body of the USS, m_l is the mass that attached to each landing gear, $F_{b,USS}$ is buoyancy force, W_{USS} is the weight of the USS, r_s is the radius of the body of the USS, r_s is the radius of the bottom of the USS, d_p is the penetration depth, L_s is the cable length attach to the USS, and h_w is the depth of the water.

the position of the CG, we can increase the toppling limit the USS can be calculated as $\angle BAB = \theta_{tl} = \frac{\pi}{2} - \arctan\left(\frac{\overline{oP_{CG}}}{\overline{oA}}\right) = 46.56°$, where $\overline{oP_{CG}}$ is the distance between the position of the CG and the center of the USS bottom, and $\overline{oA}$ is the distance between the center of the USS bottom and the tip of the USS leg as shown in Fig. 4.7.

The orientation of the USS can be measured by the IMU (Inertial Measurement Unit) sensor. When the USS lands on the sediment bed, roll and pitch angle of the USS must be smaller than the toppling limit to complete the sampling mission successfully, $\phi_{USS}, \theta_{USS} < \theta_{tl} = 46.56°$, where ϕ_{USS} is the roll angle of the USS and θ_{USS} is the pitch angle of the USS. If the roll or the pitch angle is greater than the toppling limit, the USS will tip over.

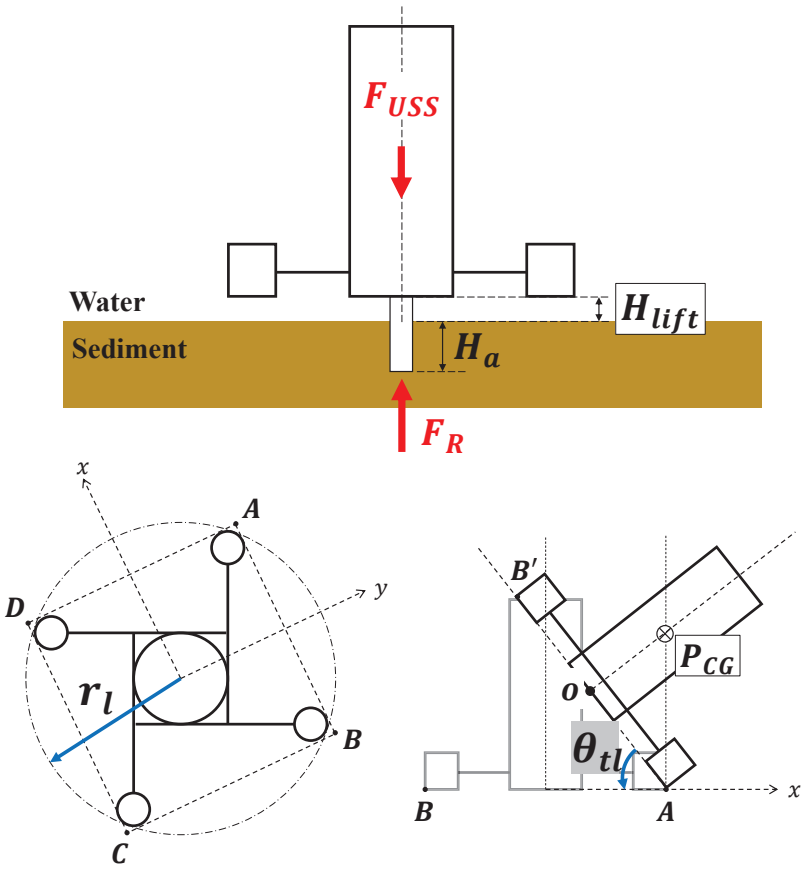

Figure 4.7. Top figure: Lifting condition of the USS, H_a is the actual penetration depth, and (H_{lift} is the height of the lift, Bottom figure: Toppling limit of the USS, r_l is the radius of the bottom of the USS, P_{CG} is the center of gravity of the USS, and θ_{tl} is the angle of the toppling limit.

Pressure Equalizing

The rubber bellows around the coring tube is sealed to ensure that the air gets trapped in the bellows at the surface. As the USS descends, the pressure changes, compressing the volume of air. The volume of air of the enclosure changes since the coring tube is deployed vertically, compressing the large rubber bellows and displacing some of the air. Furthermore, the external pressure changes as the USS descends to the sampling depth. Equalizing the internal and external pressure is necessary to maintain the vertical motion of the coring tube. The shape of the large rubber bellow must be maintained to keep the vertical motion by equalizing the pressure between the inside and outside of the USS.

We can describe the volume change due to the linear motion by calculating the volume difference between the initial volume of the large rubber bellow and the volume of the bellow when the coring tube is fully deployed, $\Delta V_{L-bellow} = V_{L-\text{bellow,i}} - V_{L-bellow,f} = 4.8 \times 10^{-4} m^3$. The volume change due to the increase of the external pressure can be calculated based on the density of the air at atmospheric pressure and pressure with the depth of water. We assume that temperature is the standard temperature, the maximum depth of water is $3m$, and the mass of the air is constant. Based on the assumptions, we can calculate pressure, temperature, and density at water depth at 3 m as shown in Table 4.2.

Table 4.2. Properties of the standard atmosphere and water depth.

	Standard Atmosphere	Water Depth (@ $3m$)
Pressure (p)	101.325 kPa	130.655 kPa
Temperature (T)	15 °C (288.15 K)	15 °C (288.15 K)
Density (ρ)	1.225 kg/m^3	1.576 kg/m^3

The air volume inside of the USS at atmosphere pressure is $V_{air,atm} =$ and the mass of the air inside of the enclosure is $m_{air} = \rho_{air,atm} V_{air,atm} = (1.225)(0.019) = 0.024kg$, and the air volume at pressure due to the water depth of $3m$ is $V_{air,3m} = \frac{m_{air}}{\rho_{air,3m}} = (0.024)/(1.576) = 0.015m^3$.

The volume difference due to pressure change is $\Delta V_{pressure} = V_{air,atm} - V_{air,3m} = 0.019 - 0.015 = 0.004m^3$, so the total volume change can be calculated as $\Delta V_{total} = \Delta V_{L-bellow} + \Delta V_{pressure} = 4.8 \times 10^{-4} + 0.004 = 4.48 \times 10^{-3} m^3$.

To compensate for the total volume difference, an extra volume must be connected to the inside of the USS. We installed four large syringes connected to the inner volume of the USS. Pistons of syringes were initially fully extended to create an extra volume, which will ascend when the USS deploys to the underwater and the coring tube starts the sampling mission. Pistons will descend when the USS returns to the atmospheric pressure and the coring tube is back to the initial position.

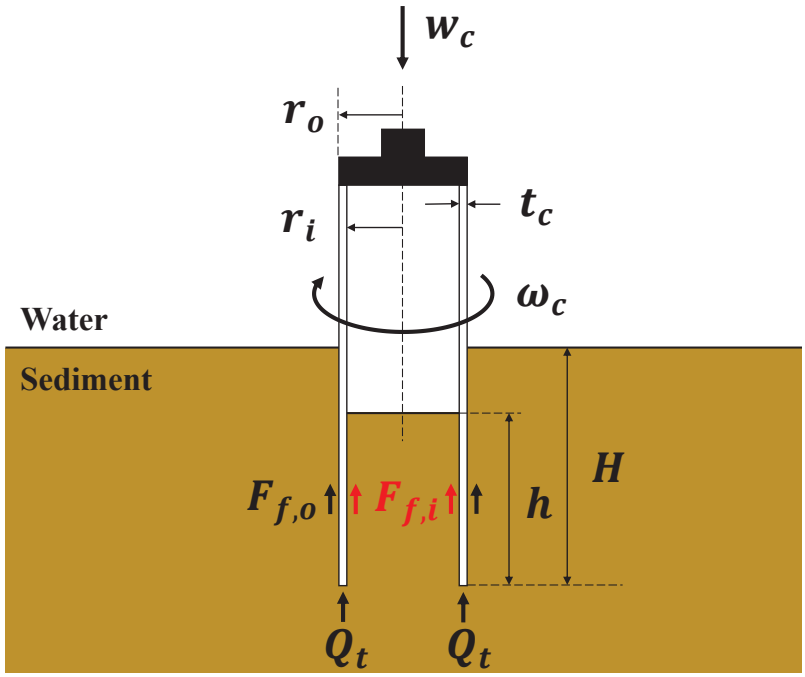

Figure 4.8. Input variables for sampling patterns; w_c is the linear velocity, and ω_c is the angular velocity, Q_t is the bearing capacity at the tip, $F_{f,\mathrm{i}}$ and $F_{f,o}$is the friction between inside and outside wall of the coring tube, penetration depth (H), core depth (h), thickness of the core (t_c), and inner and outer radius of the coring tube (r_i, ro).

4.3.2 Sampling

At the *Sampling* state, we adopt a core sampling method to sample the sediment. When core sampling, the penetration depth ($d_p = H$) cannot be considered as the actual coring depth. The actual coring depth (h) is smaller than the penetration depth and the recovery ratio (h/H) can be used as one of the sampling evaluation categories as shown in Fig. 4.8.

During the sampling process, the reaction force acting on the coring tube of the USS due to the penetration affects the performance of the USS. Forces acting on the coring tube and parameters of the coring tube can be simplified, and the penetration force can be driven as $F_p = F_\mathrm{e} + W_b - Q_t - F_f$, where F_p is the penetration force, F_e is the external driven force, W_b is the buoyant weight of the sampler, Q_t is the bearing capacity at the tip of the core, and F_f is the side friction [90] between the wall of the core and sediment. To penetrate the

sediment, the sum of the external force and weight of the core ($F_e + W_b$) must be greater than the reaction force ($Q_t + F_t$), $F_e + W_b > Q_t + F_f$ as shown in Fig. 4.8.

If the reaction force ($F_R = Q_t + F_f$) is greater than the net force ($W_{USS} - F_{b,USS}$) acting on the USS, it can break the position and orientation of the USS. The USS can collapse when the roll or pitch angle of the USS is greater than the toppling limit. For example, if the USS is pivoting by $\overline{AB}$, the USS will collapse when the center of gravity (CG) passes the pivoting line ($\overline{AB}$). Based on the position of the CG, the toppling limit of the USS can be defined as $\angle BAB = \theta_{tl}$. Also, the USS can be lifted by the reaction force as shown in Fig. 4.7.

Sampling Pattern

We adopt a zig-zag motion from a preliminary study to penetrate the sediment. The zig-zag motion is the combination of the linear and rotational motion. During the penetration process, the coring tube is a 2-DOF condition: *heave and yaw*. We can define a more simplified kinematics equation for the coring tube since the vector of the body position is $\eta_1 = (z)^\top$, and the vector of the body Euler angle is $\eta_2 = (\psi)^\top$. Also, the translation motion and rotational motion only occurs along the z-axis ($\nu_1 = (w)^\top, \nu_2 = (r)^\top$).

The actual translation and rotational motion of the coring tube based on two servo motors can be illustrated as shown in Fig. 4.9(a). The position (z_c) and linear velocity (w_c) of the lead screw as shown below:

$$z_c = r_m tan\lambda \theta_{lead} \tag{4.1}$$

$$w_c = \frac{r_m}{cos\lambda}\dot{\theta}_{lead} \tag{4.2}$$

where r_m is the radius of the lead screw, λ is the lead angle, and θ_{lead} is the lead screw rotation. The angular velocity of the coring tube (ω_c) can be expressed as shown below:

$$\omega_c = \frac{\Delta\theta_c}{\Delta t} \tag{4.3}$$

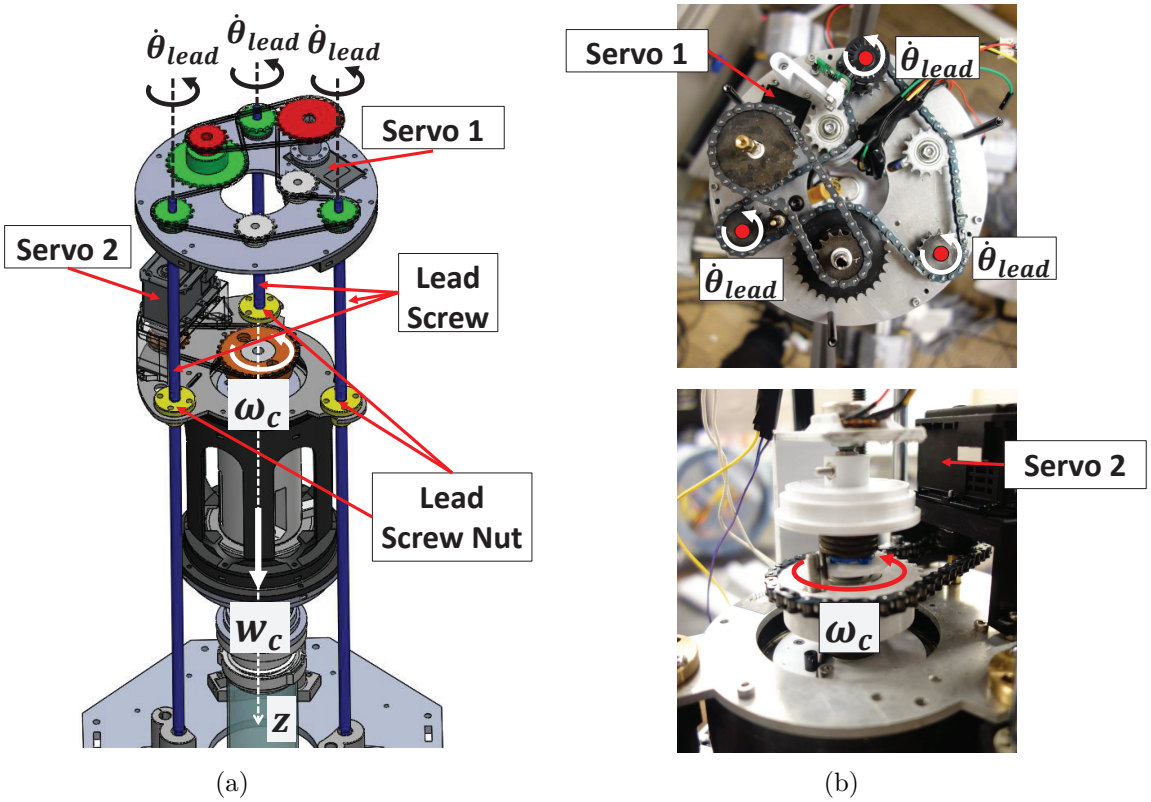

(a) (b)

Figure 4.9. (a) Linear and rotational motion of the coring tube. Blue shafts are lead screws and yellow nuts are lead screw nuts. Red and green gears are to generate linear motion, and orange gears are to generate rotational motion, $\dot{\theta}_{lead}$ is the angular velocity of lead screws, and linear velocity (w_c) and angular velocity (ω_c) of the coring tube, (b) Integrated linear and rotational motion system.

where $\Delta\theta_c$ is change in angular rotation of the coring tube and Δt is the time difference.

To generate the linear motion, we installed three lead screws to convert the rotational motion from the servo (servo 1 - linear servo) as shown in Fig. 4.9(a). We designed the gearbox to convert linear motion to rotational motion and to increase the feed rate of the coring tube. Another servo (servo 2 - rotary servo) is installed in the coring tube module to generate the rotational motion as shown in Fig. 4.9(a). We integrated the solenoid to generate the hammering motion. The main purpose of the hammering motion is to support penetrating the sediment as shown in Fig. 4.10.

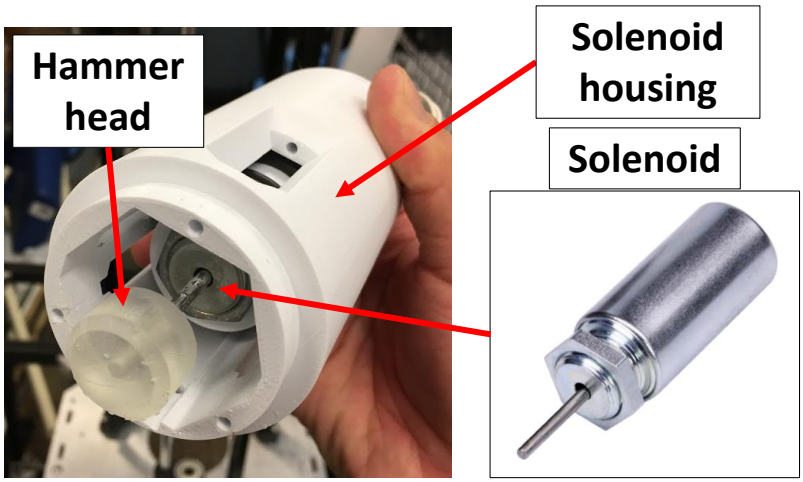

Figure 4.10. Solenoid with hammering head installed in the housing.

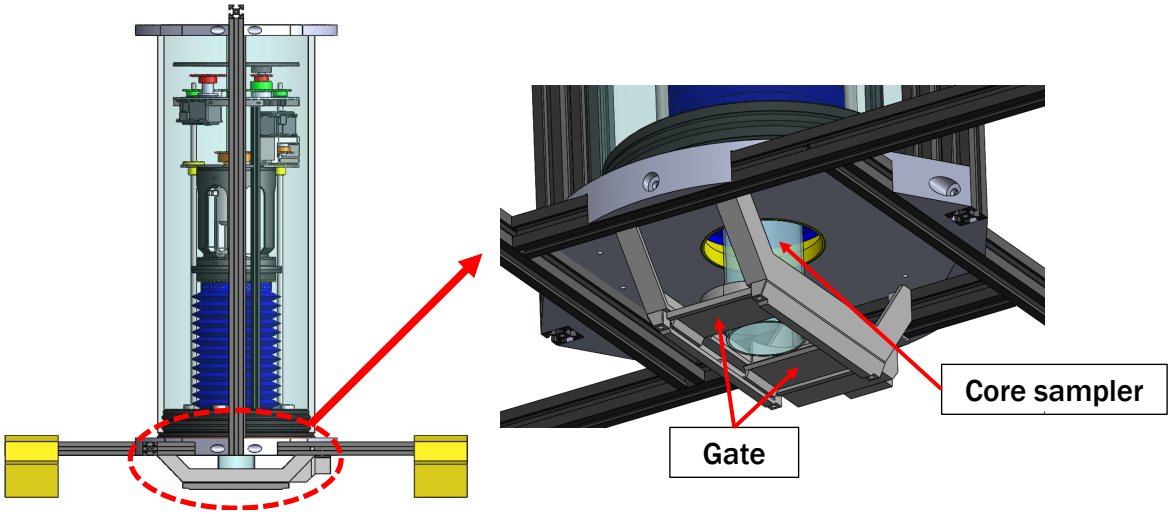

Figure 4.11. Gate system of the USS to block the bottom of the coring tube.

Sediment Sample Securement

After the penetration, capturing the sediment inside of the coring tube is essential to securing the sediment. We designed and installed an automatic gate that seals the open end of the coring tube at the completion of the coring cycle. This double-gate entrapment, shown in Fig. 4.11, closes from both sides to prevent sediment loss and movement, thereby preserving sediment quality by helping to reduce sediment disturbances. The gate is a passive system based on the position of the coring tube. The location of the gate aligns with the tip

of the coring tube when it is fully retracted to the initial position and the gate opens from the middle. It must be opened to penetrate the sediment, to ensure that the starting point of the coring tube is only a few centimeters below the initial position. To close the gate, the coring tube must retract to the initial position.

4.3.3 Sediment Sampling Pattern Analysis

The USS has three different motions: Linear motion, Rotational motion (direction changing), and Hammering motion. Based on these motions, we can generate three sampling patterns; 1) Linear, 2) Linear+Rotational (direction changing), and 3) Linear+Rotational (direction changing)+Hammering. We can generate several sampling patterns depending on the input variables of each motion. The main objective of sampling pattern analysis is to find the optimal sampling pattern by analyzing the reaction force, as well as input and output energy. We compare the reaction forces of sampling patterns to explain effect of different motions on the reaction forces. Additionally, the reaction forces are a critical factor to determine whether the USS can maintain its stability. The input energy is based on input variables to generate motions and we can consider the reaction forces to calculate the output energy. We can derive the energy efficiency of the system during sampling based on input and output energy.

Reaction Force

The reaction force is generated when the sampling core penetrates the sediment. Also, the reaction force consists of two types of forces as we defined in Section III.B.4) which are the bearing capacity (Q_t) acting on the tip of the core and the friction force (F_f) between the side surface of the core and the sediment. The friction force can be divided into two forces, the friction force between the inner surface of the core and the sediment ($F_{f,\mathrm{i}}$), and between the outer surface and the sediment ($F_{f,o}$). Based on three sampling patterns, we can define the reaction force mathematically.

Case I. Linear Motion, L

When the sampling pattern is only linear motion, we can simply define the reaction force as below:

$$\begin{aligned} F_{R,L} &= Q_{t,L} + F_{f,\mathrm{i},L} + F_{f,o,L} \\ &= A_t \int_0^H f_1(z)dz + 2\pi r_{\mathrm{i}} \mu_f \int_0^h f_2(z)dz \int_0^h dz \\ &+ 2\pi r_{\mathrm{i}} \mu_f \int_0^H f_2(z)dz \int_0^H dz \end{aligned} \tag{4.4}$$

where A_t is the area of the tip of the core, $f_1(z)$ is the function of the pressure acting on the tip of the core, $f_2(z)$ is the function of the pressure acting on the inner surface of the core, and $f_3(z)$ is the function of the pressure acting on the outer surface of the core.

Case II. Linear and Rotational (one direction) Motion, $L + R_1$

When the rotational motion is added, direction of the motion must be considered based on the linear displacement by linear velocity, and the circular displacement by angular velocity. Then, we can define direction of the motion with an angle respect to the z-direction, angle of attack, θ_c and the reaction force becomes,

$$\begin{aligned} F_{R,L,R_1} &= Q_{t,L,R_1} + F_{f,\mathrm{i},L,R_1} + F_{f,o,L,R_1} \\ &= Q_{t,L,R_1} + F_{f,\mathrm{i},L} \cos\theta_c + F_{f,o,L} \cos\theta_c \\ &= A_t \int_0^H f_1(z)dz \\ &+ 2\pi r_{\mathrm{i}} \mu_f \cos\theta_c \int_0^h f_2(z)dz \int_0^h dz \\ &+ 2\pi r_o \mu_f \cos\theta_c \int_0^H f_2(z)dz \int_0^H dz. \end{aligned} \tag{4.5}$$

Since the range of the angle of attack is, $0 < \theta_c < \pi/2$, the reaction force of the L, R_1 is always smaller than the reaction force of the linear motion, $F_{R,L,R_1} \leq F_{R,L}$.

Case III. Linear and Rotational (direction changing) Motion, L, R_2

In the case of direction changing rotational motion, the friction force changes depending on the number of cycle and angle of the rotation, θ_{R_2}. For example, when the core had one cycle rotation to reach to the penetration depth, H, and the rotation angle is $\pi/2$, the reaction force becomes,

$$\begin{aligned} F_{R,L,R_2} &= Q_{t,L,R_2} + F_{f,\mathrm{i},L,R_2} + F_{f,o,L,R_2} \\ &= A_t \int_0^H f_1(z)dz \\ &+ \pi/2 r_\mathrm{i} \mu_f \cos\theta_c \int_0^h f_2(z)dz \int_0^h dz \\ &+ \pi/2 r_o \mu_f \cos\theta_c \int_0^H f_2(z)dz \int_0^H dz. \end{aligned} \tag{4.6}$$

In this example case, the reaction force is smaller than the L, R_1 case. However, this conclusion does not applies to all cases. With same angular velocity, the friction force of the L, R_2 can be vary depends on the rotation angle and the number of cycle.

Case IV. Hammering Motion

The idea of the hammering motion was to support penetration. The hammering motion supports penetration by injecting a series of impulse forces to the coring tube using an electromagnetic solenoid. The hammering frequency is $1Hz$ and hammering impact force changes depending on the distance between the hammer and coring tube, d_H. Hammering effect can reduce the reaction force when penetration depth has increased due to the hammering motion. The amount of the reaction force reduction can be determined by the ratio between the ideal penetration depth by hammering (D_H) and actual penetration depth by hammering (D_h). However, when the actual penetration depth is smaller than the ideal penetration depth by hammering ($D_h < D_H$), the reaction force is generated due to the hammering motion. The amount of the reaction force increase can be determined by the ratio between the ideal penetration depth by hammering (D_H) and remaining penetration

depth by hammering ($D_H - D_h$). In the case of $L + R_2$ with hammering motion, we can define the reaction force as follows:

$$F_{R,L,R_2,H} = Q_{t,L,R_2,H} + F_{f,\mathrm{i},L,R_2,H} + F_{f,o,L,R_2,H} \tag{4.7}$$

where $Q_{t,L+R_2+H}$ is the bearing capacity, $F_{f,\mathrm{i},L+R_2+H}$ is the inner friction, and $F_{f,o,L+R_2+H}$ is the outer friction of the pattern, $L+R_2+H$. Each parameter is affected by the hammering motion, $\sum_{\mathrm{i}=1}^{n_{H,\mathrm{i}}} \frac{D_{h,\mathrm{i}}}{D_H} F_{H,d_H} - \sum_{\mathrm{i}=1}^{n_{H,\mathrm{i}}} (1 - \frac{D_{h,\mathrm{i}}}{D_H}) F_{H,d_H}$ and n_H is number of hammering, $D_{h,\mathrm{i}}$ is the actual penetration depth of each hammering, and F_{H,d_H} is the impact force of each hammering.

In summary, the hammering motion can increase or decrease the reaction force depending on the performance of the hammering.

Energy

The input energy is based on the linear velocity (w_c) and angular velocity (ω_c) of the coring tube, and the impact force (F_{H,d_H}) and displacement (D_h) by hammering motion. The output energy is based on the reaction force (F_R) and the total penetration depth (H). We can define the energy equation ($E_{in} = E_{out} + E_{loss}$) of the USS during sampling as below:

$$\frac{1}{2} {w_c}^2 + \frac{1}{2} I_c {\omega_c}^2 + \sum_{\mathrm{i}=1}^{n_{H,\mathrm{i}}} D_{h,\mathrm{i}} F_{H,d_H} = \int_0^H f_{F_R}(z) dz + E_{loss} \tag{4.8}$$

where $KE = \frac{1}{2} {w_c}^2$ is the kinetic energy by linear velocity, $AE = \frac{1}{2} I_c {\omega_c}^2$ is the angular energy by angular velocity, $\sum_{\mathrm{i}=1}^{n_{H,\mathrm{i}}} D_{h,\mathrm{i}} F_{H,d_H}$ is the sum of impact energy by hammering, $\int_0^H f_{F_R}(z) dz$ is the output energy, and E_{loss} is the energy loss due to the penetration. The energy efficiency can be expressed based on $E_{\mathrm{i}n}$ and E_{out}, as $\frac{E_{out}}{E_{\mathrm{i}n}} \times 100(\%)$.

Unstable Condition - Lifting

The lifting can be one of the unstable conditions when the reaction force is getting greater than the total down force of the USS, $F_{USS} < F_R$. By applying energy equation, we can define the lifting phenomenon as follows:

$$\begin{aligned} \frac{1}{2}{w_c}^2 + \frac{1}{2}I_c{\omega_c}^2 + \sum_{\mathrm{i}=1}^{n_{H,\mathrm{i}}} D_{h,\mathrm{i}}F_{H,d_H} = \int_0^{H_a} f_{F_R}(z)dz \\ + \int_{H_a}^{H} f_{F_R}(z)dz - F_{USS}H_{lift} + E_{loss} \end{aligned} \tag{4.9}$$

where $\int_0^{H_a} f_{F_R}(z)dz$ is the work done by reaction force and actual penetration depth (H_a), and $H_{lift} = H - H_a$ is the height of the lift.

4.4 System Architecture

The system architecture is sketched in Fig. 4.12. In the system, we use a laptop as the base station to monitor and control the real-time situation of the USV and USS from the shore. A single-board computer is used as the main controller of the system that is in charge of sub-systems of the USV and the USS. To guarantee wireless communication, we make the single-board computer as a *ROS Master* and connect the laptop with it using WiFi, which is proven to have a much longer communication distance than other communication method such as Bluetooth. We connect the USS to the single-board computer via serial communication.

4.4.1 USV - System Architecture

In the system architecture of the USV, as shown in Fig. 4.13, two microprocessors and the USB camera are connected to the main controller (single-board computer, namely (NVIDIA Jetson Nano). One microprocessor (Arduino UNO) is fused with the GPS sensor and an electronic compass to transmit and store the current position of the USV. Another micro-

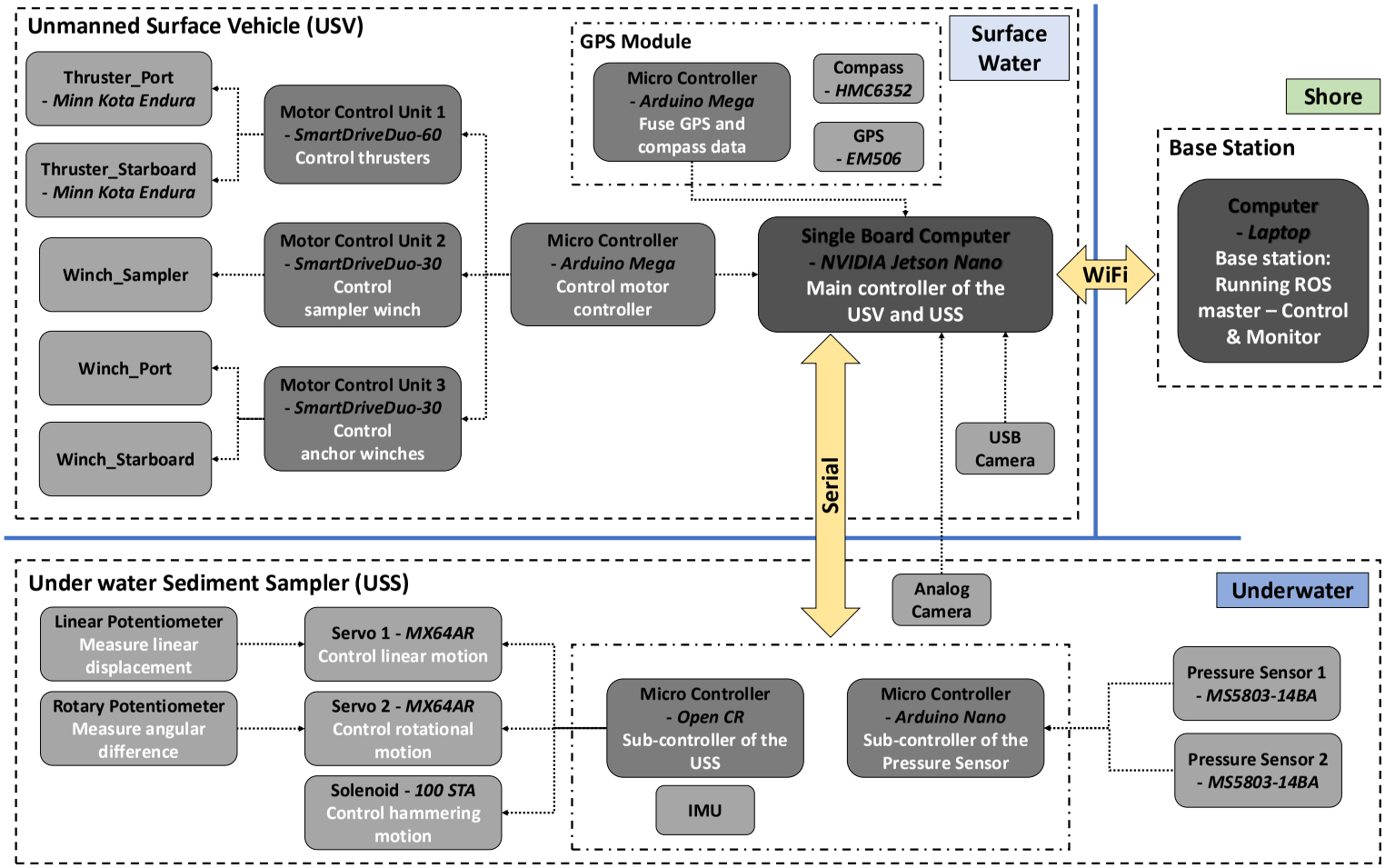

Figure 4.12. Overall system architecture of the uncrewed sediment sampling system.

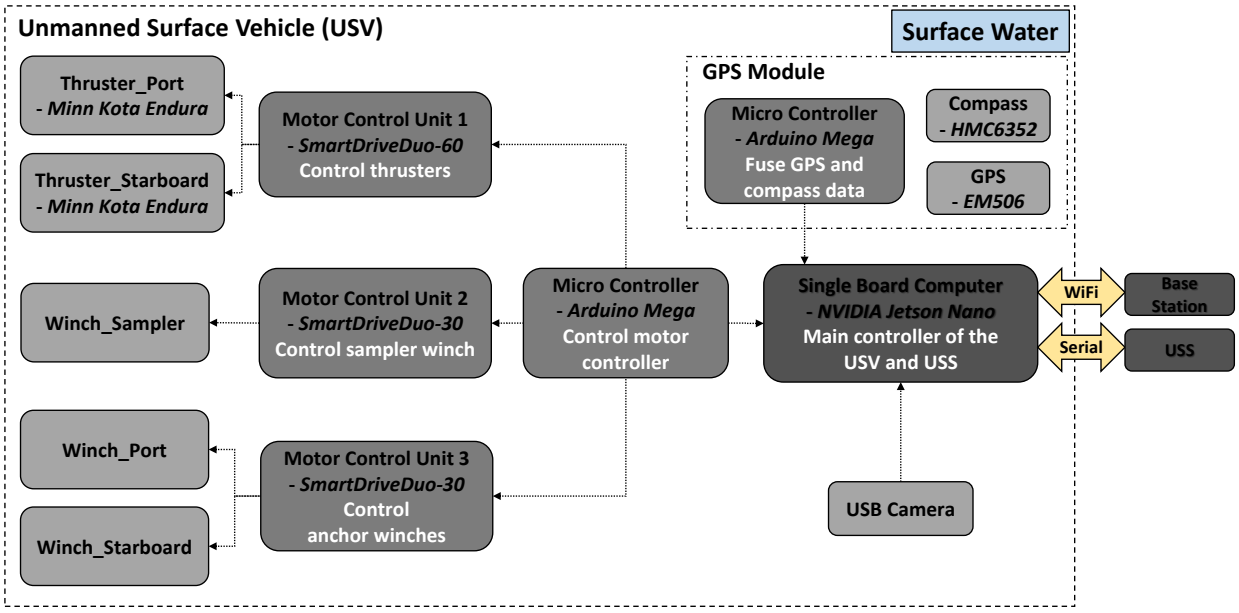

Figure 4.13. System architecture of the USV.

processor (Arduino Mega) is used to control the winches for anchoring and USS launching and thrusters via serial communication.

A manual control mode for USV is realized based on the propulsion and navigation system of the USV. In manual navigation mode, we use a manual control node and send commands directly from the user to the USB. To enable full functionalities of the USV in sediment sampling, we incorporated winches for the USS and anchors and two thrusters. Sampler winch and anchor winch modules are encapsulated as a *ROS node* and they must subscribe to the *ui node* via the single-board computer. Along with the UI, we can further control winches for the USS and anchors as shown in Fig. 4.15. To secure real-time monitoring over the operation and in case of emergencies, we employ a laptop as the base station to provide real-time visualization. The laptop connects to the *ROS master* and can subscribe to the *USV camera node* to monitor anchoring and launching the USS.

4.4.2 USS - System Architecture

In the system architecture of the USS as shown in Fig. 4.14, a micro-controller (Open CR 1.0) publishes commands to servos and the solenoid to generate the sampling pattern and

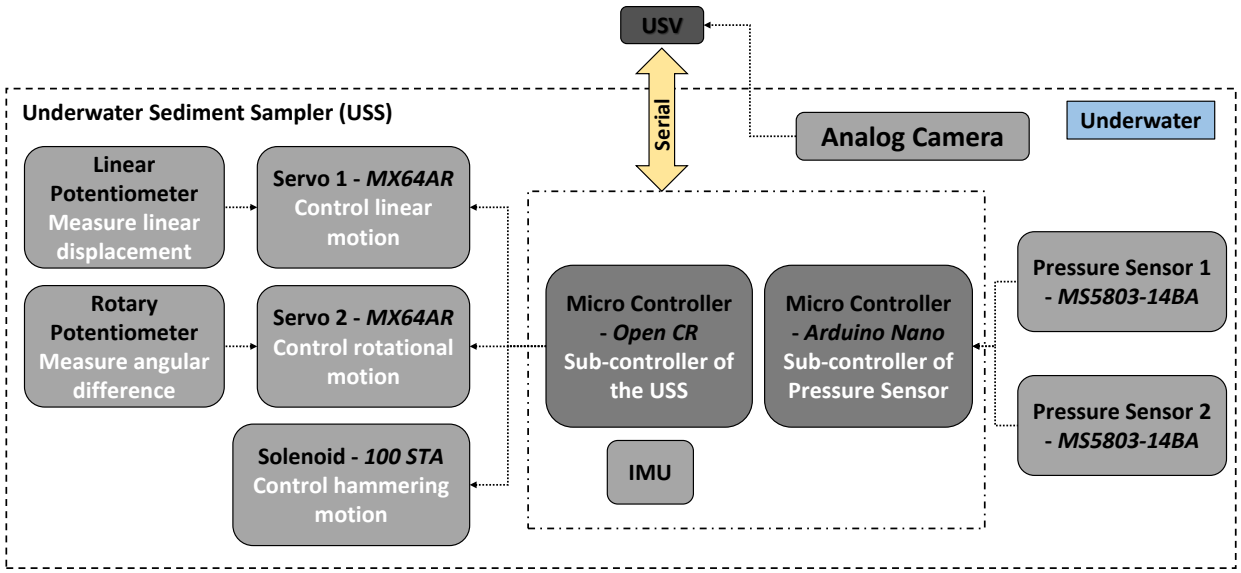

Figure 4.14. System architecture of the USS.

subscribes to data from servos, pressure sensors, linear potentiometer, rotary potentiometer, limit switches, and IMU sensor to monitor the sampling process. We used two microcontrollers. One was used to control servos and the solenoid, while the other was for pressure sensors to prevent conflict of data communication. Servo 1 controlled the linear motion and the linear potentiometer measures the displacement of the compression during the penetration. Servo 2 controlled the rotational motion and the rotary potentiometer measures the actual rotation angle of the coring tube. The solenoid is to generate the hammering motion, whereas pressures sensors are used to estimate the depth of the USS based on the pressure data. The reason why we used two pressure sensors is to calibrate the density of the water based on the data from the two sensors.

The user can control linear, rotational, and hammering motion via the graphic user interface (GUI) as shown Fig. 4.15. Furthermore, the user can monitor the pressure data and converted depth data from the UI as depicted in Fig. 4.15. We installed an analog camera to monitor the coring tube while the USS is underwater.

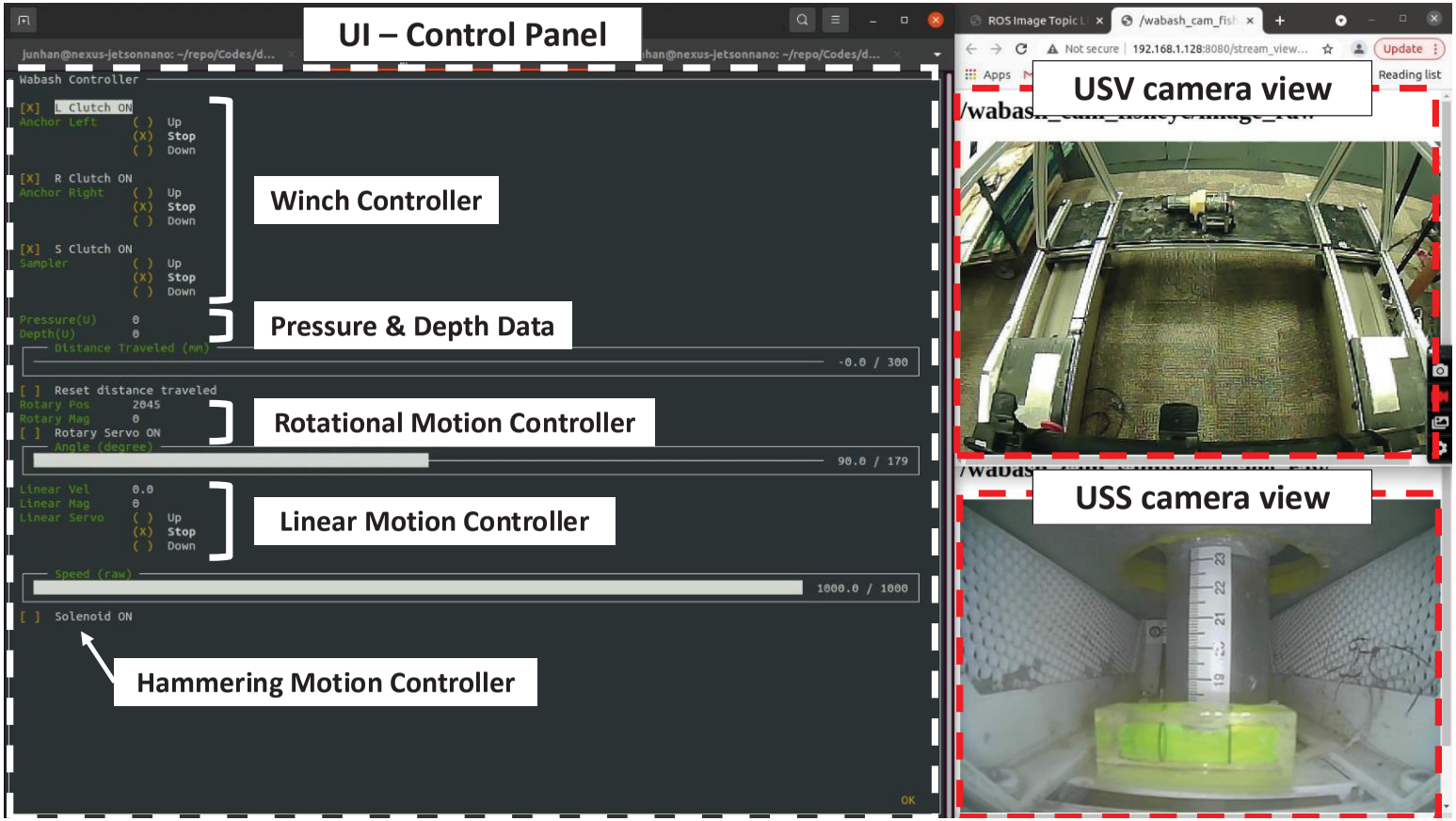

Figure 4.15. UI of the uncrewed sediment sampling system, and the USV and USS camera view.

5. EXPERIMENT

5.1 Sediment Sampling Pattern Test

The main objective of the sediment sampling pattern test is to discover the effectiveness of the hammering motion, rotational motion range, and linear motion velocity based on the reaction force and work done (energy) of each pattern.

5.1.1 Sediment Sampling Pattern Test Setup

For sediment sampling pattern test, we prepared a lab test environment, using coarse sand as the test sediment. Input variables of each motion are: Linear motion velocity, $w_c \in 6.5, 4.875, 3.25$ (mm/s), Rotational motion range, $w_c \in 60, 90, 120$ ($^\circ$), and presence of Hammering motion $H \in On, Off$. Based on the input variables of each motion, we generated 18 sampling patterns.

5.1.2 Hammering Motion Effect

Hammering motion is used to support the penetration of the coring tube. However, the reaction force can be reduced or increased depending on the hammering motion performance.

We used nine combinations to generate sampling patterns based on the input variables of the linear velocity and the rotational motion range. Each pattern was tested with or without the hammering motion. We compared the maximum reaction force and work-done (output energy) of each pattern, as shown in Fig. 5.1, 5.2, 5.3, 5.4, and 5.5. The blue lines and bars depict 'Hammering: On', whereas the red lines and bars depict 'Hammering: Off'. In the case of linear motion velocity, 6.5 mm/s, regardless of the rotation angle, the maximum reaction force of patterns with hammering was smaller than the force of the patterns without hammering, as shown in Fig. 5.1. However, in the cases of linear motion velocity, 4.875 mm/s and 3.25 mm/s, regardless of the rotation angle, the maximum reaction force of patterns without hammering were smaller than the patterns with hammering as shown in Fig. 5.2 and Fig. 5.3.

To summarize, in patterns with linear motion velocity 6.5 mm/s, the hammering motion reduced the reaction force during sampling. However, in the cases of the linear motion velocities 4.875 mm/s and 3.25 mm/s, hammering motion did not reduce the reaction force. In the case of the linear motion velocity 6.5 mm/s with the three rotational motion ranges $60, 90, 120$ ($^\circ$) ($L6.5R60, L6.5R90, L6.5R120$), $L4.875R90$, and $L3.25R90$, the hammering motion reduced the energy required to penetrate, which is depicted in Fig. 5.4.

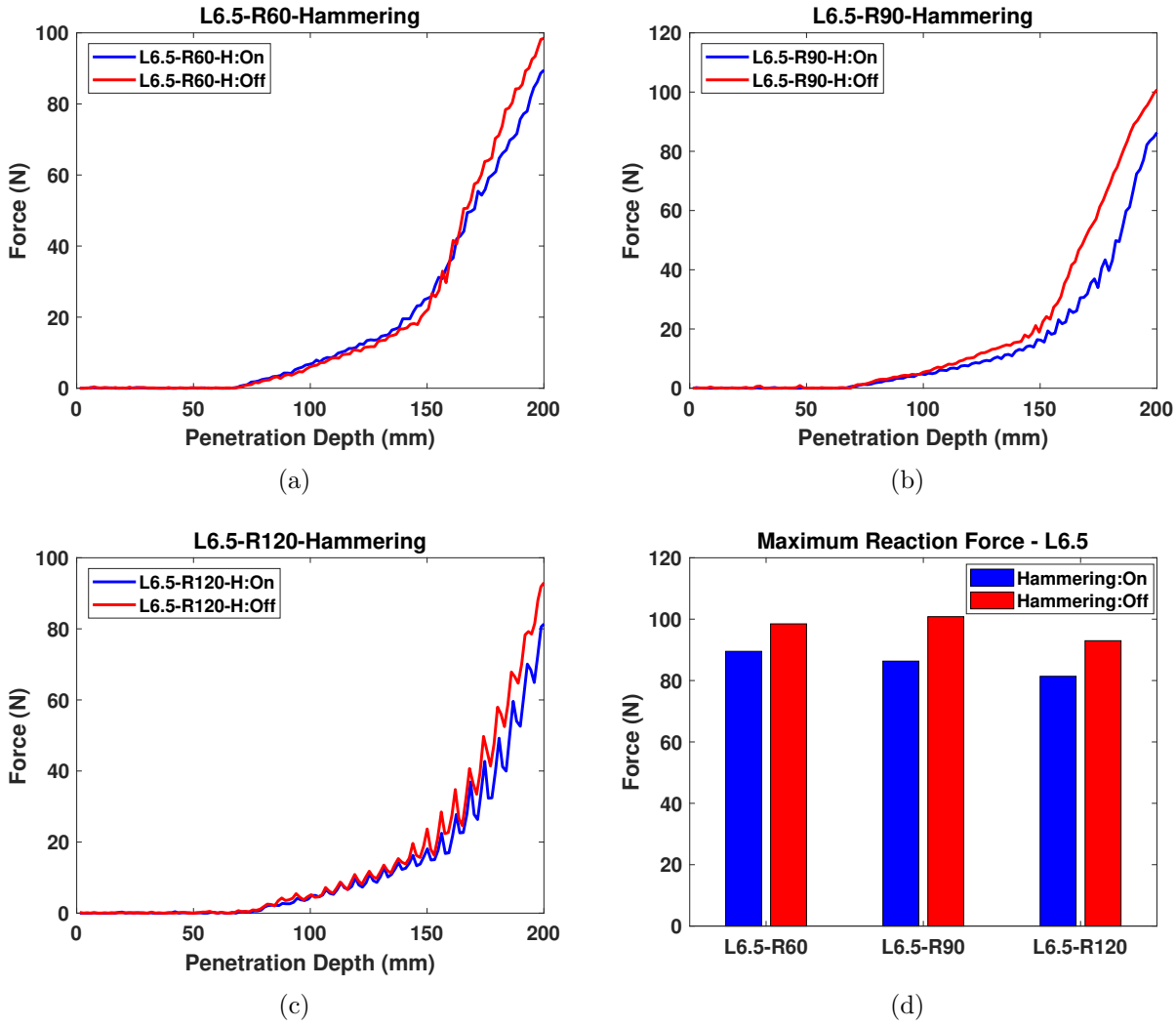

Figure 5.1. Force diagram of sampling patterns based on the presence or absence of hammering motion: (a) Force data of $L6.5-R60$, (b) Force data of $L6.5-R90$, (c) Force data of $L6.5-R120$, and (d) Comparison of the max. reaction force among three patterns.

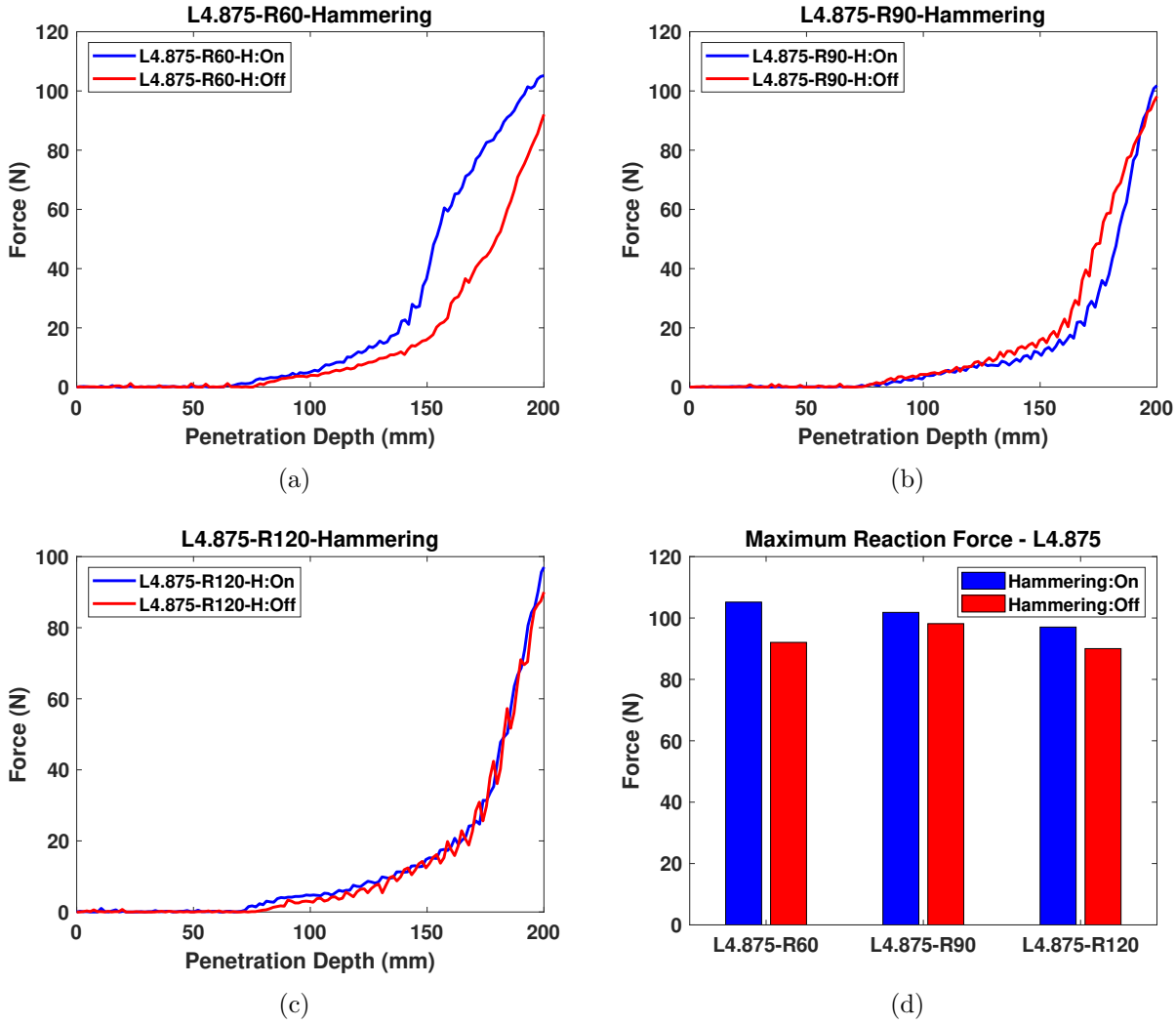

Figure 5.2. Force diagram of sampling patterns based on the presence or absence of hammering motion: (a) Force data of $L4.875 - R60$, (b) Force data of $L4.875 - R90$, (c) Force data of $L4.875 - R120$, and (d) Comparison of the max. reaction force among three patterns.

5.1.3 Rotational Motion Range Comparison

Given the linear motion velocity with the hammering motion, we observed that the maximum reaction force decreased as the rotation range increased, can be seen in Fig. 5.1, 5.2, and 5.3. Moreover, the work-done (output energy based on the reaction force) decreased as the rotation angle increased except when the linear motion velocity is 4.875 mm/s, and the rotational motion angle is 120°, as shown in Fig. 5.4. The work-done decreased significantly

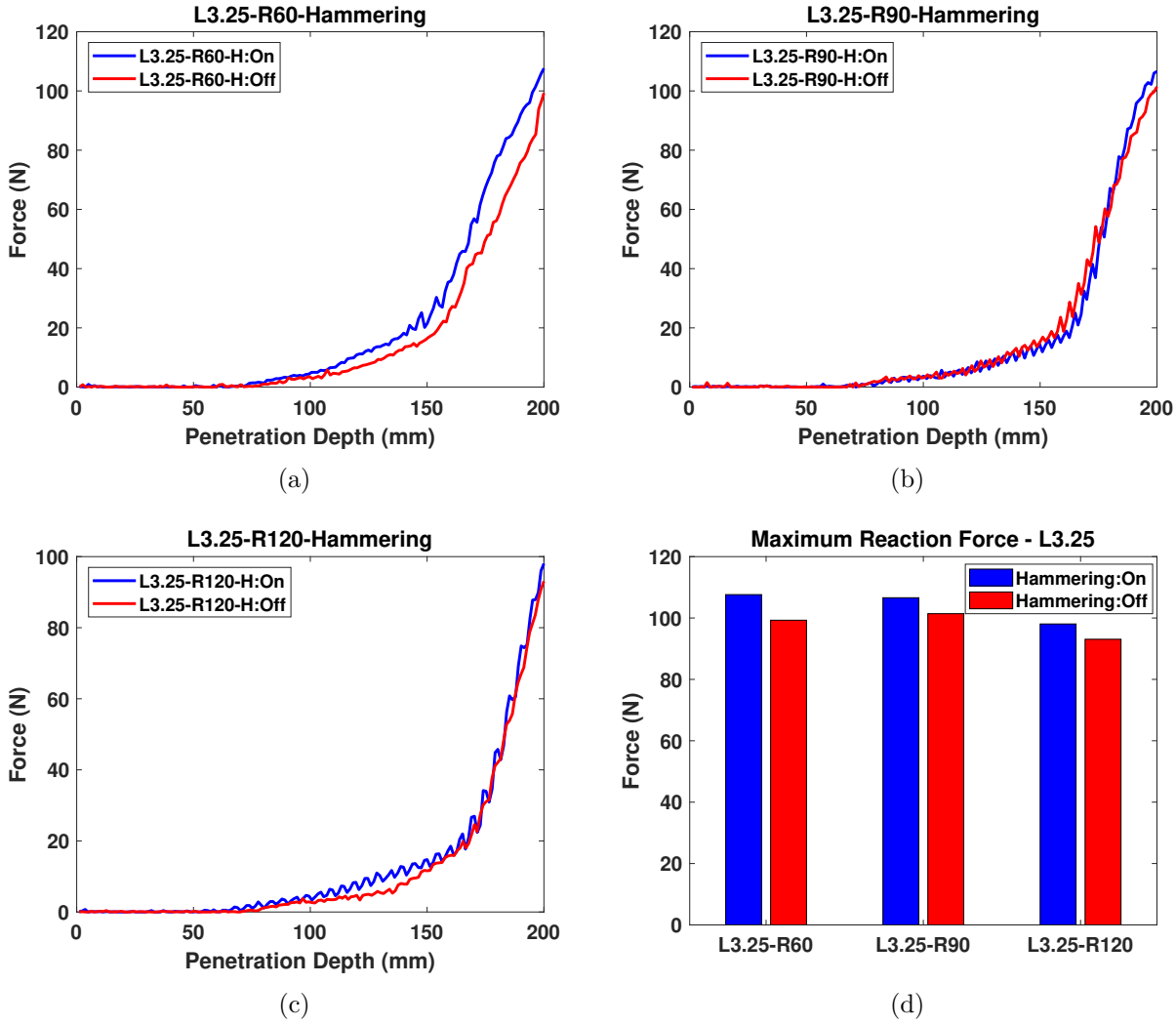

Figure 5.3. Force diagram of sampling patterns based on the presence or absence of hammering motion: (a) Force data of $L3.25-R60$, (b) Force data of $L3.25-R90$, (c) Force data of $L3.25-R120$, and (d) Comparison of the max. reaction force among three patterns.

from 60° to 90°, however, the work-done marginally increased as the rotational motion angle increased to 120°, as shown in Fig. 5.4 (b).

In summary, regardless of the linear motion velocity and the hammering motion, patterns with the rotational motion angle 120° have the lowest maximum reaction force among other patterns that have the same linear motion velocity.

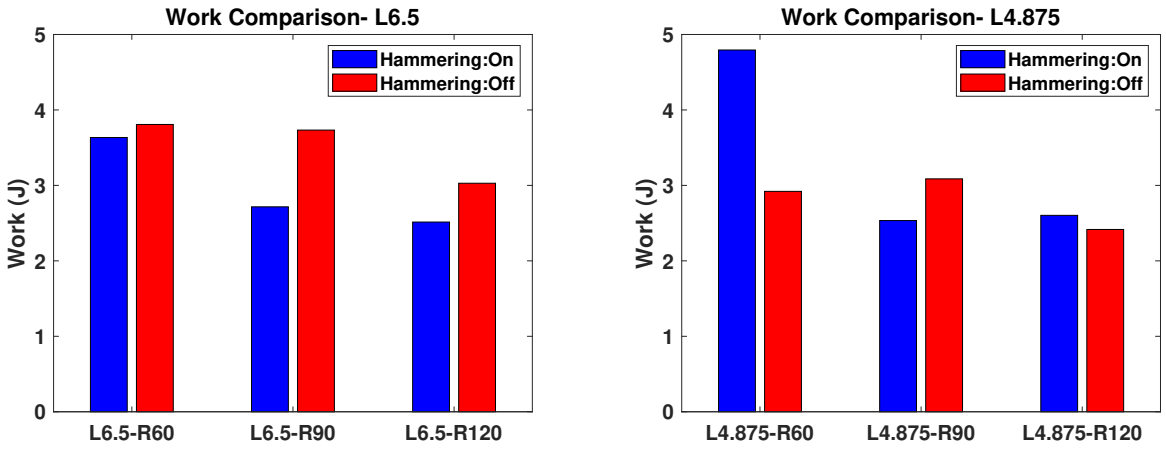

(a)

(b)

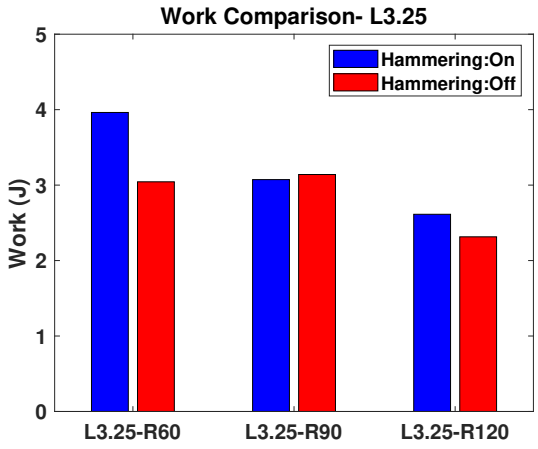

(c)

Figure 5.4. Comparison of the Work-done (output energy) diagram of nine patterns based on the presence or absence of hammering motion.

5.1.4 Linear Motion Speed Comparison

Given the rotational motion angle with the hammering motion, the reaction force increased as the linear motion velocity decreased, which can be seen in Fig. 5.5. However, the work-done had no particular pattern as the linear motion velocity decreased. Pattern without hammering motion, no significant changes in maximum reaction force and work-done.

In summary, *L6.5-R120-H:On* pattern showed the lowest maximum reaction force and work-done among nine patterns. Based on the sampling pattern test, the optimal sediment

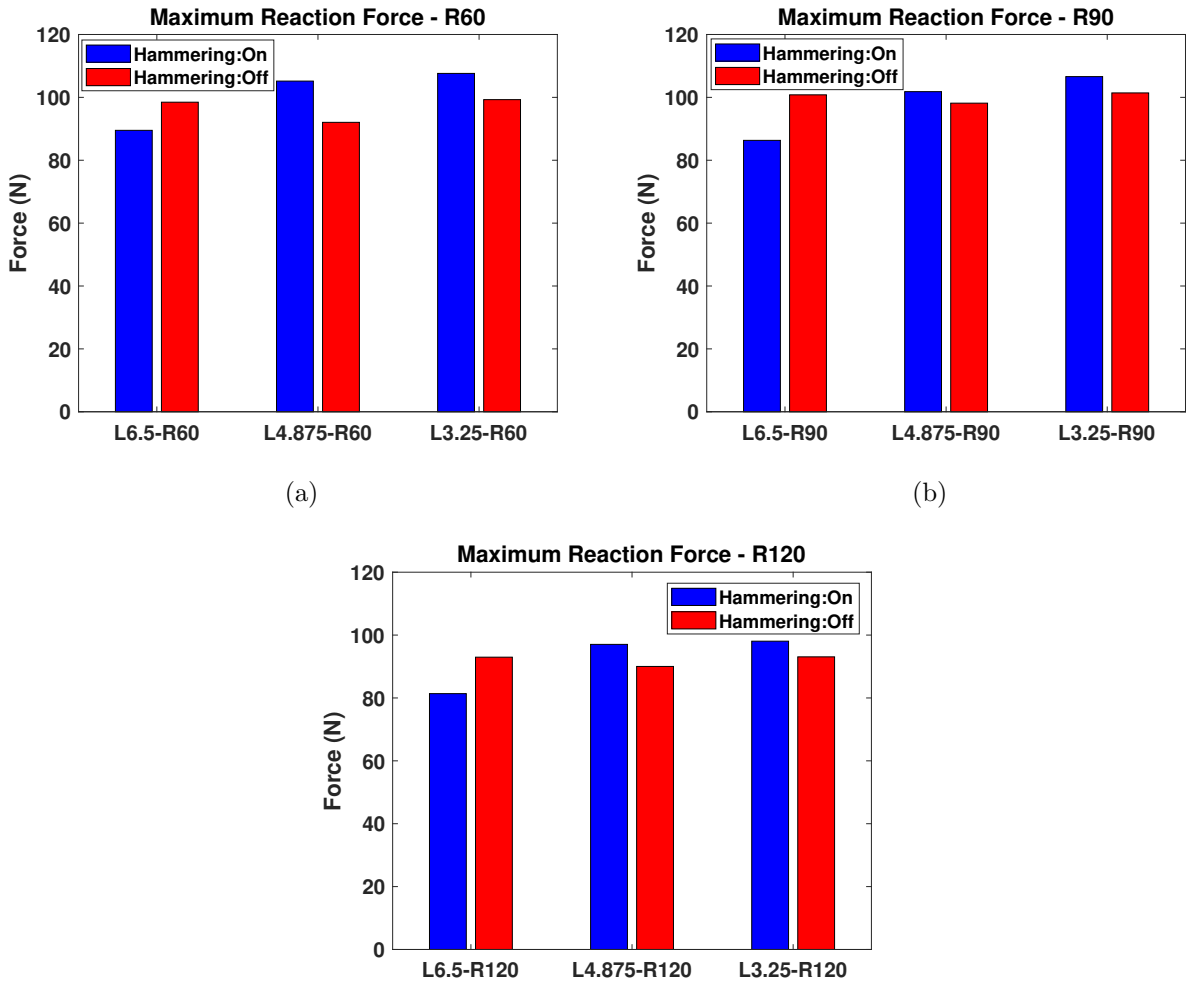

Figure 5.5. Comparison of max. reaction force diagram of nine patterns based on the presence or absence of hammering motion.

sampling pattern can be the *L6.5-R120-H:On* pattern in terms of the maximum reaction force and the energy required to penetrate the sediment.

5.2 Field Experiment

We conducted extensive field experiments to evaluate the effectiveness of our complete system. For all outdoor trials, we controlled and monitored this system from the base station via wireless communication.

5.2.1 Field Experiment Setup

The location of the field experiment is one of the retention ponds near the N. 100 W, West Lafayette (40.470137, -86.926809) operated by the PRF (Purdue Research Foundation). The base station of the uncrewed sediment sampling system consists of a laptop as a control and monitor station, and an access point to communicate with USV and USS as shown in Fig. 5.6.

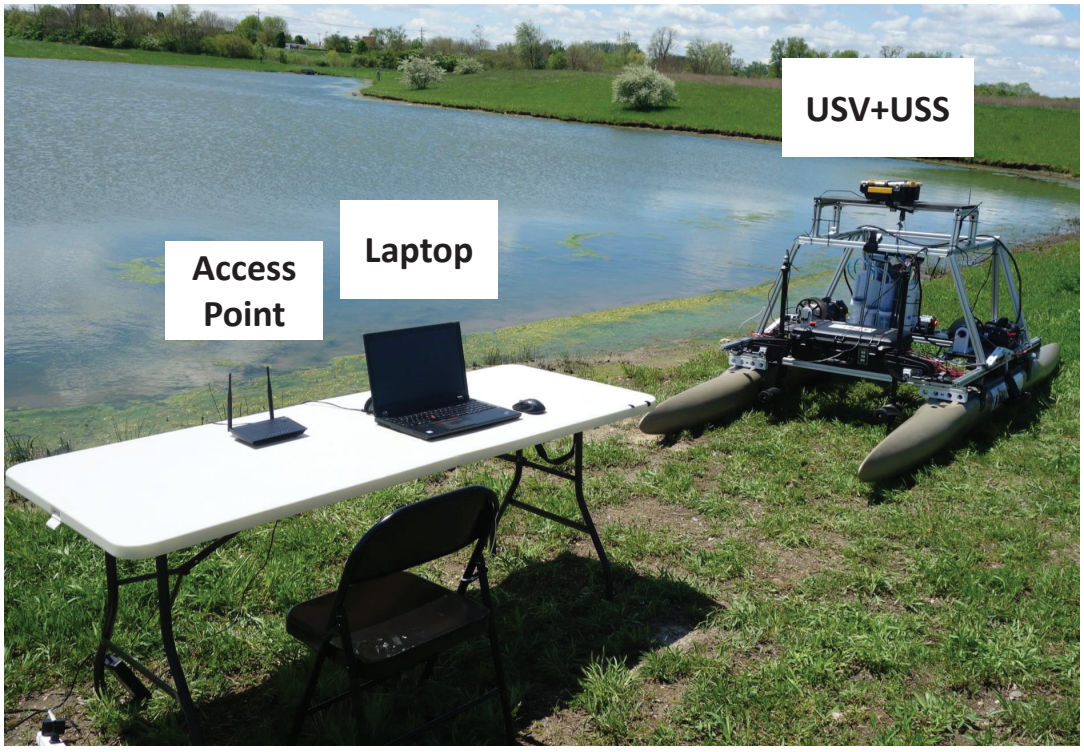

Figure 5.6. Base station of the uncrewed sediment sampling system with a laptop and an access point for a remote operation.

5.2.2 Field Experiment Scenario

An experiment scenario is based on the procedure of the uncrewed sediment sampling system. We deploy the USV to the desired sampling area via manual control that can be seen in Fig. 5.7(a). When the USV arrives at the desired sampling area, we launch anchors to maintain the position of the USV as shown in Fig. 5.7(b). Next, we launch the USS to the bottom of the water to collect a sediment sample, as shown in Fig. 5.7(c). Once the USS successfully lands at the sediment bed, the coring tube starts penetrating the sediment based on the optimal sampling pattern, which is shown in Fig. 5.8(a). When the penetration is completed, we retrieve the coring tube to capture the sediment. After the sampling process, we return the USS to the USV, as shown in Fig. 5.8(b). Next, we navigate the USV back to the shore near the base station, as shown in Fig. 5.8(c). The final step is to retract the coring tube into the USS.

5.2.3 Result

In the *Deploying* and the *Positioning* states, we collected GPS data to find the trajectory of the USV. In the *Launching* and the *Sampling* states, we measured pressure data to track the depth of the water at the sampling area, IMU data to find the orientation of the USS during launching and sampling, and potentiometer data to calculate the reaction forces acting on the USS.

Deploying and Positioning

The sampling point of Trial 1 from the field experiment was $(40.47007678, -86.92694018)$, based on the GPS coordinates. The distance from the base station was 38 m. The red line shows the trajectory of the USV when deploying, and the blue line shows the trajectory while positioning, as shown in Fig. 5.9(a). During the positioning, the GPS data changed 30 times and the accumulated maneuvering distance of the USV was approximately 12 m within the maneuvering range of approximately 7 m^2.

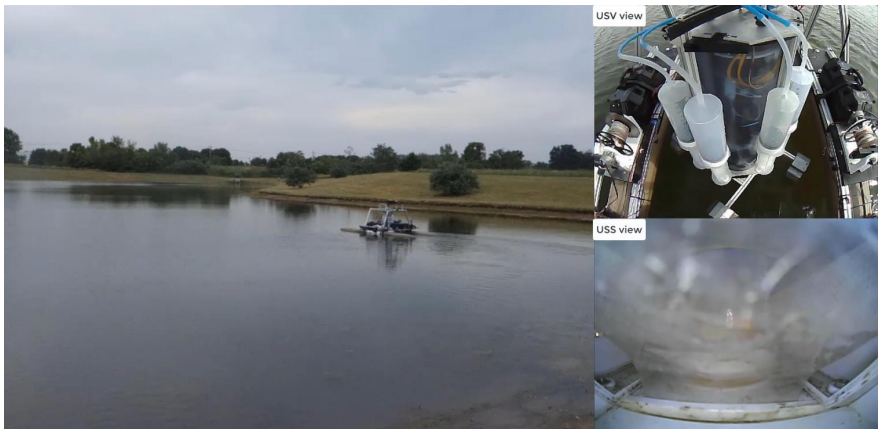

(a)

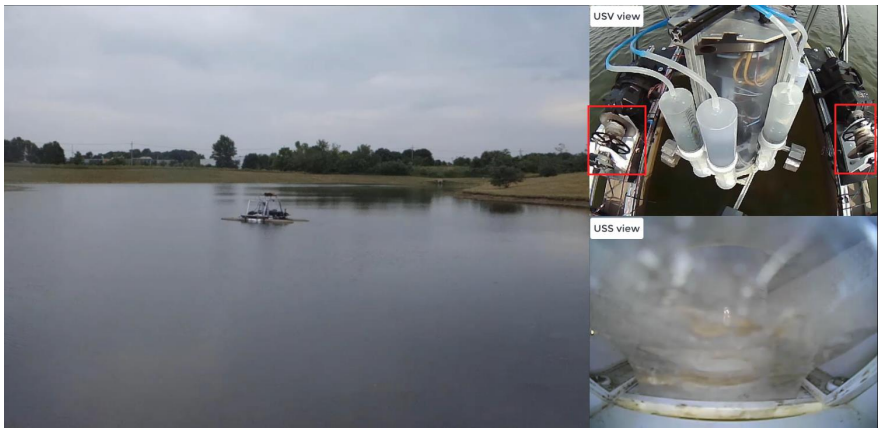

(b)

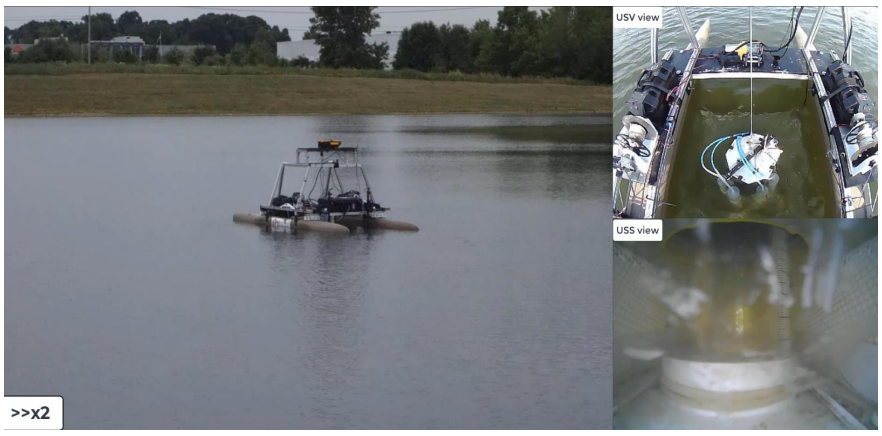

(c)

Figure 5.7. The first part of procedure of the uncrewed sediment sampling system: (a) Deploying, (b) Positioning, and (c) Launching.

(a)

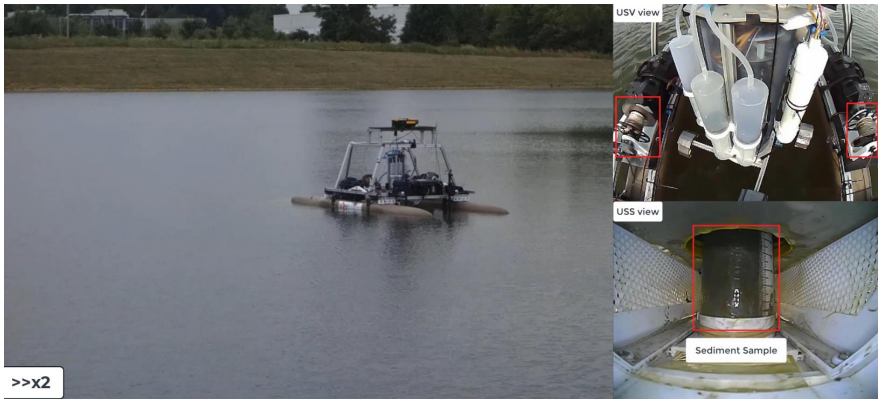

(b)

(c)

Figure 5.8. The second part of procedure of the uncrewed sediment sampling system: (a) Sampling, (b) Retrieving of the USS and anchors, and (c) Returning of the USV.

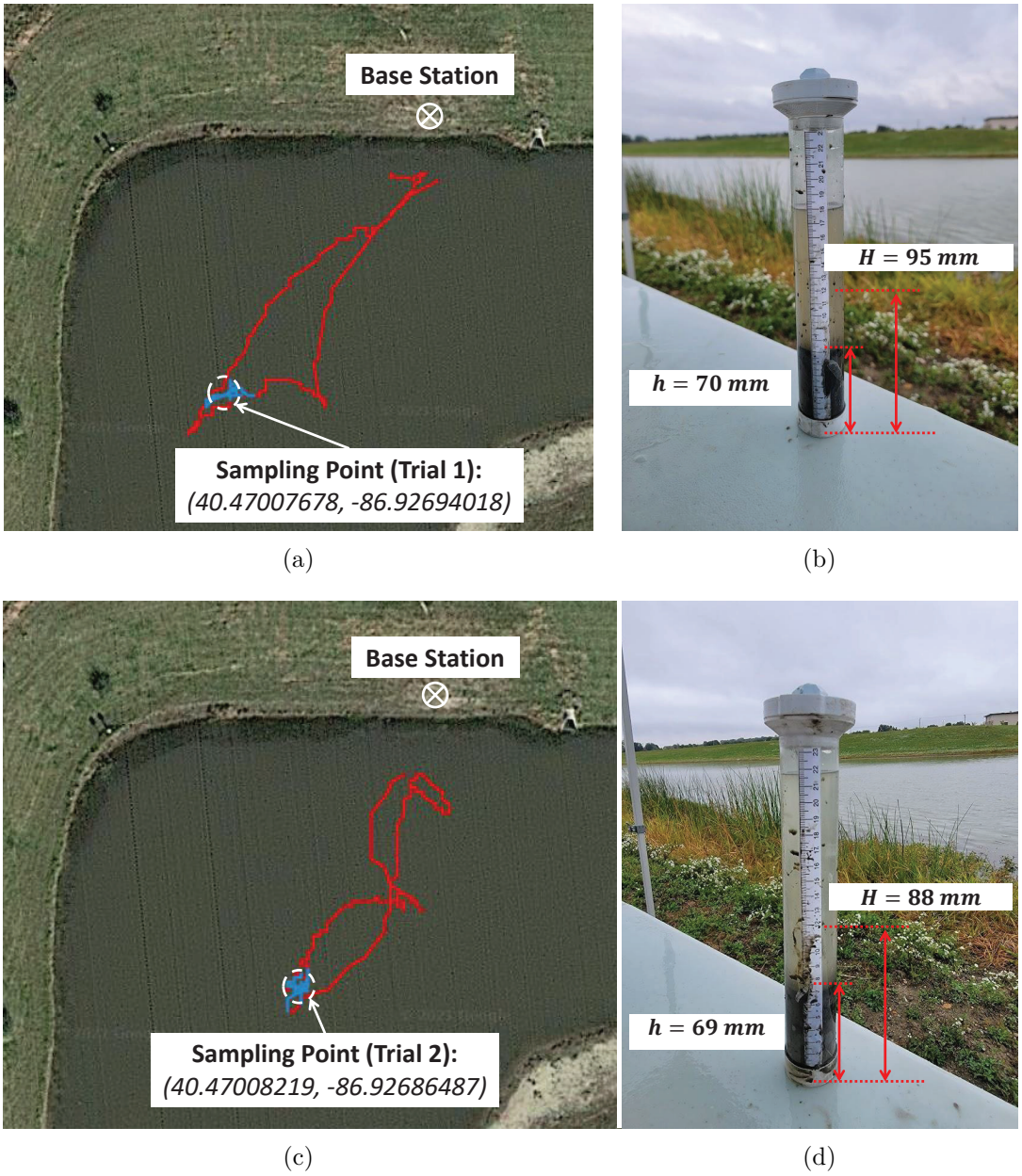

Figure 5.9. (a) Trajectory of the USV (a distance between the base station and sampling point is 38 m in a straight line) from Trial 1, and (b) Collected sediment sample with the off-the-shelf coring tube from Trial 1, (c) Trajectory of the USV (a distance between the base station and sampling point is 34 m in a straight line) from Trial 2, and (d) Collected sediment sample with the off-the-shelf coring tube from Trial 2.

The sampling point of Trial 2 from the field experiment was $(40.47008219, -86.92686487)$ based on the GPS coordinate and the distance from the based station was 34 m. The red

line demonstrates the trajectory of the USV during deploying, while the blue line shows during positioning as depicted in Fig. 5.9(c). During the positioning, the GPS data changed 30 times and the accumulated maneuvering distance of the USV was approximately 26 m within the maneuvering range of approximately 4 m^2.

Sampling Depth

The sampling depth of the USS from Trial 1 was 2.38 m as shown in Fig. 5.10(a). The blue line shows the depth change during submerging, which took approximately 38 seconds to land at the bottom. The yellow line represents the depth data during sampling. The red line is for penetration, and the green line is for retrieval of the USS. The cyan blue line shows the depth during retrieval. We can observe an interesting phenomenon from the depth data. During penetration (red line) of the sediment, we could observe that the depth was decreased, which implies that the USS was lifted during penetration. The main cause of lifting can be the reaction force when it is greater than the net negative buoyancy force of the USS. From the data, the USS was lifted for approximately 10.5 cm. The whole process was completed in approximately 200 seconds, from submerging to retrieving.

The sampling depth of the USS from Trial 2 was 2.33 m as shown in the top figures of Fig. 5.11(a). The blue line shows the depth change during submerging, which took approximately 36 seconds to land at the bottom. The yellow line represents the depth date during sampling. The red line is for penetrating, as well as the green line is for retrieving. The cyan blue line depicts the depth during retrieving. A same interesting phenomenon as Trial 1 can be observed from the depth data, which decreases during penetrating (red line) the sediment, meaning that the USS was lifted during penetration. From the data, approximately 11.2 cm was lifted. The whole process took approximately 188 seconds from submerging to retrieving.

Based on the depth of the USS during submerging, sampling, and retrieving, we could find the depth of the sampling location and observe the lifting of the USS. However, we could not conclude that the USS was only lifted. We should compare the orientation data of the USS in the next section.

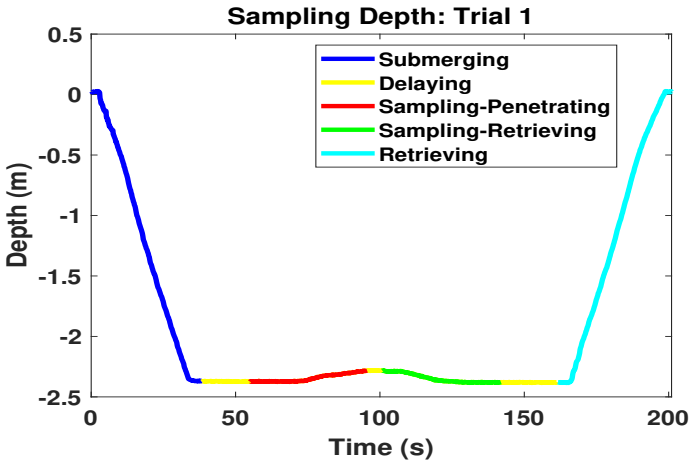

(a)

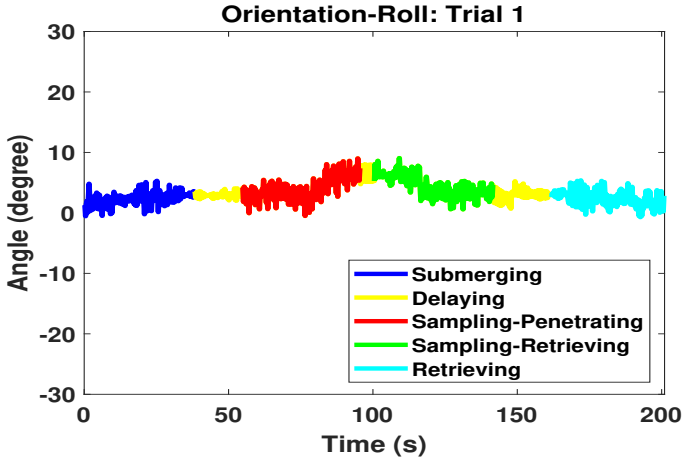

(b)

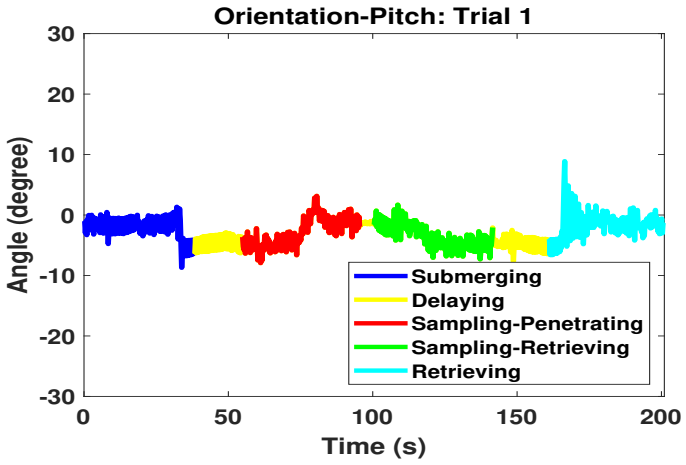

(c)

Figure 5.10. Trial 1: (a) Sampling depth of the USS, (b) Roll orientation of the USS, and (c) Pitch orientation of the USS during the sediment sampling procedure.

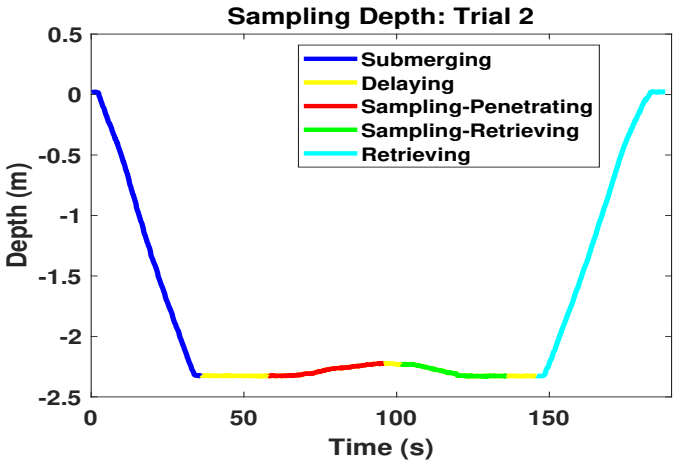

(a)

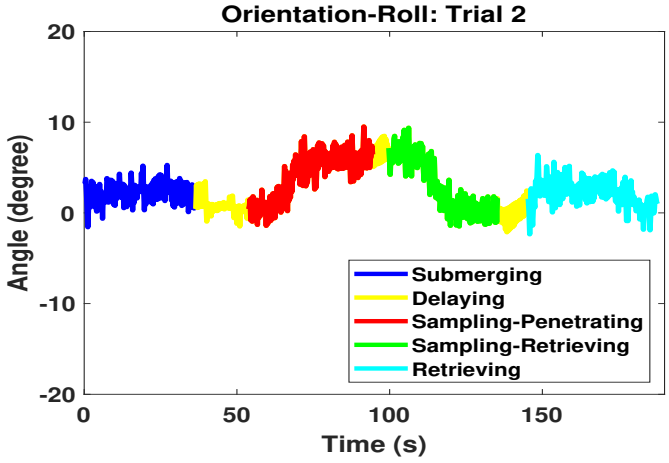

(b)

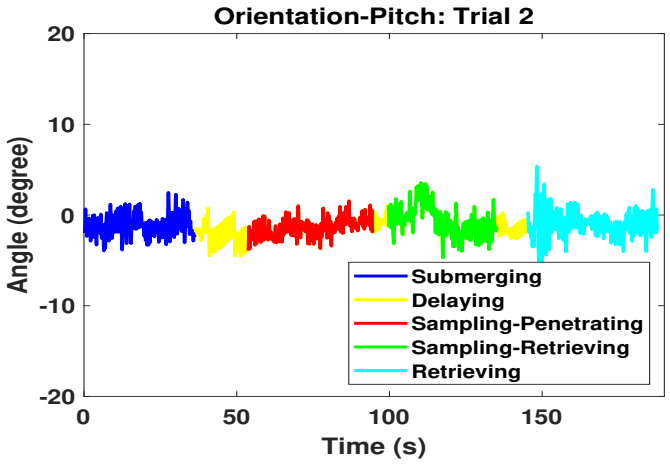

(c)

Figure 5.11. Trial 2: (a) Sampling depth of the USS, (b) Roll orientation of the USS, and (c) Pitch orientation of the USS during the sediment sampling procedure.

Orientation of the USS

The overall orientation of the USS during launching and sampling from Trial 1 is shown in Fig. 5.10(b), and 5.10(c). The blue line shows the orientation change during submerging. The yellow line represents the orientation of the USS during sampling. The red line is for penetrating, and the green line shows retrieving. The cyan blue line shows the orientation during retrieving. Total roll angle change was between -0.705 ° to 9.067 °, and pitch angle was changed between -8.725 ° to 8.906 ° during launching and sampling as shown in Fig. 5.10(b), and 5.10(c). When the USS landed at the sediment bed, the orientation of the USS was roll angle, 2.431 ° and pitch angle, -4.035 °. During the penetration, we could observe that the orientation of the USS was changed, roll angle from -0.505 ° to 9.014 ° and pitch angle from -7.949 ° to 3.164 °. The overall orientation of the USS during launching and sampling from Trial 2 is shown in Fig. 5.11(b), and 5.11(c). The blue line shows the orientation change during submerging. The yellow line represents the orientation of the USS during sampling. The red line is for penetrating, and green line is for retrieving. The cyan blue line shows the orientation during retrieving. Total roll angle change was between -0.705 ° to 9.067 °, and pitch angle was changed between -8.725 ° to 8.906 ° during launching and sampling as shown in Fig. 5.11(b), and 5.11(c). When the USS landed at the sediment bed, the orientation of the USS was roll angle, 3.048 ° and pitch angle, -2.424 °. During the penetration, we could observe that the orientation of the USS was changed, roll angle from -1.429 ° to 9.526 ° and pitch angle from -3.926 ° to 1.557 °.

According to orientation data, the USS has toppled approximately 9 ° in roll and 3 ° in pitch from Trial 1 and approximately 9.5 ° in roll and 1.6 ° in pitch from Trial 2. If we assume that the USS was not lifted, with the collected roll and pitch angle of the USS, the depth change might be approximately 4 cm, not approximately 10 cm as we observed. In conclusion, the USS was both lifted and toppled during the penetration.

Reaction Force

From Trial 1, the reaction force occurs while the coring tube is penetrating the sediment as shown in Fig. 5.12(a). The red line is the reaction force during penetration, and the green

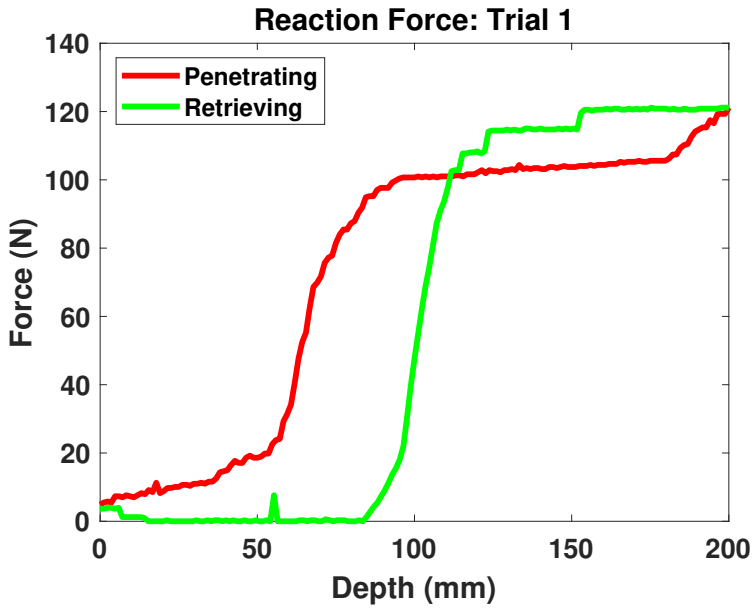

(a)

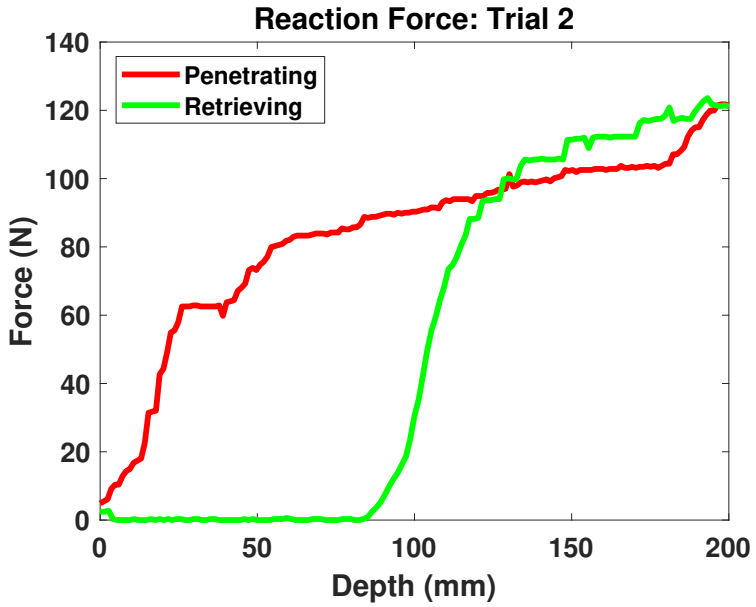

(b)

Figure 5.12. Reaction force of the USS during sampling, (a) Trial 1 and (b) Trial 2.

line is during retrieving. The reaction force is the indicator of the lifting phenomenon and work-done (output energy). Based on the reaction force and actual penetration depth, we can calculate the work-done, which is the required energy to penetrate the sediment. In this

trial, lifting was approximately 10.5 cm. At the depth of 95 mm from the Fig. 5.12(a), the USS started lifting, and we can observe flat region from the red line.

From Trial 2, the reaction force occurs while the coring tube is penetrating the sediment as shown in Fig. 5.12(b). The red line is the reaction force during penetration, and the green line is during retrieving. The reaction force is the indicator of the lifting phenomenon and work-done (output energy). Based on the reaction force and actual penetration depth, we can calculate the work-done, which is the required energy to penetrate the sediment. In this trial, lifting was approximately 11.2 cm. At the depth of 88 mm from the Fig. 5.12(b), the USS started lifting, and we can observe flat region from the red line.

Sediment Samples

We successfully collected sediment samples from the bottom of the water. From Trial 1, the penetration depth (H) was 95 mm and the core's length (h, height of the collected sediment sample) was 70 mm. The recovery ratio (h/H) of the sediment sample from the trial was $70 : 95 = 1 : 1.267$ as shown in Fig. 5.9(b). From Trial 2, the penetration depth was 88 mm and the core's length (height of the collected sediment sample) was 69 mm. The recovery ratio (h/H) of the sediment sample from the trial was $69 : 88 = 1 : 1.275$ as shown in Fig. 5.9(d).

The main reason for the core's length (h) being shorter than the penetration depth (H) is that as the core penetrates, the sediment below the tip of the core moves laterally away and the sediment inside of the core is compressed [61].

6. DISCUSSION

In this section, we discuss three major topics regarding the proposed research: 1) Design of the uncrewed sediment sampling system, 2) Field experiments, and 3) Autonomous sediment sampling system.

6.1 Design of the Uncrewed Sediment Sampling System

6.1.1 Novel Design of the USS

The novelty of the uncrewed sediment sampling system mainly lies in the design of the USS. First is the flexibility of the mechanical system of the USS to generate linear and rotational motion. We chose servo motors, and used the wheel mode to generate linear motion and the joint mode to generate rotational motion. For the linear motion, we designed gearbox to maximize the angular velocity of the servo motor, and installed lead screws to convert the rotational motion to linear motion. For the rotational motion, we designed the spiral spring - damper to measure the angle of the coring tube. In addition, we integrated an electric solenoid to generate the hammering motion. The aggregate of these features permits a thorough investigation of sample quality with respect to desired sediment characteristics but is outside the scope of this dissertation.

Second is the pressure equalizing system. We used rubber bellows to waterproof the linear motion and the acrylic enclosure to waterproof the entire system of the USS. The inner volume of the enclosure is fixed, however, and when the USS is deploying the sampling coring tube, it changes the inner volume. Further, when the USS is launched underwater, the outer pressure of the enclosure increases as a function of the water depth as the USS is submerging. In response to the increasing pressure difference, the inner volume tries to expand. Since the rubber bellows consist of flexible material, they start deforming to increase the inner volume, which can result in an unplanned stoppage of linear motion. To maintain the shape of the rubber bellows, we must compensate for the volume change due to the pressure difference. We connected syringes to the inner volume of the USS to control the volume change due to the linear motion and pressure difference.

The third is waterproofing. We designed static and dynamic waterproofing methods to waterproof the USS. We installed acrylic enclosure to cover the main system of the USS, as well as rubber bellows to waterproof the linear motion, and a misaligned shaft O-ring to waterproof the rotational motion. Since we waterproofed the linear motion, the linear motion can cause the volume change inside of the enclosure, which causes the deformation of the rubber bellow. This issue can lower the speed of the linear motion or block it entirely. The pressure increases as the USS goes deeper. Due to the pressure difference between the inner and outer volume of the enclosure, we have to compensate for the pressure difference. Otherwise, it cause a deformation of rubber bellows which are made of the soft material. Therefore, we used large volume syringes as self-adjustable volume to compensate the volume change and prevent deformation of rubber bellows.

However, there are limitations to the design of the USS, and based on those, we can consider design improvements. First is the mechanical system of the USS to generate sampling patterns. We conducted a test of sediment sampling with the USS to evaluate and validate sampling patterns. Based on the results, we could consider different types of servo motors and a more advanced gearing system to expand the range of the sampling pattern. Also, we can consider the hammering motion's design to increase the impact force for more effective penetration.

Second is the design of the waterproofing and pressure equalization. We used rubber bellows to block the water coming inside the enclosure during linear motion. With this design, the inside of the enclosure is completely sealed. Thus, to generate the linear motion, the volume change is unavoidable and causes the deformation of rubber bellows. Also, when we deploy the USS underwater, the water pressure affects volume change on top of the volume change due to the linear motion. So, we installed syringes to equalize the pressure inside and outside the enclosure by compensating for the volume change. However, there is a limitation on the deploying depth. Volume compensation is unavoidable with the enclosure and rubber bellows to waterproof the USS. We could add as many syringes as possible, but this approach is inefficient. We have to consider a better way to waterproof the components of the USS to minimize the volume change and a more advanced pressure equalizing system.

6.1.2 Sediment Sampling Pattern

The optimal sampling pattern for a particular core sampling is a function of the type of sediments, the degree of overlying debris, the desired depth of the sample, and the desired sample quality. At the same time, there are engineering concerns for the functioning of the system that include reaction forces and ballast weight, and energy efficiency during sampling. For the preliminary engineering study, we used 20 patterns for Step 1 and 28 patterns for Step 2 based on three types of motions (linear, helix, and zig-zag) and three types of sediments (coarse sand, medium sand, and silt). For the sampling pattern analysis for the USS, we used 18 sampling patterns with one type of sediment (coarse sand) to find the effectiveness of hammering, rotational angle, and linear motion velocity. From the preliminary study, it was found the range of flexibility offered by the mechanism met engineering specifications and produced various results, validating design requirements. Furthermore, it was found in general that zig-zag motion showed the best performance in terms of the sample collected and work carried out. From the sampling pattern analysis for the USS, the sampling pattern with maximum linear velocity (6.5 mm/s), maximum rotating angle (120°), and hammering motion 'on' exhibited the lowest maximum reaction force acting on the coring tube during sampling and carried out the lowest amount of work.

Based on the sampling pattern analysis results, it can be assumed that the sediment is uniform with respect to depth. However, in real environments, the sediment type is not uniform, and its properties are not linear to the depth. Thus, more extensive sampling pattern tests based on different sediments to find the relationship between the sediment and sampling patterns is required by a soil scientist based on application needs. Ideally, we can derive the optimal sampling pattern consisting of multiple sampling patterns based on the extensive amount of data. In conclusion, the goals of this thesis for engineering analysis of sampling mechanism flexibility have been achieved, but a more thorough sampling pattern test exploring real-time strategies for optimizing sample quality and efficiency is left for other researchers and system adopters.

6.2 Field Experiments

During the extensive field experiments, it is vital to prepare for unexpected situations. To minimize these situations, we conducted indoor demonstrations many times until all steps of the system were processed smoothly. Despite all of the preparation, we were often faced with unpredictable situations in the field. To minimize those situations, we were required to increase the stability of the system. For example, for the hardware side of the system, we had to make sure that there are no issues in all joints of the mechanical components, and wiring harness. Moreover, we had to ensure that all sensors are working correctly. We tested all sensors in the field before we collected sensor data. In summary, establishing thorough checkpoints for field experiment preparation, and well-designed field experiment procedures can improve the quality of field experiments by minimizing the unexpected situations. We also faced expected situation such as lifting or toppling. If the terrain at the sampling area was adequately flat enough, the USS can be lifted instead of toppling or those can happen simultaneously depending on the contour of the terrain. Based on the field experiment result, the terrain was not ideally flat, so we could observe both lifting and toppling phenomenon.

We observed sample failure cases during the field experiments. We failed to sample the sediment from some trials and there are several reasons why we could not sample the sediment. First, the coring tube could not penetrate the sediment as shown in Fig. 6.1

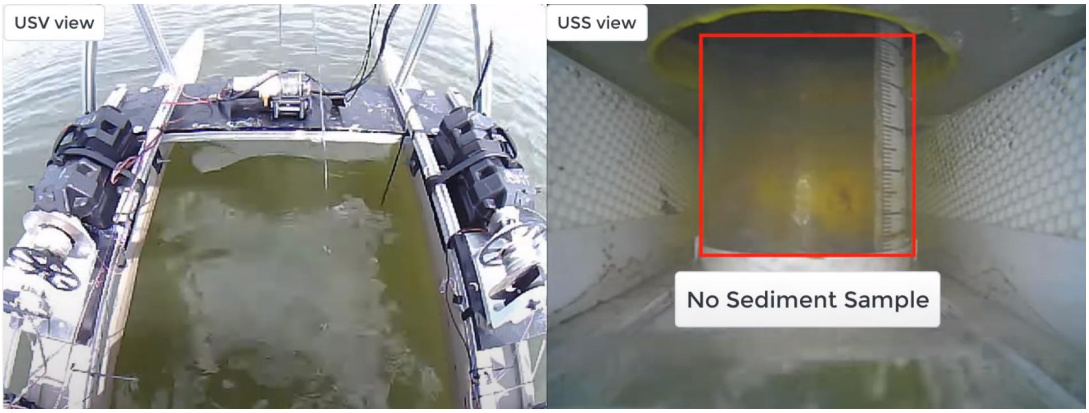

Figure 6.1. Sample failed: the coring tube could not penetrate the sediment.

and more details can be found in https://youtu.be/05SZiBrQB1A. We can suspect two scenarios: the complete lifting of the USS due to unexpected terrain such as hard rock and system failure. Sometimes, the system froze during operation. For example, the servo motor halted due to the heavy load. This depicts that the coring tube was not able to penetrate the sediment due to the hardness of the sediment. According to these experiences, we have to consider design a control system to prepare unexpected situations because of the unknown environment.

There were instances where we lost communication between the base station and the USV. Since the typical WiFi communication range is 100 m, we would lose connection to the USV if we deployed the USV beyond that limit. We can consider more advanced communication system such as using a directional antenna to increase the communication range and bandwidth [91]. Thrusters and anchor cables got tangled with heavy algae and vegetation growth in certain seasons, so the navigation capability of the USV was decreased. We considered design improvements and chose to install a protective cage to prevent tangling with vegetation or algae. There was also an instance where the USS and anchor cables got tangled together. This is the limitation of the current positioning system with anchors. We could consider adopting a dynamic positioning system for the positioning system of the USV [92], [93] but that is less amenable to the types of geographically-constrained freshwater bodies we are targeting (particularly rivers and canals).

6.2.1 Lifting and Toppling

The lifting phenomenon is dependent on the total negative buoyancy of the USS and the reaction force during the penetration and is highly dependent on the materials and potential debris at the chosen sampling site. If the reaction force increases beyond the negative buoyancy of the USS, the USS starts lifting and it can cause the toppling at the same time depending on the contour of the terrain and the support polygon of the sampler. This is critical because it is directly related to the recovery ratio, especially the actual penetration depth (H). If lifting and toppling occurs, as the penetration depth decreases, the core's length (h) decreases resulting in a reduction in the sample volume. This issue can be resolved by

increasing the negative buoyancy of the USS or by relocating the sampler to a new sampling site. Negative buoyancy can be achieved for the USS by adding more weight on top of the USS's weight. From previous trial, we observed the lifting phenomenon, and the additional weight of the USS was 20 kg. The lifting height was approximately 15 cm as shown in Fig. 6.2(a). We add extra 10 kg on the USS to increase the weight of the USS. According to the weight increase we could reduce the height of the lifting to approximately 10 cm as shown in Fig. 6.2(b). We can estimate the maximum reaction force via a statistical approach based on the data. Once we estimate the maximum reaction force, we can calculate how much more weight is required. Currently, the USS can easily attach or detach the weights to control the negative buoyancy.

Based on experiences, we must consider adding reaction force and orientation data monitoring system to the GUI of the system. Thus, the user can determine the sampling performance based on the real-time data and prevent sampling failure. For example, if the USS moves in the sampling impossible region based on the threshold of lifting and toppling of the USS, the user can decide to retrieve the USS. Also, we can consider the ultimate method. For example, we can develop an anchoring system for the USS by integrating an auger drill system to each leg of the USS.

6.3 Autonomous Sediment Sampling System

The development of the autonomous system is important for constructing more effective environmental monitoring systems by obtaining a real-time system. The autonomous sediment sampling system is necessary to establish more advanced sediment monitoring systems based on more frequent sediment sampling and to provide an instrument for the detailed study of sediment sampling quality.

An autonomous sediment sampling system has the potential to expand even further. Integrating autonomy is not applicable to just unmanned systems; instead, it can be integrated to the entire system by introducing the cyber-physical system (CPS) [94][95][96][97] and cloud computing [98][99][100]. We can deploy multiple autonomous sediment sampling systems to the target environment and collect massive amounts of data simultaneously. Af-

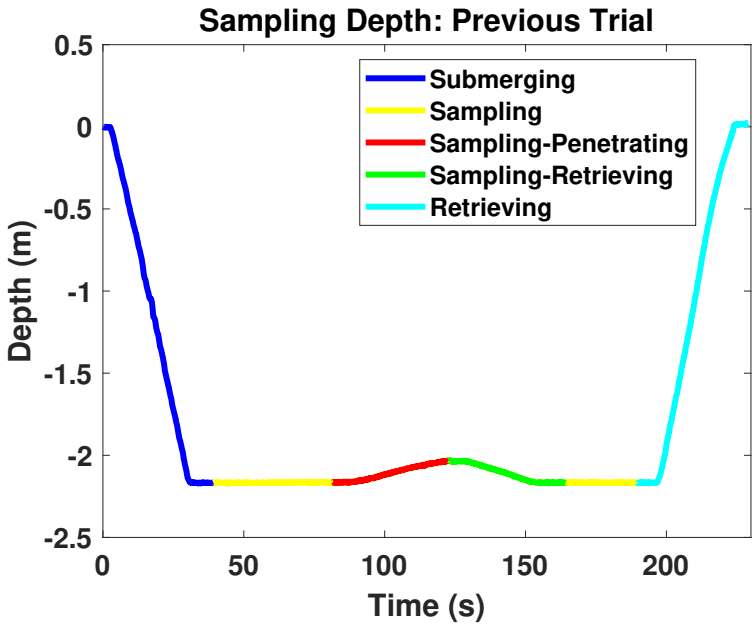

(a)

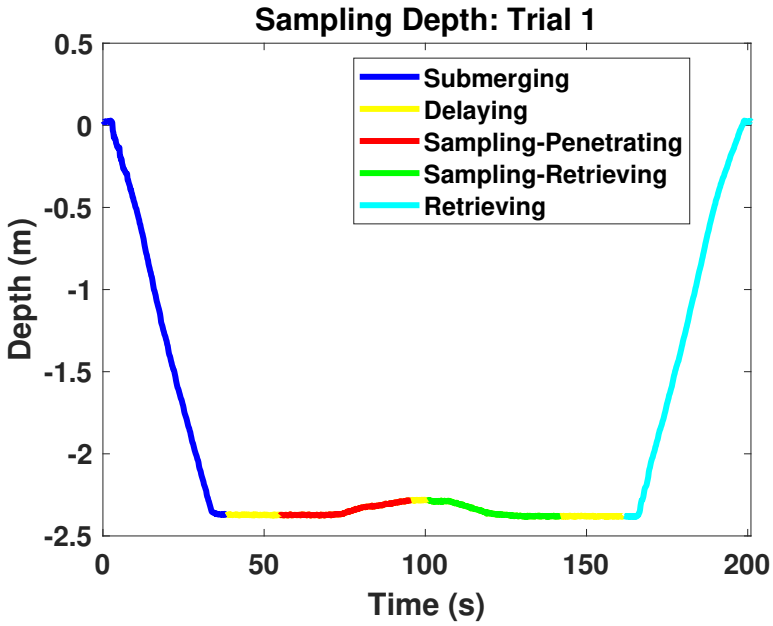

(b)

Figure 6.2. Sampling depth of the USS: (a) When the additional weight of the USS was 20 kg (Previous Trial), the lifting height was about 15 cm, and (b) When the additional weight of the USS was 30 kg (Trial 1), the lifting height was about 10 cm.

terward, we can transmit the data to the cloud for storage. We can also establish a real-time computing system to analyze the data and predict the solution as a control input of the system. By developing this concept, we can establish an autonomous environmental monitoring system to preserve and restore nature.

7. CONCLUSION

In this research, we designed and developed an uncrewed sediment sampling system to collect sediment samples more effectively and with the ability to comprehensively study sample quality from surface-water environments. We also defined the challenges of sampling the sediment underwater and considered those when designing the system. Furthermore, we developed a USV to carry the USS to the desired sampling area and maintain its position while the USS samples the sediment. We also applied submersible designs, such as negative buoyancy, waterproofing, and pressure equalizing to launch the USS successfully on the sediment bed and sample the sediment successfully in underwater conditions. We integrated sampling patterns based on the preliminary study about sediment sampling to reduce the reaction force and minimize the disturbance during the sampling process. Furthermore, we explained the relationship between the reaction force and sampling patterns mathematically.

To evaluate mechanisms generating the sampling patterns, we conducted indoor tests and collected the reaction force and energy data. Based on this, we could analyze the effectiveness of the hammering motion, effectiveness of the rotation range, and linear motion velocity. Moreover, we conducted field experiments to evaluate the system from an engineering perspective. We defined tasks to evaluate the performance of the system and collected GPS data to check the performance of USV deploying and positioning systems. The depth data showed the depth change of the USS during submerging, sampling, and retrieving. During the sampling state, we plotted the depth data while the coring tube was penetrating and retrieving the sediment. Notably, the USS was lifted during penetration. The IMU data showed the orientation of the USS while it was submerging, sampling, and retrieving. The orientation change of the USS was not significant compared to the lifting. We also measured the reaction forces acting on the coring tube while sampling. We then observed the lifting and toppling, and calculated the work carried out to find the energy required to penetrate the sediment based on the reaction force data.

Based on the development process and the results of the field experiments, we realized the limitations and potential approaches of the uncrewed sediment sampling system. For the limitations of current system, we can improve the mechanical system for generating sediment

sampling patterns to cover wider environment. We can consider improving the waterproofing and pressure equalizing system to expand the deploying depth of the USS. While this dissertation's goal is not to fully evaluate sediment sample quality, the engineering capabilities that allow a full and thorough examination by qualified soil scientists have been verified, and the desired preliminary validation confirmed. From the field experiments, we observed system limitations in sampling and communication that would benefit from a taxonomy of waterbed materials and conditions beyond this dissertation's scope. The biggest challenge was 'How we can prevent lifting and toppling of the USS during penetration to increase the quality and quantity of the sediment sample at the location specified by the soil scientist. The current solution is to simply abort, re-position the unit to a new sample location specified by the soil scientist.'

The strengths of the proposed system include field adaptability and applicability. Since this system consists of the multi-robot team and it is covering both surface water and underwater, it can be actively used not only for sediment sampling but also for other functions such as water sampling and various sensor and collection of various mobile sensor data. Thus, this system can have many potential elements that can be a total solution for autonomous environmental monitoring. Specifically, by adding the water sampling system to the USS, we can collect water samples even from the different depth even from varying depths. It is designed to adapt to sites that require sediment sampling, and more information can be obtained by implementing various types of sensors, such as a pH, turbidity, total organic carbon (TOC), conductivity, residual chlorine, or oxygen-reduction potential senor to the USV and USS for collect various types of data both from surface water and underwater. Also, we can install sensors for bathymetry mapping such as sonar or acoustic doppler. Furthermore, based on these approaches, this system can be upgraded to an autonomous environmental monitoring system. For example, this system can automatically deploy the USV and USS to the points of interest and collect the sediment samples. An uncrewed sediment sampling system is the first step to establish a more advanced environmental monitoring system. This study is a pioneering work in this field, contributing to the development of an autonomous environmental monitoring system from above the water surface through the water column and into the sediments at the floor to preserve and protect our natural resources.

REFERENCES

[1] I. S. I. ISI, *Sediment issues & sediment management in large river basins; interim case study synthesis report*, 2011.

[2] A. J. Sekellick, W. S. Banks, and M. K. Myers, "Water volume and sediment volume and density in Lake Linganore between Boyers Mill Road Bridge and Bens Branch, Frederick County, Maryland, 2012," Reston, VA, Tech. Rep., 2013, p. 26.

[3] L. F. B. Chief, "Sediment sampling operating procedure," *Region 4, U.S. Environmental Protection Agency, Laboratory Services and Applied Science Division, Athens, Georgia*, 2020.

[4] H. J. Timothy Simpson John Deatrick, "Field sampling quality control," *Region 4, U.S. Environmental Protection Agency, Laboratory Services and Applied Science Division, Athens, Georgia*, 2017.

[5] L. R. 9. LABORATORY, "Field sampling guidance document 1215," *U.S.EPA REGION 9 LABORATORY, RICHMOND, CALIFORNIA*,

[6] R. Awal, P. Sapkota, S. Chitrakar, B. Thapa, H. Neopane, and B. Thapa, "A general review on methods of sediment sampling and mineral content analysis," in *Journal of Physics: Conference Series*, IOP Publishing, vol. 1266, 2019, p. 012 005.

[7] R. S. V. H. S. S. SINGHAL G. C. JOSHI, "Sediment sampling in rivers and canals," *Erosion and Sediment Transport Measurement (Proceedings of the Florence Symposium)*, no. 133, pp. 169–175, 1981.

[8] S. Cieniawski, "A guidance manual to support the assessment of contaminated sediments in freshwater ecosystems," 2002.

[9] C. Paull, S. Stratton, M. Conway, K. Brekke, T. C. Dawe, N. Maher, and W. Ussler, "Deep sea vibracoring system improves ROV sampling capability," en, *Eos, Transactions American Geophysical Union*, vol. 82, no. 30, pp. 325–326, Jul. 2001, ISSN: 2324-9250.

[10] H. Yoshida, T. Aoki, H. Osawa, T. Miyazaki, J. Tahara, S. Ishibashi, H. Ochi, Y. Watanabe, and M. Mizuno, "The Two-Stage ROV for Sediment Sampling on Mariana Trench," in *OCEANS 2006 - Asia Pacific*, May 2006, pp. 1–4.

[11] H. Yoshida, T. Aoki, H. Osawa, S. Ishibashi, Y. Watanabe, J. Tahara, T. Miyazaki, and K. Itoh, "A Deepest Depth ROV for Sediment Sampling and Its Sea Trial Result," in *2007 Symposium on Underwater Technology and Workshop on Scientific Use of Submarine Cables and Related Technologies*, Apr. 2007, pp. 28–33.

[12] L. L. Whitcomb, M. V. Jakuba, J. C. Kinsey, S. C. Martin, S. E. Webster, J. C. Howland, C. L. Taylor, D. Gomez-Ibanez, and D. R. Yoerger, "Navigation and control of the Nereus hybrid underwater vehicle for global ocean science to 10,903 m depth: Preliminary results," in *2010 IEEE International Conference on Robotics and Automation*, May 2010, pp. 594–600.

[13] D. Sathianarayanan, R. Ramesh, A. N. Subramanian, G. Harikrishnan, D. Muthukumaran, M. Murugesan, E. Chandresekaran, S. Elangovan, V. D. Prakash, A. Vadivelan, M. Radhakrishnan, S. Ramesh, G. A. Ramadass, M. A. Atmanand, S. Sukonkin, and A. Alexey, "Deep sea qualification of remotely operable vehicle (ROSUB 6000)," in *2013 IEEE International Underwater Technology Symposium (UT)*, Mar. 2013, pp. 1–7.

[14] P. Gao, B. Zheng, J. Liang, C. Ren, G. Gao, L. Zhou, L. Shao, C. Chen, Q. Wang, J. Shen, *et al.*, "Development of an underwater robot for sediment soil sampling," in *2015 3rd International Conference on Mechatronics and Industrial Informatics (ICMII 2015)*, Atlantis Press, 2015.

[15] N. Sakagami, S. Sasaki, M. Kawabata, K. Yokoi, S. Matsuda, A. Mitsui, K. Sano, K. Tago, and S. Kawamura, "Development of a human-portable underwater robot for soil core sampling," in *2013 MTS/IEEE OCEANS - Bergen*, Jun. 2013, pp. 1–6.

[16] K. Yokoi, M. Kawabata, S. Sakai, S. Kawamura, N. Sakagami, S. Matsuda, A. Mitsui, and K. Sano, "Improvement of a human-portable underwater robot for soil core sampling," in *2014 Oceans - St. John's*, Sep. 2014, pp. 1–6.

[17] "Human-based sediment sampling," [Online]. Available: https://i.ytimg.com/vi/vD0pQsg3NdA/maxresdefault.jpg.

[18] "Sediment sampling from the boat," [Online]. Available: https://lh3.googleusercontent.com/proxy/G7SJYp-JaNzYsIVBiYz4in7lXeYfSa9-TeET8T2UtlTWcXAzVFBa4nkrniX-3Q3myb79_i2GQ_5NsgDg0G-QcoLXmuPpIgepXH2cEk9-oMqNNyi-Nx2C.

[19] S. J. Carr, L. M. Diggens, and K. L. Spencer, "There is no such thing as 'undisturbed'soil and sediment sampling: Sampler-induced deformation of salt marsh sediments revealed by 3d x-ray computed tomography," *Journal of Soils and Sediments*, vol. 20, pp. 2960–2976, 2020.

[20] S. Dutta, D. Sarma, and P. Nath, "Ground and river water quality monitoring using a smartphone-based ph sensor," *Aip Advances*, vol. 5, no. 5, p. 057 151, 2015.

[21] L. Parra, J. Rocher, J. Escrivá, and J. Lloret, "Design and development of low cost smart turbidity sensor for water quality monitoring in fish farms," *Aquacultural Engineering*, vol. 81, pp. 10–18, 2018.

[22] Y. Wang, S. S. M. Rajib, C. Collins, and B. Grieve, "Low-cost turbidity sensor for low-power wireless monitoring of fresh-water courses," *IEEE Sensors Journal*, vol. 18, no. 11, pp. 4689–4696, 2018.

[23] A. A. Azman, M. H. F. Rahiman, M. N. Taib, N. H. Sidek, I. A. A. Bakar, and M. F. Ali, "A low cost nephelometric turbidity sensor for continual domestic water quality monitoring system," in *2016 IEEE International Conference on Automatic Control and Intelligent Systems (I2CACIS)*, IEEE, 2016, pp. 202–207.

[24] Y. Mulyana and D. Hakim, "Prototype of water turbidity monitoring system," in *IOP Conference Series: Materials Science and Engineering*, IOP Publishing, vol. 384, 2018, p. 012 052.

[25] N.-B. Chang, B. W. Vannah, Y. J. Yang, and M. Elovitz, "Integrated data fusion and mining techniques for monitoring total organic carbon concentrations in a lake," *International Journal of Remote Sensing*, vol. 35, no. 3, pp. 1064–1093, 2014.

[26] J. Raich, "Review of sensors to monitor water quality," *European reference network for critical infrastructure protection (ERNCIP) project*, 2013.

[27] P. M. Ramos, J. D. Pereira, H. M. G. Ramos, and A. L. Ribeiro, "A four-terminal water-quality-monitoring conductivity sensor," *IEEE Transactions on Instrumentation and Measurement*, vol. 57, no. 3, pp. 577–583, 2008.

[28] L. Parra, S. Sendra, J. Lloret, and I. Bosch, "Development of a conductivity sensor for monitoring groundwater resources to optimize water management in smart city environments," *Sensors*, vol. 15, no. 9, pp. 20 990–21 015, 2015.

[29] L. H.-H. Hsu, A. Aryasomayajula, and P. R. Selvaganapathy, "A review of sensing systems and their need for environmental water monitoring," *Critical Reviews™ in Biomedical Engineering*, vol. 44, no. 5, 2016.

[30] L. Hsu, P. R. Selvaganapathy, J. Brash, Q. Fang, C.-Q. Xu, M. J. Deen, and H. Chen, "Development of a low-cost hemin-based dissolved oxygen sensor with anti-biofouling coating for water monitoring," *IEEE Sensors Journal*, vol. 14, no. 10, pp. 3400–3407, 2014.

[31] J. E. Manley, "Unmanned surface vehicles, 15 years of development," in *OCEANS 2008*, Ieee, 2008, pp. 1–4.

[32] J. Jin, J. Zhang, Y. Ma, and S. GUAN, "An unmanned surface vehicle for bathymetry," *Hydrographic Surveying and Charting*, vol. 33, no. 2, pp. 53–56, 2013.

[33] A. Mancini, E. Frontoni, and P. Zingaretti, "Development of a low-cost unmanned surface vehicle for digital survey," in *2015 European Conference on Mobile Robots (ECMR)*, IEEE, 2015, pp. 1–6.

[34] M. L. Seto and A. Crawford, "Autonomous shallow water bathymetric measurements for environmental assessment and safe navigation using usvs," in *OCEANS 2015-MTS/IEEE Washington*, IEEE, 2015, pp. 1–5.

[35] H. Ferreira, C. Almeida, A. Martins, J. Almeida, N. Dias, A. Dias, and E. Silva, "Autonomous bathymetry for risk assessment with roaz robotic surface vehicle," in *Oceans 2009-Europe*, Ieee, 2009, pp. 1–6.

[36] R. Dinehart and J. Burau, "Repeated surveys by acoustic doppler current profiler for flow and sediment dynamics in a tidal river," *Journal of hydrology*, vol. 314, no. 1-4, pp. 1–21, 2005.

[37] H. Francis and P. Traykovski, "Development of a highly portable unmanned surface vehicle for surf zone bathymetric surveying," *Journal of Coastal Research*, 2021.

[38] J. Yuh, "Development in underwater robotics," in *Proceedings of 1995 IEEE International Conference on Robotics and Automation*, vol. 2, May 1995, 1862–1867 vol.2.

[39] J. Yuh and M. West, "Underwater robotics," *Advanced Robotics*, vol. 15, no. 5, pp. 609–639, Jan. 2001, ISSN: 0169-1864.

[40] G. Antonelli, T. I. Fossen, and D. R. Yoerger, "Underwater Robotics," en, in *Springer Handbook of Robotics*, B. S. Prof and O. K. Prof, Eds., Springer Berlin Heidelberg, 2008, pp. 987–1008.

[41] G. Antonelli, "1. Introduction," en, in *Underwater Robots – 2nd Edition*, ser. Springer Tracts in Advanced Robotics 2, DOI: 10.1007/11540199_1, Springer Berlin Heidelberg, 2006, pp. 1–13.

[42] L. L. Whitcomb, "Underwater robotics: Out of the research laboratory and into the field," in *Proceedings 2000 ICRA. Millennium Conference. IEEE International Conference on Robotics and Automation. Symposia Proceedings (Cat. No.00CH37065)*, vol. 1, 2000, 709–716 vol.1.

[43] "Jason 2 (whoi)," [Online]. Available: https://oria.ceoe.udel.edu/files/2012/10/Jason-from-WHOI.jpg.

[44] "Bluefin-12d," [Online]. Available: https://auvac.org/files/uploads/configuration/bluefin-12d-recovery.jpg.

[45] J. Yuh, S. K. Choi, C. Ikehara, G. H. Kim, G. McMurty, M. Ghasemi-Nejhad, N. Sarkar, and K. Sugihara, "Design of a semi-autonomous underwater vehicle for intervention missions (SAUVIM)," in *Proceedings of 1998 International Symposium on Underwater Technology*, Apr. 1998, pp. 63–68.

[46] J. Evans, P. Redmond, C. Plakas, K. Hamilton, and D. Lane, "Autonomous docking for Intervention-AUVs using sonar and video-based real-time 3d pose estimation," in *Oceans 2003. Celebrating the Past ... Teaming Toward the Future (IEEE Cat. No.03CH37492)*, vol. 4, Sep. 2003, 2201–2210 Vol.4.

[47] V. Bertram, "Unmanned surface vehicles-a survey," *Skibsteknisk Selskab, Copenhagen, Denmark*, vol. 1, pp. 1–14, 2008.

[48] M. Caccia, M. Bibuli, R. Bono, and G. Bruzzone, "Basic navigation, guidance and control of an Unmanned Surface Vehicle," en, *Autonomous Robots*, vol. 25, no. 4, pp. 349–365, Nov. 2008, ISSN: 0929-5593, 1573-7527.

[49] C. R. Sonnenburg and C. A. Woolsey, "Modeling, Identification, and Control of an Unmanned Surface Vehicle," en, *Journal of Field Robotics*, vol. 30, no. 3, pp. 371–398, May 2013, ISSN: 1556-4967.

[50] A. Valada, P. Velagapudi, B. Kannan, C. Tomaszewski, G. Kantor, and P. Scerri, "Development of a Low Cost Multi-Robot Autonomous Marine Surface Platform," en, in *Field and Service Robotics*, ser. Springer Tracts in Advanced Robotics 92, K. Yoshida and S. Tadokoro, Eds., DOI: 10.1007/978-3-642-40686-7_43, Springer Berlin Heidelberg, 2014, pp. 643–658.

[51] "Protector usv (navy)," [Online]. Available: https://www.defencetalk.com/wp-content/uploads/2012/01/Protector-Umanned-Surface-Vessel-rafael.jpg.

[52] "Catarob-ats-03," [Online]. Available: https://geo-matching.com/uploads/default/m/i/migrationu0csri.jpg.

[53] B. Colby, "Fluvial sediments a summary of source, transportation, deposition, and measurement of sediment discharge," U. S. Govt. Print. Off., USGS Numbered Series 1181-A, 1963. [Online]. Available: http://pubs.er.usgs.gov/publication/b1181A.

[54] "Grab sampler," [Online]. Available: https://www.iopan.gda.pl/projects/biodaff/picVVeen.jpg.

[55] "Core sampler," [Online]. Available: https://lh3.googleusercontent.com/proxy/28YmwKG_ClghvxGHrkgYY4-8osdo7F-iUBj2pTcP35fIrNHTk2LuiBExhUei9B_HoZZyP1BYLPPBd_kYtmNoc-Za-NRULBsM9q-rtFumzIkA-hK4jsdPnhzOyG5YNU9SdUcaZ-exQ-2kWnnofXarqU79T_94Xg.

[56] O. US EPA, *Methods for Collection, Storage and Manipulation of Sediments for Chemical and Toxicological Analyses*, en, Data and Tools, 2017. [Online]. Available: https://www.epa.gov/ocean-dumping/methods-collection-storage-and-%20%5C%5C%20manipulation-sediments-chemical-and-toxicological.

[57] J. Kasich, M. Taylor, and S. Nally, "Sediment sampling guide and methodologies," *Ohio Environmental Protection Agency*, 2012.

[58] L. R. Shelton and P. D. Capel, "Guidelines for collecting and processing samples of stream bed sediment for analysis of trace elements and organic contaminants for the national water-quality assessment program," US Geological Survey; USGS Earth Science Information Center, Open-File …, Tech. Rep., 1994.

[59] "Lake and stream bottom sediment sampling manual," English, 1997. [Online]. Available: http://agris.fao.org/agris-search/search.do?recordID=US201300039603.

[60] IAEA, "Collection and Preparation of Bottom Sediment Samples for Analysis of Radionuclides and Trace Elements," English, 2003.

[61] ASTM, "Standard Guide for Core Sampling Submerged, Unconsolidated Sediments," Tech. Rep., 2014.

[62] C. G. Skilbeck, S. Trevathan-Tackett, P. Apichanangkool, and P. I. Macreadie, "Sediment Sampling in Estuaries: Site Selection and Sampling Techniques," en, in *Applications of Paleoenvironmental Techniques in Estuarine Studies*, ser. Developments in Paleoenvironmental Research, Springer, Dordrecht, 2017, pp. 89–120, ISBN: 9789402409888 9789402409901.

[63] O. US EPA, *Methods for Collection, Storage and Manipulation of Sediments for Chemical and Toxicological Analyses*, en, Data and Tools, Aug. 2015.

[64] M. F. Horne, "Drilling on Mars – Mathematical Model for Rotary-Ultrasonic Core Drilling of Brittle Materials," en, Ph.D. dissertation, UC Berkeley, 2015.

[65] X. Shi, Z. Deng, Q. Quan, D. Tang, X. Hou, and S. Jiang, "Development of a drilling and coring test-bed for lunar subsurface exploration and preliminary experiments," en, *Chinese Journal of Mechanical Engineering*, vol. 27, no. 4, pp. 673–682, Jul. 2014.

[66] Y. Tian, D. Tang, Z. Deng, S. Jiang, and Q. Quan, "Drilling power consumption and soil conveying volume performances of lunar sampling auger," en, *Chinese Journal of Mechanical Engineering*, vol. 28, no. 3, pp. 451–459, May 2015.

[67] Q. Quan, J. Tang, F. Yuan, S. Jiang, and Z. Deng, "Drilling load modeling and validation based on the filling rate of auger flute in planetary sampling," *Chinese Journal of Aeronautics*, vol. 30, no. 1, pp. 434–446, Feb. 2017.

[68] Tian Ye, Deng Zong-Quan, Tang De-Wei, and Chen Jing-Kai, "Drilling Power Consumption Analysis of Coring Bit in Lunar Sample Mission," *Journal of Aerospace Engineering*, vol. 30, no. 5, p. 04 017 055, Sep. 2017.

[69] T. Zhang and X. Ding, "Drilling forces model for lunar regolith exploration and experimental validation," *Acta Astronautica*, vol. 131, pp. 190–203, Feb. 2017.

[70] K. Zacny, A. Avanesyan, G. Paulsen, J. Craft, P. Chu, and T. Szwarc, "Mars drill for the Mars sample return mission with a Brushing and Abrading bit, regolith and powder bit, core PreView Bit and a coring bit," in *2012 IEEE Aerospace Conference*, Mar. 2012, pp. 1–8.

[71] J. A. Escudero, J. A. Ramírez-Macías, J. C. Correa, and D. Rozo, "Experimental Study of Push Coring Forces During Sediment Extraction Using a Robot Manipulator," V009T10A021, Jun. 2017.

[72] Y. T. Tseng, J. J. Ding, and C. S. Liu, "Analysis of attenuation measurements in ocean sediments using normal incidence chirp sonar," *IEEE Journal of Oceanic Engineering*, vol. 37, no. 3, pp. 533–543, Jul. 2012, ISSN: 0364-9059. DOI: 10.1109/JOE.2012.2200377.

[73] R. A. Wheatcroft, A. W. Stevens, and R. V. Johnson, "In situ time-series measurements of subseafloor sediment properties," *IEEE Journal of Oceanic Engineering*, vol. 32, no. 4, pp. 862–871, Oct. 2007, ISSN: 0364-9059. DOI: 10.1109/JOE.2007.907927.

[74] K. Kitada, E. Araki, T. Kimura, Y. Mizuguchi, M. Kyo, T. Saruhashi, I. Sawada, Y. Namba, and M. Kinoshita, "Field experimental study on vortex-induced vibration behavior of the drill pipe for the ocean borehole observatory installation," *IEEE Journal of Oceanic Engineering*, vol. 38, no. 1, pp. 158–166, Jan. 2013, ISSN: 0364-9059. DOI: 10.1109/JOE.2012.2213973.

[75] J. T. Hatleskog and M. W. Dunnigan, "Passive compensator load variation for deep-water drilling," *IEEE Journal of Oceanic Engineering*, vol. 32, no. 3, pp. 593–602, Jul. 2007, ISSN: 0364-9059. DOI: 10.1109/JOE.2007.895276.

[76] P. Deusdado, M. Guedes, A. Silva, F. Marques, E. Pinto, P. Rodrigues, A. Lourenço, R. Mendonça, P. Santana, J. Corisco, S. M. Almeida, L. Portugal, R. Caldeira, J. Barata, and L. Flores, "Sediment Sampling in Estuarine Mudflats with an Aerial-Ground Robotic Team," en, *Sensors*, vol. 16, no. 9, p. 1461, Sep. 2016.

[77] J. H. Bae, J. H. Park, S. Lee, and B.-C. Min, "Tri-SedimentBot: An underwater sediment sampling robot," in *2016 IEEE International Conference on Automation Science and Engineering (CASE)*, Aug. 2016.

[78] S. J. Blott and K. Pye, "GRADISTAT: A grain size distribution and statistics package for the analysis of unconsolidated sediments," en, *Earth Surface Processes and Landforms*, vol. 26, no. 11, pp. 1237–1248, Oct. 2001, ISSN: 1096-9837.

[79] S. J. Blott and K. Pye, "Particle size scales and classification of sediment types based on particle size distributions: Review and recommended procedures," en, *Sedimentology*, vol. 59, no. 7, pp. 2071–2096, Dec. 2012, ISSN: 1365-3091.

[80] P. Ngatchou, A. Zarei, and A. El-Sharkawi, "Pareto Multi Objective Optimization," in *Proceedings of the 13th International Conference on, Intelligent Systems Application to Power Systems*, Nov. 2005, pp. 84–91.

[81] G. Vanderplaats, "Multi-Objective Optimization," in *Multidiscipline Design Optimization*, First edition, Monterey, CA: Vanderplaats R&D, Inc, 2007, pp. 294–301, ISBN: 0-944956-04-1.

[82] L. M. Moore, *The basic practice of statistics*, 1996.

[83] M. H. Kutner, *Applied linear statistical models*, eng, 5th edition.., ser. McGraw-Hill/Irwin series operations and decision sciences. McGraw-Hill Irwin, 2005, ISBN: 0072386886.

[84] R. T. Marler and J. S. Arora, "The weighted sum method for multi-objective optimization: New insights," en, *Structural and Multidisciplinary Optimization*, vol. 41, no. 6, pp. 853–862, Jun. 2010, ISSN: 1615-147X, 1615-1488.

[85] A. Lavin, "A pareto front-based multiobjective path planning algorithm," *arXiv preprint arXiv:1505.05947*, 2015.

[86] S. Dai and J. C. Santamarina, "Sampling disturbance in hydrate-bearing sediment pressure cores: NGHP-01 expedition, Krishna godavari Basin example," *Marine and Petroleum Geology*, vol. 58, pp. 178–186, Dec. 2014.

[87] A. O. M. Mogg, K. M. Attard, H. Stahl, T. Brand, R. Turnewitsch, and M. D. J. Sayer, "The influence of coring method on the preservation of sedimentary and biogeochemical features when sampling soft-bottom, shallow coastal environments," *Limnology and Oceanography: Methods*, vol. 15, pp. 905–915, 2017.

[88] S. Sharma, W. Naeem, and R. Sutton, "An autopilot based on a local control network design for an unmanned surface vehicle," *Journal of Navigation*, vol. 65, no. 2, pp. 281–301, 2012, ISSN: 0373-4633.

[89] C. Li, J. Jiang, F. Duan, W. Liu, X. Wang, L. Bu, Z. Sun, and G. Yang, "Modeling and experimental testing of an unmanned surface vehicle with rudderless double thrusters," *Sensors*, vol. 19, no. 9, 2019, ISSN: 1424-8220.

[90] K. Rocker Jr, "Handbook for marine geotechnical engineering. deep ocean technology," *Final Report, Oct. 1979-Dec. 1983 Naval Civil Engineering Lab., Port Hueneme, CA.*, 1985.

[91] B.-C. Min, E. T. Matson, and J.-W. Jung, "Active antenna tracking system with directional antennas for enhancing wireless communication capabilities of a networked robotic system," *Journal of Field Robotics*, vol. 33, no. 3, pp. 391–406, 2016.

[92] H. Halvorsen, "Dynamic positioning for unmanned surface vehicles," M.S. thesis, Institutt for teknisk kybernetikk, 2008.

[93] N.-H. Tran, H.-S. Choi, J.-Y. Oh, and S.-K. Jeong, "Design and implementation of dynamic positioning control system for usv," in *AETA 2015: Recent Advances in Electrical Engineering and Related Sciences*, Springer, 2016, pp. 633–644.

[94] M. Iqbal and H. B. Lim, "A Cyber-physical Middleware Framework for Continuous Monitoring of Water Distribution Systems," in *Proceedings of the 7th ACM Conference on Embedded Networked Sensor Systems*, ser. SenSys '09, New York, NY, USA: ACM, 2009, pp. 401–402.

[95] A. Nasir, B. H. Soong, and S. Ramachandran, "Framework of WSN based human centric cyber physical in-pipe water monitoring system," in *2010 11th International Conference on Control Automation Robotics Vision*, Dec. 2010, pp. 1257–1261.

[96] D. Li, Z. Zhao, L. Cui, H. Zhu, L. Zhang, Z. Zhang, and Y. Wang, "A cyber physical networking system for monitoring and cleaning up blue-green algae blooms with agile sensor and actuator control mechanism on Lake Tai," in *2011 IEEE Conference on Computer Communications Workshops (INFOCOM WKSHPS)*, Apr. 2011, pp. 732–737.

[97] Z. Wang, H. Song, D. W. Watkins, K. G. Ong, P. Xue, Q. Yang, and X. Shi, "Cyber-physical systems for water sustainability: Challenges and opportunities," *IEEE Communications Magazine*, vol. 53, no. 5, pp. 216–222, May 2015, ISSN: 0163-6804.

[98] A. A. Cardenas, S. Amin, and S. Sastry, "Secure Control: Towards Survivable Cyber-Physical Systems," in *2008 The 28th International Conference on Distributed Computing Systems Workshops*, Jun. 2008, pp. 495–500.

[99] G. Mois, T. Sanislav, and S. C. Folea, "A Cyber-Physical System for Environmental Monitoring," *IEEE Transactions on Instrumentation and Measurement*, vol. 65, no. 6, pp. 1463–1471, Jun. 2016.

[100] T. Sanislav, G. Mois, S. Folea, L. Miclea, G. Gambardella, and P. Prinetto, "A cloud-based Cyber-Physical System for environmental monitoring," in *2014 3rd Mediterranean Conference on Embedded Computing (MECO)*, Jun. 2014, pp. 6–9.

A. APPENDIX

No	**Description**	**Link**
1	A video on the evaluation of sampling methods for robotic sediment sampling systems: a preliminary study proposed in Chapter 3.	https://youtu.be/W8gBe9SDXNw
2	A video on the development of an uncrewed surface vehicle for remote sediment sampling with a Van Veen grab sampler proposed in Chapter 4.	https://youtu.be/YwTirVChu7g
3	A video on the sampling pattern test for the uncrewed sediment sampling system proposed in Chapter 4.	https://youtu.be/Gq8vrngBsWE
4	A video on the field experiment for the uncrewed sediment sampling system for surface water sediment collection proposed in Chapter 4.	https://youtu.be/hyOpj9d6nxI
5	A video on the field experiment for the uncrewed sediment sampling system: Example of a sample failure case proposed in Chapter 6.	https://youtu.be/05SZiBrQB1A

VITA

Jun Han Bae was born in Seoul, Republic of Korea, in 1985. He received the B.S. degree in Mechanical Engineering from Yonsei University, Republic of Korea, in 2010, and the M.S. degree in School of Engineering Technology from Purdue University in 2014. He worked at the mechanical design division in STX Offshore & Shipbuilding CO. for two years (2010-2012). He is currently pursuing his Ph.D. in Technology with a specialization in Robotics at Purdue University in West Lafayette, USA. His research interests span the areas of mechanical design in robotics, intelligent robotics modeling and control, and underwater robotics.

Referred Publications

- **Jun Han Bae**, Wonse Jo, Jee Hwan Park, Richard M. Voyles, Sara K. McMillan, and Byung-Cheol Min, "Evaluation of Sampling Methods for Robotic Sediment Sampling Systems", *IEEE Journal of Oceanic Engineering,* 2020.

- **Jun Han Bae**, Shaocheng Luo, Shyam Sundar Kannan, Yogang Singh, Bumjoo Lee, Richard M. Voyles, Mauricio Postigo-Malaga, Edgar Gonzales Zenteno, Lizbeth Paredes Aguilar, and Byung-Cheol Min, "Development of an Unmanned Surface Vehicle for Remote Sediment Sampling with a Van Veen Grab Sampler", 2019 MTS/IEEE OCEANS, Seattle, WA, USA, October 27-31, 2019.

- Shaocheng Luo, Yogang Singh, Hanyao Yang, **Jun Han Bae**, J. Eric Dietz, Xiumin Diao, and Byung-Cheol Min, "Image Processing and Model-Based Spill Coverage Path Planning for Unmanned Surface Vehicles", 2019 MTS/IEEE OCEANS, Seattle, WA, USA, October 27-31, 2019.

- Shaocheng Luo, Jonghoek Kim, Ramviyas Parasuraman, **Jun Han Bae**, Eric T Matson, and Byung-Cheol Min, "Multi-robot Rendezvous Based on Bearing-aided Hierarchical Tracking of Network Topology", *Ad Hoc Networks,* 2018.

- Shaocheng Luo, **Jun Han Bae**, and Byung-Cheol Min, "Pivot-based Collective Coverage Control with a Multi-robot Team", *2018 IEEE International Conference*

on Robotics and Biomimetics (IEEE ROBIO 2018), Kuala Lumpur, Malaysia, Dec. 12-15, 2018.

- Hyun Hwang, **Jun Han Bae**, and Byung-Cheol Min, "Design Guidelines for Sensor Locations on 3D Printed Prosthetic Hands", *IEEE Robotic Computing (IRC) 2017,* Taichung, Taiwan, April 10-12, 2017.

- **Jun Han Bae**, Jeehwan Park, Sangjun Lee, and Byung-Cheol Min, "Tri-SedimentBot: An Underwater Sediment Sampling Robot", *Automation Science and Engineering (CASE), 2016 IEEE International Conference,* Fort Worth, TX, USA, Aug. 21-24, 2016.

Refereed Reports & Extended Abastract

- **Jun Han Bae**, Pou Hei Chan, Shyam Sundar Kannan, Richard M. Voyles, Mauricio Postigo-Malaga, and Byung-Cheol Min, "Unmanned Sediment Sampling System for Surface Water Sediment Collection", *2020 RDE (Realizing the Digital Enterprise) Student Showcase "Mini-Talk" event,* West Lafayette, IN, USA, Nov. 18, 2020. [**RDE Mini Talk Award Winner**]

- Yogang Singh, **Jun Han Bae**, Wonse Jo, Yuta Haoshi, Jose Garcia, Brittany Newell, Mauricio Postigo, Sara McMillan, Richard Voyles, Lisabeth Leonor Pardes Aguilar, Godofredo Pena, Edgar Gonzales Zenteno and Byung-Cheol Min, "Design and Development of Unmanned Robotic Water Quality Monitoring and Sediment Sampling Systems", *6th Annual Environmental Community Mixer, Purdue Discovery Park Center for the Environment (C4E),* Purdue University, West Lafayette, IN, USA, Oct. 17, 2019.

- Shaocheng Luo, Yogang Singh, Hanyao Yang, **Jun Han Bae**, J. Eric Dietz, Xiumin Diao, and Byung-Cheol Min, "Coverage Path Planning for Efficient Spill Cleaning in Maritime Environment ", *6th Annual Environmental Community Mixer, Pur-*

due Discovery Park Center for the Environment (C4E), Purdue University, West Lafayette, IN, USA, Oct. 17, 2019.

- **Jun Han Bae**, Yogang Singh, Mauricio Postigo-Malaga, Lizbeth Leonor Paredes Aguilar, Bumjoo Lee, Richard M. Voyles and Byung-Cheol Min, "Design and Development of an Unmanned Underwater Sediment Sampling System", *40th Annual IWRA Spring Symposium,* Syracuse, Indiana, Jun. 26-28, 2019.

- **Jun Han Bae**, Wonse Jo, Jee Hwan Park, Shyam Sundar Kannan, Yuta Hoashi, and Byung-Cheol Min, "Robot-based Environment Monitoring: Application to Sediment Monitoring", *2018 RDE (Realizing the Digital Enterprise) Graduate Research Poster session,* West Lafayette, IN, USA, Nov. 26, 2018. [**Best Poster Award**]

- **Jun Han Bae**, Wonse Jo, Jee Hwan Park, Shyam Sundar Kannan, Yuta Hoashi, and Byung-Cheol Min, "Robot-based Environment Monitoring: an Application to Water Sediment Monitoring", *2018 5th Annual Purdue Environmental Community Mixer,* West Lafayette, IN, USA, Oct. 12, 2018.

- **Jun Han Bae**, Ramviyas Parasuraman, Wonse Jo, Arabinda Samantaray, Jee Hwan Park, Hunjung Lim, and Byung-Cheol Min, "Development of Autonomous Robotic Systems for Algae Removal", *2017 4th Annual Purdue Environmental Community Mixer,* West Lafayette, IN, USA, Sep. 15, 2017.

- **Jun Han Bae**, Shaocheng Luo, Jee Hwan Park, and Byung-Cheol Min, "Development of Autonomous Robotic Teams for a Real-Time Water Monitoring", *2017 4th Annual Purdue Environmental Community Mixer,* West Lafayette, IN, USA, Sep. 15, 2017.

- **Jun Han Bae**, Shaocheng Luo, Jee Hwan Park, and Byung-Cheol Min, "Technology in Water Quality Monitoring System: Cyber-Physical Systems (CPS) & Robotics", *2017 Midwest Robotics Workshop (MWRW),* Chicago, IL, USA, May. 18-19, 2017.

- **Jun Han Bae**, Shaocheng Luo, Jee Hwan Park, and Byung-Cheol Min, "Cyber-Physical Systems (CPS) based Water Quality Monitoring System with Collaborative Robots", *2017 I/UCRC: Center for Robots and Sensors for the Human Well-being (ROSE-HUB) IAB Meeting,* Minneapolis, MN, USA, Apr. 27-28, 2017.

- Hyun Hwang, **Jun Han Bae**, and Byung-Cheol Min, "Finding Optimal Sensor Location on Prosthetics for People with Limb Losses", *Health and Disease: Science, Technology, Culture and Policy Research Poster Session,* West Lafayette, IN, USA, Mar. 23, 2017.

- **Jun Han Bae**, Shaocheng Luo, Jee Hwan Park, Dong Hun Lee, and Byung-Cheol Min, "Water Quality Monitoring System Based on Robotics and Cyber-Physical Systems", *2016 I/UCRC: Center for Robots and Sensors for the Human Well-being (ROSE-HUB) IAB Meeting,* Charlotte, NC, USA, Nov. 17-18, 2016.

- **Jun Han Bae**, Dong Hun Lee, and Byung-Cheol Min, "Design and Concept of the Sediment Sampling Robot and Dynamic Buoy", *2016 IEEE/RSJ International Conference on Intelligent Robots and Systems (IROS), Late-Breaking Reports,* Daejeon, Rep. of Korea, Oct. 9-14, 2016.

- **Jun Han Bae**, Eric T. Matson, and Byung-Cheol Min, "Towards a Long-Term Wa- ter Monitoring with Continuous and Real-Time Autonomous System", *IEEE SSRR 2015, Late-Breaking Reports,* West Lafayette, IN, USA, Oct. 18-20, 2015.